

Performance improvement of professional printing systems : from theory to practice

Citation for published version (APA):

Ezzeldin Mahdy Abdelmonem, M. (2012). *Performance improvement of professional printing systems : from theory to practice*. [Phd Thesis 1 (Research TU/e / Graduation TU/e), Electrical Engineering]. Technische Universiteit Eindhoven. <https://doi.org/10.6100/IR731260>

DOI:

[10.6100/IR731260](https://doi.org/10.6100/IR731260)

Document status and date:

Published: 01/01/2012

Document Version:

Publisher's PDF, also known as Version of Record (includes final page, issue and volume numbers)

Please check the document version of this publication:

- A submitted manuscript is the version of the article upon submission and before peer-review. There can be important differences between the submitted version and the official published version of record. People interested in the research are advised to contact the author for the final version of the publication, or visit the DOI to the publisher's website.
- The final author version and the galley proof are versions of the publication after peer review.
- The final published version features the final layout of the paper including the volume, issue and page numbers.

[Link to publication](#)

General rights

Copyright and moral rights for the publications made accessible in the public portal are retained by the authors and/or other copyright owners and it is a condition of accessing publications that users recognise and abide by the legal requirements associated with these rights.

- Users may download and print one copy of any publication from the public portal for the purpose of private study or research.
- You may not further distribute the material or use it for any profit-making activity or commercial gain
- You may freely distribute the URL identifying the publication in the public portal.

If the publication is distributed under the terms of Article 25fa of the Dutch Copyright Act, indicated by the "Taverne" license above, please follow below link for the End User Agreement:

www.tue.nl/taverne

Take down policy

If you believe that this document breaches copyright please contact us at:

openaccess@tue.nl

providing details and we will investigate your claim.

**Performance Improvement of Professional
Printing Systems:**
from theory to practice

PROEFSCHRIFT

ter verkrijging van de graad van doctor
aan de Technische Universiteit Eindhoven,
op gezag van de Rector Magnificus, prof.dr.ir. C.J. van Duijn,
voor een commissie aangewezen door het College voor Promoties
in het openbaar te verdedigen
op woensdag 25 april 2012 om 16.00 uur

door

Mohamed Ezzeldin Mahdy Abdelmonem

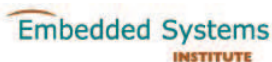
geboren te Menia, Egypte

Dit proefschrift is goedgekeurd door de promotoren:

prof.dr.ir. P.P.J. van den Bosch
en
prof.dr. S. Weiland



This work has been carried out as part of the OCTOPUS project with Océ Technologies B.V.



This project is under the responsibility of the Embedded Systems Institute.



This dissertation has been completed in fulfillment of the requirements of the Dutch Institute of Systems and Control DISC.

A catalogue record is available from the Eindhoven University of Technology Library.

Performance Improvement of Professional Printing Systems: *from theory to practice* / by
Mohamed Ezzeldin Mahdy Abdelmonem. – Eindhoven : Technische Universiteit Eindhoven,
2012

Proefschrift. ISBN: 978-90-386-3127-1

Copyright © 2012 by Mohamed Ezzeldin Mahdy.

This thesis was prepared with the L^AT_EX documentation system.
Cover Design: Verspaget & Bruinink, Eindhoven, The Netherlands.

Summary

Markets demand continuously for higher quality, higher speed, and more energy-efficient professional printers. In this thesis, control strategies have been developed to improve the performance of both professional inkjet and laser printers.

Drop-on-Demand (DoD) inkjet printing is considered as one of the most promising printing technologies. It offers several advantages including high speed, quiet operation, and compatibility with a variety of printing media. Nowadays, it has been used as low-cost and efficient manufacturing technology in a wide variety of markets. Although the performance requirements, which are imposed by the current applications, are tight, the future performance requirements are expected to be even more challenging. Several requirements are related to the jetted drop properties, namely, drop velocity, drop volume, drop velocity consistency, productivity, and reliability. Meeting the performance requirements is restricted by several operational issues that are associated with the design and operation of inkjet printheads. Major issues that are usually encountered are residual vibrations in and crosstalk among ink channels. This results in a poor printing quality for high-speed printing. Given any arbitrary bitmap, the main objective is to design actuation pulses such that variations in the velocity and volume of the jetted drops are minimized.

Several model-based feedforward control techniques using an existing model are implemented to generate appropriate input pulses for the printhead. Although the implementation of the model-based techniques shows a considerable improvement of the printhead performance compared with the current performance, further improvements are still necessary. We observe that besides the pulse shape the state of the ink surface at the nozzle plate (speed, position) at the start of the pulse influences the drop velocity considerably. This state at firing depends also on previous pixels in the bitmap of the image. Consequently, any pulse design has to guarantee almost the same initial state when firing a drop. Based on these facts, a model-free optimization scheme is developed to

minimize the drop velocity variations taking into account the bitmap information. Experimental results show the effectiveness of the optimized pulses.

Laser printing systems are highly depending on the appropriate combination of several design factors so as to become functional in a desired working range. The physical printing process involves multiple temperature set points at different places, precise electro-magnetic conditions, transfer of toner through certain pressures and layouts, and many other technical considerations. In the laser printing system there are several challenging issues and unknown disturbances. They originate from different sources, such as the printer itself (unknown phenomena appear, disturbances that are not foreseen, wear, contamination, failures, bugs), the environment of the system (power supply variations, temperature, humidity, vibrations), and the printing media (weight, coating, thermal properties, humidity characteristics, and initial temperature).

These issues have a negative effect on the stability and performance of the laser printing system. The objective is to design a control scheme to achieve printing quality requirements and a high productivity. Good printing quality means that the fusing temperature should track a certain reference signal at different operating conditions. Based on the printing system behavior, we propose two different control schemes to cope with the large parameter variations and disturbances, namely, a Model Reference Adaptive Controller (MRAC) and a nonlinear (scheduled) observer-based output feedback control scheme. Both control techniques yield considerable performance improvements compared with the present industrial controller.

Table of Contents

Summary	iii
Table of Contents	v
1 Introduction	1
1.1 Professional printing systems	2
1.2 Research targets	3
1.3 Methodology and main contributions	4
1.4 Thesis outline	6
2 Drop-on-Demand Professional Inkjet Printer	7
2.1 Inkjet printing technologies	8
2.2 DoD piezoelectric inkjet printer	12
2.3 Operational issues	17
2.4 Experimental setup	20
2.5 Objectives	20
2.6 Control limitations	22
2.7 Methodology	23
3 Model-Based Feedforward Control for a DoD Inkjet Printhead	25
3.1 Introduction	26
3.2 Inverse-based control	26
3.3 Control objectives	33
3.4 Printhead model	33
3.5 Single-channel feedforward control	35
3.6 Multi-channel control	41
3.7 Conclusions	47
4 Experimental-Based Control for a DoD Inkjet Printhead	49
4.1 Introduction	50
4.2 Input pulse parametrization	52

4.3	Experimental-based optimization	53
4.4	Multi-channel control	61
4.5	Bitmap-based control	66
4.6	Conclusions	70
5	Professional Laser Printers	75
5.1	Introduction	76
5.2	Development of laser printer	76
5.3	Description of the printing system	77
5.4	Printing system heat flow	80
5.5	Control challenges for the printing system	82
6	Improved Convergence of MRAC Designs for Laser Printer	85
6.1	Introduction	86
6.2	Preliminary	88
6.3	Nonlinear time varying adaptation gain	94
6.4	Multiple-adaptation gain MRAC design	96
6.5	Numerical comparison	104
6.6	Application of MRAC for laser printing system	109
6.7	Conclusions	110
7	Robust \mathcal{L}_2 Control for a Professional Printing System	113
7.1	Introduction	114
7.2	Problem formulation	115
7.3	Robust state feedback control	117
7.4	Robust output feedback control	121
7.5	LMI formulation for control synthesis	126
7.6	Simulation example	128
7.7	Robust control of professional laser printing system	137
7.8	Conclusions	142
8	Conclusions and Recommendations	143
8.1	Conclusions	143
8.2	Recommendations	147
	Bibliography	151
	Acknowledgments	159
	Curriculum Vitae	161

Chapter 1

Introduction

This work has been performed as a part of the Octopus project. This project was a cooperation between Océ Technologies, the Embedded Systems Institute, Eindhoven University of Technology, and seven academic partners. The main goal of this project is to define new techniques, tools, and algorithms to design professional printers, which adapt themselves to cope with changes that occur during operation. Printers and paper reproduction systems need to make on-line trade-offs between several system aspects so as to guarantee the performance of the system. By doing so, different demands of the customers can be optimally met in real-time using the same machine.

1.1 Professional printing systems

The market of professional printing systems is a segment where Océ plays a dominant role with systems that produce, distribute, and manage documents. Documents are printed in color or black and white and in a variety of formats, see Figure 1.1. The Océ customers are typically working in offices, education, industry, or the graphics industry. As such, the market of Océ starts at the top of the low cost office printers and ranges up to the offset lithography printers.

Faster, better quality, and lower costs of ownership are the main challenges for the development of professional printing systems. Recent advances in printing technology over the past few decades have made printing systems commercially available for home and office environments, with industry constantly pushing the limits in terms of productivity, accuracy, resolution, minimizing disturbance levels, reliability, and finding new applications. These printers depend on a wide range of deposition methods such as thermal and piezoelectric inkjet, and laser printing.



Figure 1.1: Various professional printers developed at Océ.

Several applications in industry are using inkjet printing technology due to its ability

to jet ink drops with variable size. In addition, it has shown potential for applications outside the document printing market due to its non-contact method of depositing ink or material droplets.

The fundamental requirement in all industrial printing applications is disposing and precise positioning of very small volumes of ink, typically 1-100 picoliters, on a printing medium. As inkjet applications grow, various types of jetting materials are required to be precisely dispensed from the inkjet printhead. Moreover, jetting performance needs to be efficiently controlled to make inkjet technology viable in various applications. However, during the jetting process several operational issues are encountered in the printhead, namely, residual vibrations and crosstalk. These operational issues result in large variations in the jetted drop properties, drop velocity and drop volume. Obviously, these variations limit the printhead performance. To improve the printhead performance with respect to drop velocity and drop volume, the actuation input for the printhead has to be properly designed. The designed actuation pulse should be able to achieve desired drop properties independent of the operational issues, jetting frequency, and bitmap to be jetted. Successful design for the actuation input requires understanding of the basic physics of drop formation and how the actuation input influences this jetting performance. The interactions between individual drops and the printing media as well as between adjacent drops are important in defining the resolution and accuracy of printed objects.

Similarly, the key challenges of professional laser printers are to produce printed documents with the appropriate printing properties at acceptable price with high productivity and accuracy. The professional printing market has a high demand on print consistency and print quality. There are many external and internal parameters that influence consistency and quality (e.g. humidity, temperature, speed) and they have to be controlled. To introduce new and exciting applications, the printing system should be able to handle a wide range of media with an appropriate performance. An increasing range of paper sizes, weights, color, texture and finishing is required. Complex printing jobs might include multiple media types in one pass requiring a wide media range which can run concurrently in a print job. To meet these challenges, the printing system should be able to print with variable speed and on a wide variety of printing media.

1.2 Research targets

The thesis is divided into two main parts: a drop-on-demand inkjet printing system and laser color printing.

- The first case tackles the operational issues, residual vibrations and crosstalk, encountered in a drop-on-demand inkjet printing system.

These operational issues limit now the attainable performance of the printhead. Large variations in the drop properties result as a consequence of varying the jetting frequency and the bitmap. That results in the following research goal,

1. *Design simple actuation pulses for an arbitrary bitmap and a range of jetting frequencies such that the resulting drop properties are similar under all conditions.*
- The second part of this thesis focuses on laser color printing.

Laser printers have to produce high quality prints, have a high throughput, have to be reliable under a large range of conditions, and yield a low per-print cost. As a result, such printers should be adaptable with respect to variations in media, and the environmental variations. These challenges pose the following research goals,

1. *Achieve accurate temperature control within a constrained real-time environment with fast and large parameter variations.*
2. *Design a control system that incorporates the available information about the print job to maximize throughput while satisfying in all situations quality constraints.*

1.3 Methodology and main contributions

1.3.1 Inkjet printing system

The operational issues are large, but they are also reproducible and predictable. There are rather accurate models, but no sensors available for real-time measurements. Therefore, feedforward control is suitable for designing the actuation pulse. In this thesis, two different feedforward approaches are investigated.

Firstly, an inverse-based feedforward control is implemented to deal with the residual vibrations and crosstalk. Inverse-based control is successfully used for high-precision application since it has the ability to perfectly track a desired trajectory with high precision. That makes this control strategy very appealing in our application. We explore different possibilities of the inverse control to cope with the residual vibrations and crosstalk.

To overcome the modeling problems that usually degrade the performance of the model-based feedforward control, an experimental-based feedforward control is proposed. In this approach, the actuation pulse is optimized based on the measured drop properties. The optimization is carried out with a printhead in the loop. Therefore, all modeling issues are avoided. The main advantage of this approach is that the feedforward input

is designed based on the drop properties, which are the main measure for the printing quality, and not on an intermediate variable. By understanding the physics of a print-head, a simple structure of the actuation pulse is suggested. This structure allows a simple optimization and opens a possibility for real-time pulse adaptation if measurements become available. We show throughout the thesis that designing the proper pulse will considerably improve the printhead performance without redesigning the existing printhead.

1.3.2 Laser printing system

Based on the research goals and the analysis of existing control strategies show that gain scheduling, adaptive control and/or robust control are appropriate strategies. As we know the changing parameters, robust control will be too conservative yielding less performance. For adaptive control the emphasis has to be focused on fast adaptation rate.

Adaptive control is a very powerful tool when the system dynamics are time varying. The main difference between adaptive control and robust control is that adaptive control does not need any priori knowledge about the bounds on these uncertain or time-varying parameters. Robust control guarantees that if the changes are within given bounds the control law need not be changed, while stability is guaranteed. Adaptive control is concerned with control laws, which adapt themselves. The large and fast variations in the printing system require adaptive controllers with a short adaptation phase. Therefore, we propose two methods to improve the adaptation convergence of the adaptive control.

Since the main source of parameter variations is due to different printing jobs, which is known, gain scheduling is an appropriate choice to incorporate this knowledge. Once an operating point is detected, the controller parameters are changed to the appropriate values, which are obtained from the precomputed parameters set. Transitions between different operating points, which lead to significant parameter changes, are handled by interpolation or by increasing the number of operating points. Thus, the gain scheduler consists of a look-up table and the appropriate logic for detecting the operating point and choosing the corresponding values of the controller parameters from the table. Adaptive control and gain scheduling are both used to adapt the printing system to physical runtime variations and to optimize the system to the different and changing preferences of the user.

1.4 Thesis outline

Part I : Professional Inkjet Printing System

In chapter 2, we start with a historical overview about the development of inkjet printing systems. We explain the basic principles and the structure of the printhead under investigation. That leads to a discussion over the operational issues that degrade the performance of the printhead. We present an experimental setup, which is used to study the printhead. Finally, we indicate the main industrial and research challenges and a short overview about the methods to achieve these objectives.

In chapter 3, we present the application of the inverse-based feedforward control to cope with the residual vibrations and crosstalk in the inkjet printer. We start with exploring the basics of the model-based inverse control and with formulating the control objectives. Finally, the application of the feedforward control to single and multi channel(s) with simulation and experimental results are described.

In chapter 4, an experimental-based control strategy is developed to reduce the effect of the residual vibrations and crosstalk. A new parametrization of the actuation pulse is introduced. Based on physical understanding the dynamics of an ink channel, we define a solution: each pulse has to start with the same state (meniscus velocity and meniscus position). We formulate optimization problems to reduce the drop velocity variations for both single and multi channel(s). Finally experimental results show the effectiveness of the optimized pulses.

Part II: Professional Laser Printing System

In chapter 5, we present an overview of the laser printing system. A brief description of the printing process is given. We identify a set of challenging control problems that are relevant to the printing process. Consequently, we motivate the use of adaptive control to tackle these control problems.

In chapter 6, model reference adaptive controller (MRAC) is selected to improve the behavior of the laser printing system. Two different methods to improve the convergence of the MRAC, namely, using a nonlinear varying adaptation gain and using multiple adaptation gains with a new adaptation law are addressed. Using a numerical example, the performance of the two methods are compared with the performance of the standard MRAC. Finally, the application of the proposed approaches for a printing system is illustrated.

In chapter 7, a Takagi-Sugeno (T-S) model is proposed as a feasible approximation to the laser printing system. A robust control problem is formulated taking into account the approximation error. Based on the print job, state and output feedback controllers are designed. The application of this robust gain-scheduling control design to a professional printing system is discussed.

In chapter 8, the conclusions and the recommendation of this research are presented.

Chapter 2

Drop-on-Demand Professional Inkjet Printer

Drop-on-demand (DoD) inkjet printing is an efficient technology for depositing picoliter drops on various printing surfaces. DoD technology is compatible with various liquids and does not require contacting the printing media. DoD inkjet printing combines several advantages including high speed, quiet operation, and compatibility with a variety of printing surfaces. Moreover, with DoD printing one can make patterns without any additional lithographic processes. Inkjet printing can reduce the number of processing steps compared to conventional patterning processes. This results in a lower production cost in manufacturing. Besides the well known small inkjet printers used as home or office appliances, professional inkjet printers are widely used in industry. Nowadays, DoD inkjet technology is applied in many engineering and scientific applications, see Figure 2.1. Inkjet technology is not only used for document printing, the production of posters, and CAD drawings but it is also applied in the electronics industry for the production of polyLED displays and the production of biochips for medical research. In textile industry, wide-format inkjet printers are used to print on silk, cotton, and polyester. Inkjet technology plays also an important role in 3D printing of rapid prototyping [1]-[5].

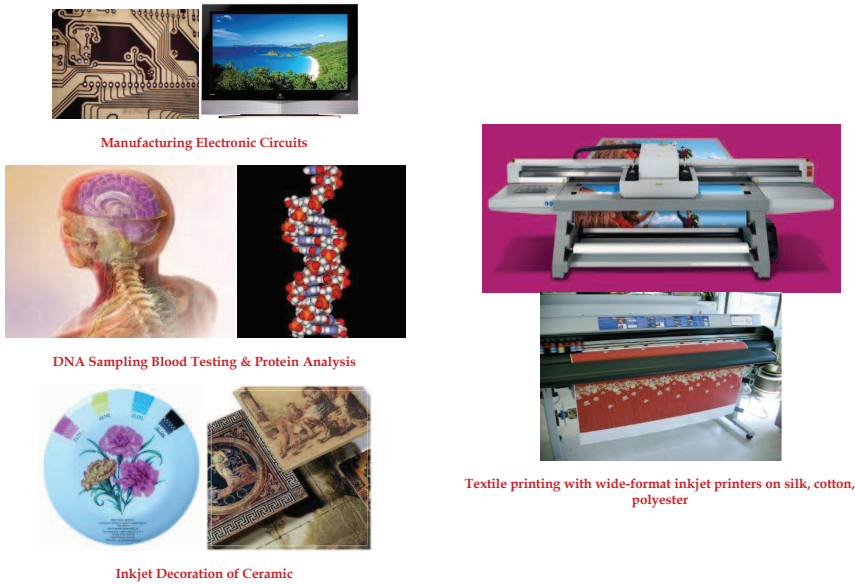


Figure 2.1: Various applications of Inkjet printing.

2.1 Inkjet printing technologies

In inkjet technology, one distinguishes between continuous inkjet or drop-on-demand (DoD). For continuous inkjet printer, a continuous stream of ink is supplied to the print-head. DoD is a broad classification of inkjet printing technologies where drops are ejected from the printhead only when required. The drops are usually formed by the creation of pressure pulses within the printhead. The particular method that is used to generate these pressure pulses creates the primary subcategories within DoD technology, namely, thermal, piezoelectric, electrostatic, and acoustic. In this section, we provide a short overview of the development of the inkjet technology. After that, we explain the basic mechanisms of different inkjet technologies.

2.1.1 History of inkjet technologies

In 1878, Lord Rayleigh described the basic principles of how a liquid stream breaks up into drops [6]. However, it took several decades before implementing these physical principles into a working device. The first device based on these principles was developed in 1948 by Siemens Elema in Sweden [7]. This device was similar to a galvanometer. Instead of using a pointer as an indicator, a pressurized continuous stream of ink was used to record the signal onto a transported recording media.

In the early 1960s, the principle of continuous inkjet printing was established. By applying a pressure wave pattern, the ink stream is splitted into drops of uniform size and spacing [8]. After breakoff, an electric charge is imposed on the drops. While passing through an electric field, the uncharged drops are deflected into a collector for recirculation, whereas the remaining charged drops are disposed directly onto the media to form an image. In the 1970s, IBM launched a development program for continuous inkjet technology [9].

In the late 1970s, the first DoD inkjet technology appeared. A DoD printer ejects ink drops only when these drops are used in imaging on the media. Many DoD inkjet systems were invented, developed, and produced commercially in the 1970s and 1980s, including the Siemens PT-80 serial character printer [10]. In these printers, a voltage pulse causes ink drops to be ejected as a result of a pressure wave created by mechanical motions of piezoelectric ceramic actuators.

In 1979, Canon invented a mechanism, called the *bubble jet*, where ink drops are ejected from the nozzle by the expansion of a vapor bubble on the top surface of a heater located near the nozzle [11]. At the same time, Hewlett-Packard developed a similar inkjet technology called *ThinkJet* (thermal inkjet) [12]. This development was the first low-cost inkjet printer based on the bubble jet principle.

Since the late 1980s, thermal inkjet or bubble jet printers became the practicable alternative to impact dot-matrix printers for home and office use, mainly because of their color capabilities, small size, low cost, and quietness. For more details about the history of inkjet technology development, see [13]-[16].

2.1.2 Inkjet technology map

Inkjet printing has been implemented in many different designs and has a wide range of potential applications. A basic overview of inkjet technologies is shown in Figure 2.2. Inkjet printing technologies are divided into the continuous and the DoD inkjet methods.

The basic mechanism of the continuous printing technology is to pump fluid from a reservoir to small nozzles, which eject a continuous stream of drops at high frequency, typically from 50 kHz to 175 kHz, using a vibrating piezoelectric crystal. The drops are electronically charged by passing them through a set of electrodes. The charged drops then pass a deflection plate that uses an electrostatic field to deflect the drops that will be printed. Undeflected drops are collected and returned for re-use.

As depicted in Figure 2.3, in this deflection methodology, the continuous inkjet is de-

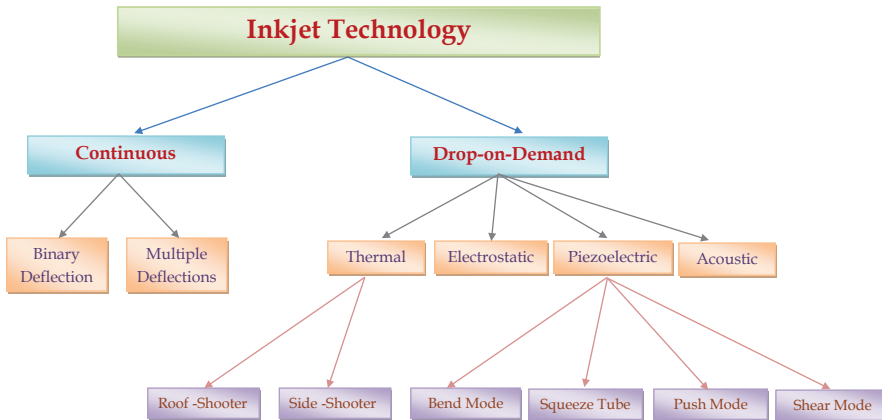


Figure 2.2: Inkjet technology diagram.

signed as a binary or multiple deflection system that separates drops for print from drops that are recollected and not printed. In a binary deflection system, the drops are either charged or uncharged. The charged drops are disposed directly onto the media, while the uncharged drops fly into a gutter for recirculation. In a multiple deflection system, drops are charged and deflected to the media at several levels. The uncharged drops pass straight to a gutter from where the ink is recirculated.

Also the DoD inkjet printers eject ink drops as a result of an electric signal, but only when needed. Depending on the actuator, the DoD printing technology is classified into thermal and piezoelectric. In the thermal process, drops of ink are forced out of the nozzle by heating a resistor to 350 – 400 C, which causes a thin film of ink above the heater to vaporise into a rapidly expanding bubble. Depending on its configuration, a thermal inkjet is either a roof-shooter with an orifice located on top of the heater, or a side-shooter with an orifice located on a side nearby the heater, see Figure 2.4.

The advantages of thermal inkjet include the high nozzle density and potential for very small drop sizes. High nozzle density leads to compact devices, potentially, high-resolutions, and low printhead costs. On the other hand, the drawbacks of this technology are mainly related to the limitations of the fluids that can be used. The fluid has to contain a substance that can be vaporized at reasonable temperatures and has to withstand the effects of high temperatures. Moreover, these high temperatures can form a hard coating on the resistive element, which degrades its efficiency and, ultimately, the life of the printhead.

Nowadays, professional and industrial inkjet printers use a piezoelectric actuator in an

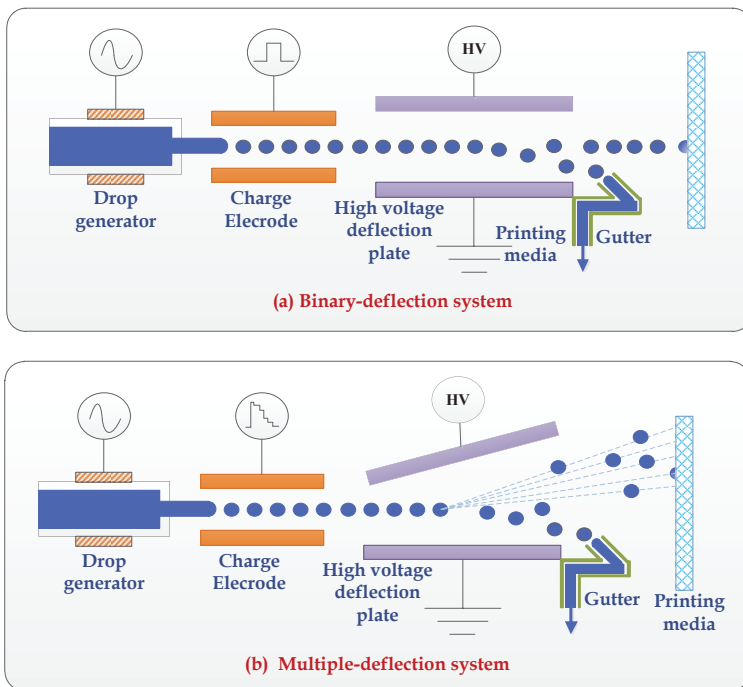


Figure 2.3: Continuous inkjet printer configurations.

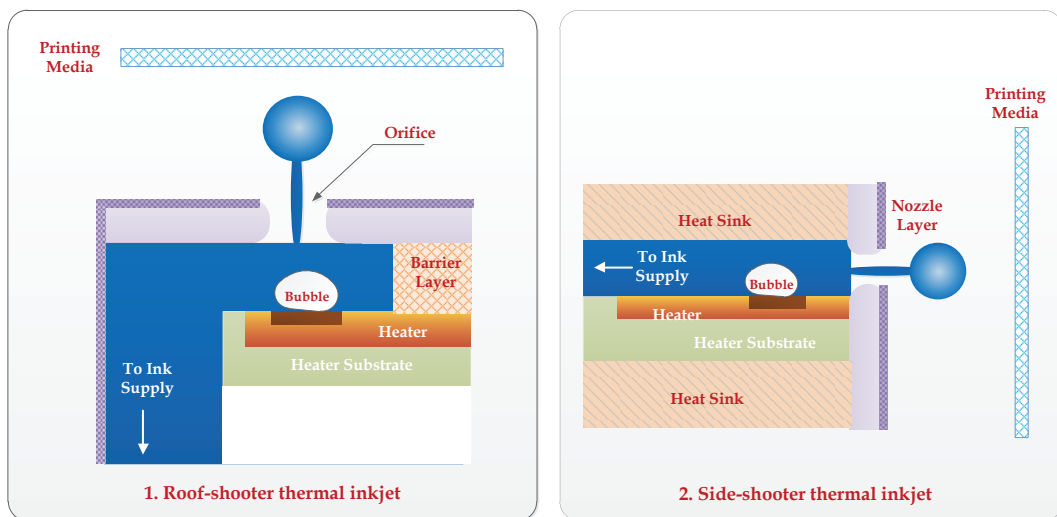


Figure 2.4: DoD thermal inkjet printer configurations.

ink-filled chamber behind each nozzle instead of a heating element. By applying a voltage, the piezoelectric material changes its shape or size, which generates a pressure pulse in the fluid forcing a drop of ink to leave the nozzle.

Based on the piezoelectric actuator deformation mode, the piezoelectric technology is classified into four main types, namely, squeeze mode, bend mode, push mode, and shear mode, see Figure 2.5. For squeeze mode, radially polarized ceramic tubes are used. In both bend and push mode design, the electric field is generated between the electrodes parallel to the polarization of the piezoelectric material. In a shear mode printhead, the electric field is designed to be perpendicular to the polarization of the piezoelectric actuator.

A piezoelectric inkjet printer allows a wide variety of fluids in a highly controllable manner and high reliability with a long life for the printhead. However, the printheads are expensive, which limits the applicability of this technology in low-cost applications.

2.2 DoD piezoelectric inkjet printer

In this thesis, we focus on a DoD piezoelectric inkjet printhead, which consists of ink channels with a high integration density. Each channel is equipped with its own piezoelectric actuator. The ink in the channel is supplied from a reservoir, which is located above the channels. Filters ensure that no unwanted particles enter the ink channels. An actuator foil covers the ink channels in the channel block. The foil is connected to the actuator plate with piezoelectric elements and substrate. The nozzle plate, which contains the nozzles, is mounted to the bottom of the head. The part of the head between a channel and a nozzle is called the *connection*. In Figure 2.6, an exploded view of the piezoelectric inkjet printhead is shown together with a schematic representation of a single channel.

2.2.1 Printhead dynamics

The fluid dynamics in the ink channel is governed by the wave propagation equation [15]-[16]. Consider the one-dimensional linear wave equation

$$\frac{\partial^2 P}{\partial x^2} - \frac{1}{\nu^2} \frac{\partial^2 P}{\partial t^2} = 0, \quad (2.1)$$

and

$$\frac{\partial^2 \zeta}{\partial x^2} - \frac{1}{\nu^2} \frac{\partial^2 \zeta}{\partial t^2} = 0, \quad (2.2)$$

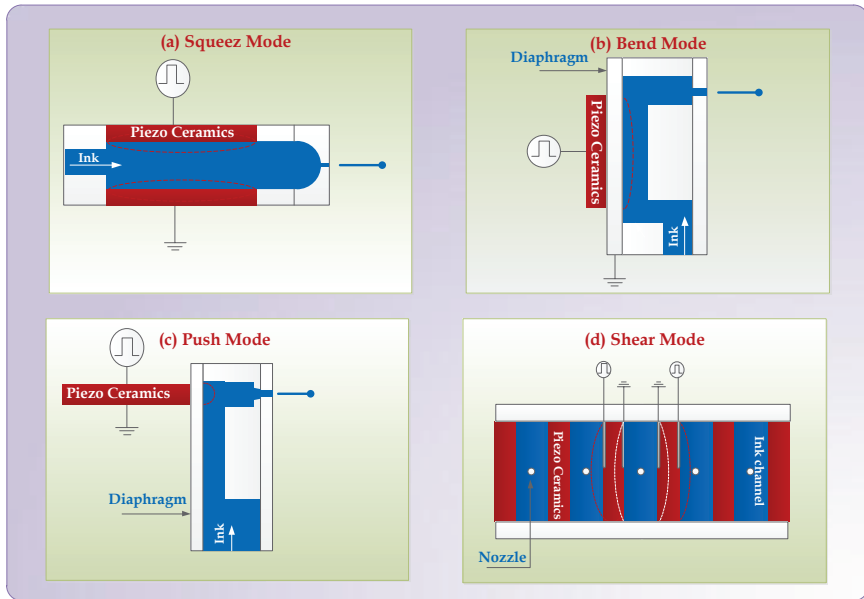


Figure 2.5: DoD Piezoelectric inkjet printer modes.

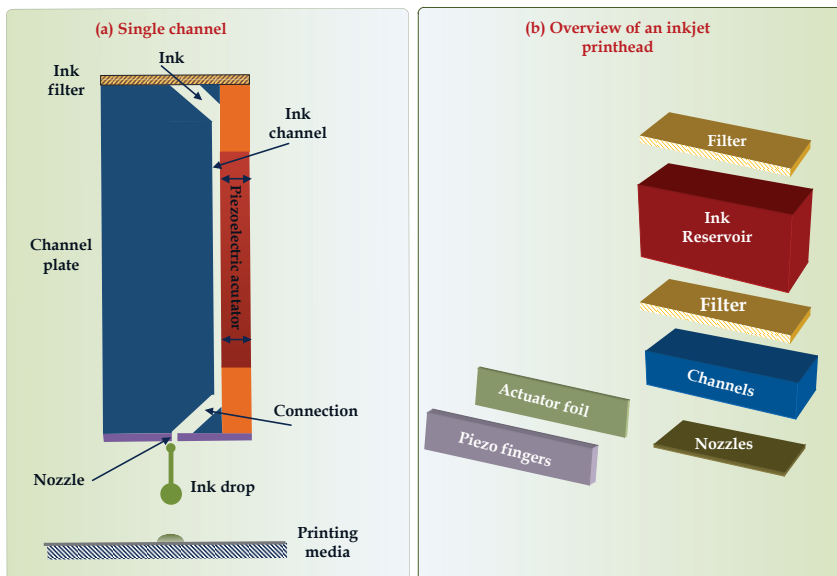


Figure 2.6: Schematic representation of a single channel (a) and overview of a piezo-electric inkjet printhead (b).

with

$$x \in [0, L], \quad t \geq 0,$$

that describes the pressure $P(x, t)$ and the particle displacement $\zeta(x, t)$ in a medium of a one-dimensional channel, where ν is the sound speed in the medium and L is the length of the channel. The relation between the pressure P and the displacement ζ is given by

$$P = -\rho\nu^2 \frac{\partial \zeta}{\partial x}, \quad (2.3)$$

with ρ the fluid density. Suppose that the sound speed ν is a constant, then each solution of (2.1) can be written as

$$P(x, t) = f(x - \nu t) + g(x + \nu t), \quad (2.4)$$

where f and g are two twice-differentiable functions. The pressure inside the channel is therefore the sum of two pressure profiles. The pressure wave f travels in the positive direction of the x -axis with velocity ν , while the pressure wave g travels in the negative direction of the x -axis with velocity ν .

When an obstruction occurs at some location inside a channel, part of the pressure wave is transmitted and part is reflected. A reflection coefficient describes either the amplitude or the intensity of a reflected wave relative to an incident wave. The reflection coefficient is closely related to the transmission coefficient. The simplest cases to analyze are the idealized open and closed ends. These assumptions are also appropriate for the end conditions in the DoD inkjet channel, where the side on which the nozzle plate is attached can be modeled as closed, since the nozzle opening is a negligible fraction of the channel cross-sectional area. The reservoir side can be considered as open, since the inside diameter of the reservoir is considerably larger than the inside diameter of the channel. The pressure reflections from open and closed ends are obtained from the boundary conditions with the use of (2.1) and (2.3).

Consider first the open end, where the (left) boundary condition of (2.1) is assumed to be zero pressure $P(0, t) = 0$. This boundary condition is satisfied by superimposing a similar pressure wave of opposite sign on the incident pressure wave. This pressure wave is traveling in the opposite direction at the same distance from the end as the incident wave. On the other hand, for the closed end the boundary condition is zero velocity $\frac{\partial \zeta}{\partial t}(L, t) = 0$. Since the displacement $\zeta(x, t)$ satisfies the same wave equation as the pressure (2.1), it follows that the velocity also satisfies a similar equation. Hence, displacement and velocity have propagating wave solutions similar to (2.4). Therefore, when the wave reflects from an open end, the phase of the reflected wave is the same

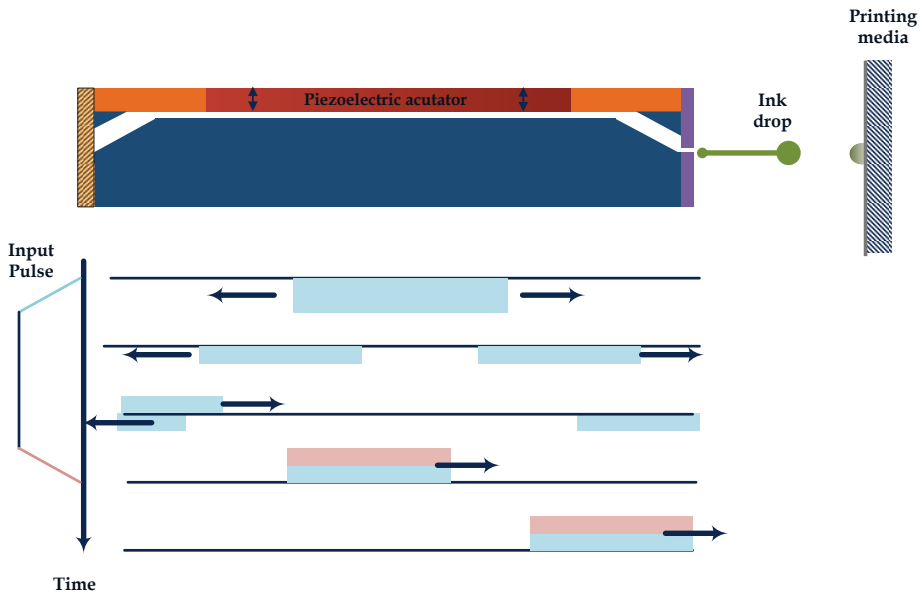


Figure 2.7: Drop jetting mechanism.

phase of the incident wave. A wave pulse reflects from an open end with the opposite phase as the incident wave.

According to the above analysis, a trapezoidal pulse is applied to the piezoelectric actuator to fire a drop, as shown in Figure 2.7. Then, ideally, the following occurs. First, a pressure distribution is generated in the channel by enlarging the volume in the channel. The initial pressure profile splits and propagates in both directions. These pressure waves are reflected at the reservoir that acts as an open end and at the nozzle that acts as a closed end. A negative pressure profile reflects at the nozzle and causes the meniscus to retract. The meniscus is the curve in the upper surface of the ink close to the surface of the nozzle. Next, by decreasing the channel's volume to its original value, a positive pressure profile is superimposed on the reflected waves when these waves are located exactly in the middle of the channel. Consequently, the wave traveling toward the reservoir is canceled, whereas the wave traveling toward the nozzle is amplified such that the pressure is large enough to result in a drop.

2.2.2 Drop formation

For simulating the drop formation the nonlinear Navier-Stokes equations have to be solved numerically. Usually, these models are 3D or 2D and computationally intensive. For a typical printhead, the drop formation process includes four main stages, as shown

in Figure 2.8 where red color reflects low pressure inside the channel, while blue color represents high pressure in the channel.

First, the negative pressure inside the ink channel causes a retraction of the meniscus. This negative pressure is caused by the initial pressure wave that hits the channel nozzle interface, as explained in the previous section, see Figure 2.8A.

As a result of the positive pressure wave that hits the channel nozzle, the meniscus velocity starts to increase and starts moving outside the nozzle without deformation. Then, the meniscus surface starts deforming in outward direction against the surface tension. The deformed area grows in both radial and axial direction. After that, the velocity of the ink reaches its maximum, see Figure 2.8B-C.

As shown in Figure 2.8D, the pressure becomes negative again and the velocity of the meniscus starts to decrease. This causes a decreasing flow of mass and kinetic energy in outward direction. Due to the surface tension, necking of the drop's tail takes place at the tip of the nozzle.

Finally, the velocity of the ink becomes negative, the tail breaks, and the drop is jetted. During this process the tail might break up, forming satellite drops. These satellites may or may not catch up with the main drop and merge, see Figure 2.8E. Satellite drops highly affect the printing quality. Therefore, the combination of ink properties, viscosity and surface tension, nozzle design and actuation pulse is tuned to create consistent drops without depositing satellites on the printing media.

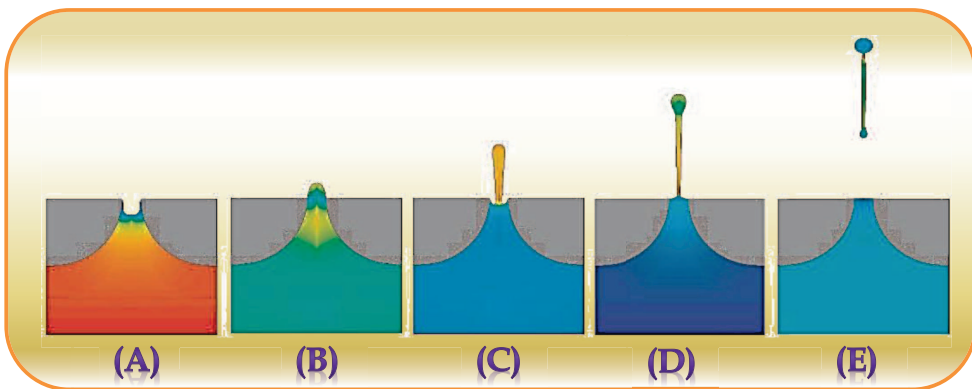


Figure 2.8: The drop formation process simulated by Flow3D.

2.2.3 Printhead performance

Although the performance requirements, which are imposed by the current applications, are tight, future performance requirements are expected to be even more challenging. Several requirements are related to the resulting drop properties, namely, drop velocity, drop volume, drop velocity consistency, productivity, and reliability.

The resulting drops are required to have a certain velocity, typically around 5 – 10 m/s. A high drop velocity results in a short time of flight. Therefore, the disturbance effects, such as variations in the printhead-printing media distance, are reduced, thus the dot position errors are smaller. Depending on the application, the performance requirement concerning volume typically varies from 1 to 25 picoliters. Some applications require that the drop size is varied during the operation. For instance, when large areas are needed to be covered, large drops are desired, whereas for high-resolution printing small drops are desirable.

Consistency of drop velocity is a crucial issue for the printing quality. The variations in the drop velocity between successive drops and between the nozzles must stay within 1 m/s, to avoid irregularities and shadow effects in the printed object. The productivity of a printhead is mainly determined by the number of nozzles per inch and the jetting frequency. Jetting frequency is defined as the number of drops that a channel jets within a certain time, which is typically 50 – 60 kHz. Evidently, these two factors depend on the design of the printhead and the actuation signal.

Reliability of the jetting process is one of the prominent performance requirements for printheads. Reliability is defined as the absence of nozzle failures per a certain number of jetted drops, a typical value for nozzle failure is once per million drops.

2.3 Operational issues

Meeting the above performance requirements is severely disrupted by several operational issues that are associated with the design and operation of inkjet printheads. Major issues that are usually encountered are residual vibrations and crosstalk. We discuss these items next.

2.3.1 Residual vibrations

After a drop is jetted, the fluid mechanics within an ink channel are not at rest immediately. Traveling pressure waves remain present. Figure 2.9 shows the time trajectory of the meniscus velocity when a standard trapezoidal actuation pulse is applied to the piezoelectric actuator. Usually, the fixed actuation pulse is designed under the assump-

tion that a channel is at rest. This assumption is apparently not satisfied for about 100 μs , see Figure 2.9, after the actuation pulse. The time needed for the residual vibrations to damp out is substantially larger than the short actuation time. This transient time in the residual vibrations limits the maximally attainable jetting frequency to 10 kHz, and, therefore, the drop properties and even the stability of the jet process cannot be guaranteed at higher frequencies. These oscillations have significant consequences concerning the productivity and drop consistency of a printhead.

The presence of residual vibrations highly affects the volume and the velocity of the subsequent drops being fired. Since the initial values of meniscus position and meniscus velocity play a crucial role in determining the velocity of the jetted drop, the residual vibrations result in a different initial meniscus position and velocity for the subsequent drops. To obtain acceptable drop characteristics with this fixed actuation pulse, the fixed actuation pulse is designed for a specific basic jetting frequency with a small range of frequencies around this basic frequency. To be more flexible and robust, the printhead must jet drops over a wider frequency range with the same or even improved drop properties.

For a continuous jetting nozzle, the DoD frequency curve for the velocity, as shown in Figure 2.10, is obtained. The DoD curve describes the relation between the jetting frequency and the drop velocity. This curve demonstrates that, depending on the jetting frequency, positive or negative interference of the pressure waves results in a higher or lower drop velocity. As depicted in the figure, considerable velocity fluctuations result from the presence of the residual vibrations. The drop velocity varies from 2.5 to 13.5 m/s. Ideally, the drop velocity is required to be independent on the jetting frequency and to remain constant for all jetting frequencies, as shown in Figure 2.10.

2.3.2 Crosstalk

A second phenomenon that is encountered in jetting is the interaction between different channels, this phenomenon is known as crosstalk. The crosstalk originates from the fact that the pressure waves within one channel influence the neighboring channels. This type of crosstalk is known as *acoustic crosstalk*. Another source of the crosstalk is the deformation of the channel. Since all piezoelectric fingers are connected to a substrate, a deformation of one piezoelectric actuator induces a deformation of the neighboring units. Consequently, the volume of the neighboring channels changes too, which induces pressure waves in the neighboring channels. The deformation of the printhead structure can originate from two sources. The first source is the result of a channel being actuated and is referred to as *direct voltage crosstalk*. The second source is the result of the occurring pressure wave that causes deformation of the channel and is called indirect or pressure crosstalk.

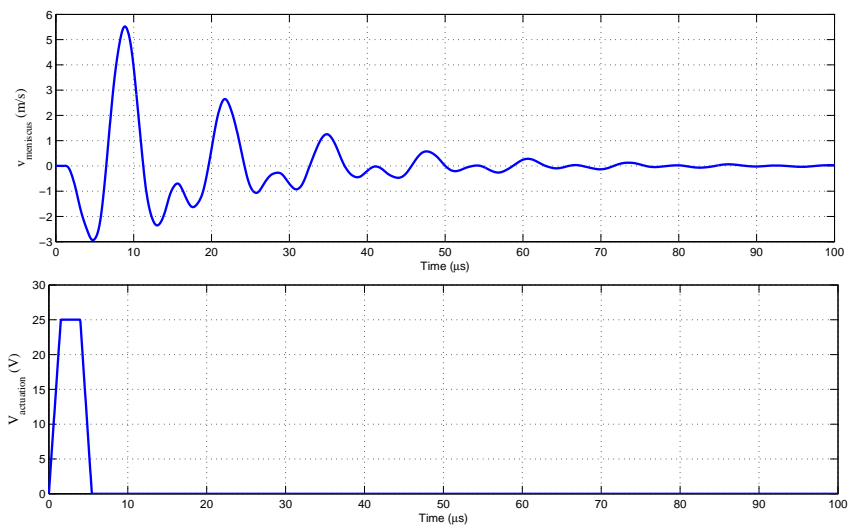


Figure 2.9: Simulated time response of the meniscus velocity on a fixed trapezium-shaped pulse.

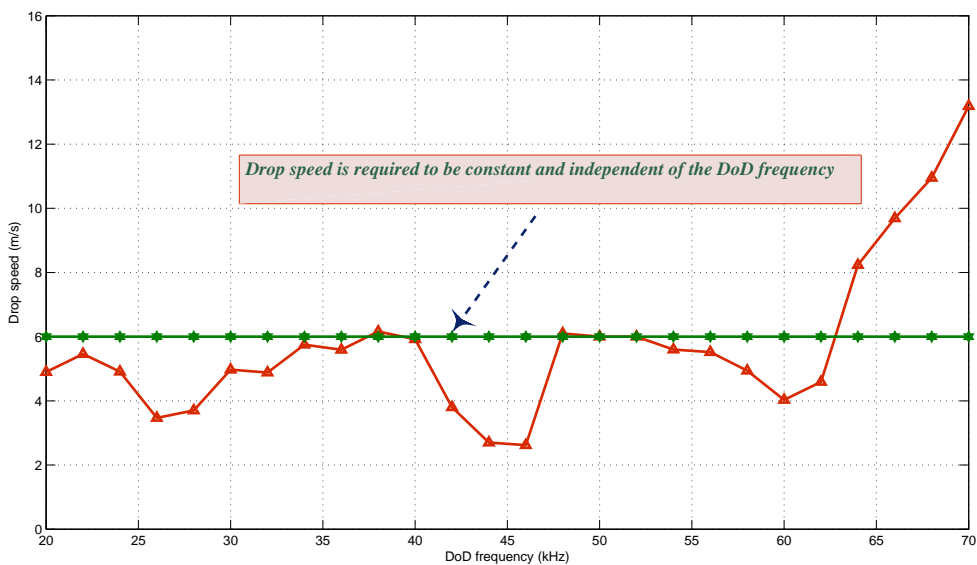


Figure 2.10: Drop-on-demand velocity curve of the standard pulse for different jetting frequencies.

The influence on the drop velocity of the center channel of an array of channels when neighboring channels are active is shown in Figure 2.11. When the direct neighbor, channel 1 or -1, in particular, becomes active, the drop velocity of channel zero drops from 6 to 5 m/s. As shown, the effect of crosstalk on the drop velocity is substantial. Note that for channels located further away, the influence of crosstalk decreases. Optimally, the drop velocity is required to be constant and independent on the actuation of the neighboring channels.

2.4 Experimental setup

A schematic overview of the experimental setup is depicted in Figure 2.12. With this setup, inkjet printheads can be investigated in various ways. The input is the voltage applied to a piezoelectric actuator of the inkjet printhead. Two sensors are available in this setup. The piezoelectric element can be used not only as an actuator but also as a sensor to measure the pressure waves in the channel after jetting a drop, this signal is known as PAIN signal. A charge-coupled device camera, equipped with a microscope, is used to monitor the properties of the resulting drop.

The ink drops are monitored by means of optical methods like stroboscopic illumination at drop formation rate and high-speed camera. The setup can be divided into a part, which controls the printhead and a part to visualize the drops. The required reference temperature is controlled by a PID controller. The printhead is mounted in the vertical direction with the nozzles faced down. An air pressure unit keeps the pressure in the ink reservoir 8 mbar below the ambient pressure to avoid that the ink flows out of the nozzles under the influence of gravity.

As depicted in Figure 2.12, the setup is connected to a computer that is equipped with cards for image processing and communication. On this computer, the desired actuation signals can be programmed and relevant data can be stored and processed. After defining the actuation signal parameters, these parameters are sent to a waveform generator. The waveform generator sends the signal to an amplifier unit. From the amplifier unit, the signal is fed to a switchboard. The switchboard is controlled by a computer and determines which channels are provided with the appropriate actuation signals. An oscilloscope is used for tracing both the actuation and PAIN signals. This oscilloscope is connected to the computer and displayed data can be stored on the computer.

2.5 Objectives

Residual vibrations and crosstalk result in large variations in the drop velocity and volume. In the current inkjet printers, a fixed actuation pulse is used. This pulse cannot

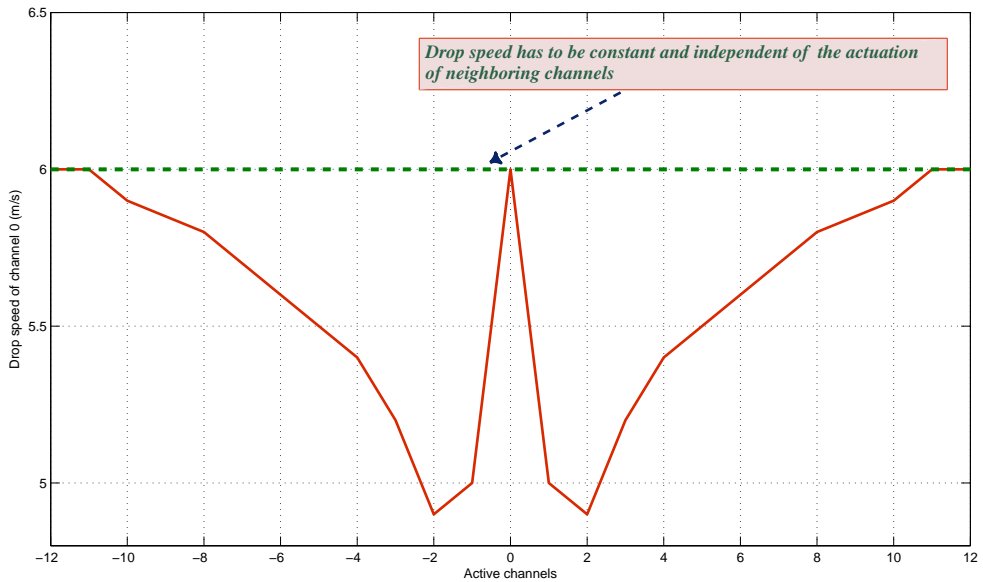


Figure 2.11: Influence on the drop velocity of channel 0 (center channel) by actuation of different neighboring channels at the same time.

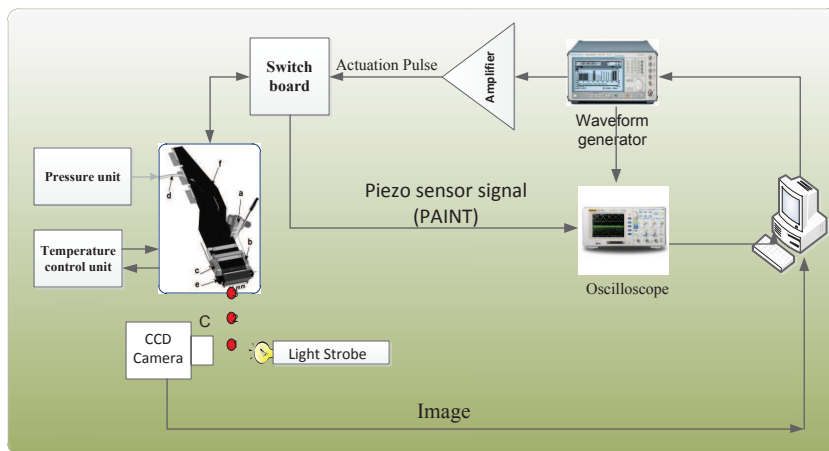


Figure 2.12: Schematic diagram of the experimental setup.

cope with the mentioned operational issues that highly affect the print quality. Apparently, the state (both meniscus position and velocity) at the firing instant determines the drop velocity and drop volume. The state at firing depends also on the bitmap (pixels on/off). Differences in drop velocity cause drops to arrive at the printing media at unpredictable positions. Differences in volume lead to color density variations on the printing media. These variations result in ragged edges or banding, and therefore reduce print quality.

The main objective in this study is to improve the performance of the printhead. In particular, we focus on drop velocity consistency and productivity. Thus, we want to minimize the velocity variations that occur due to the presence of the residual vibrations and crosstalk.

This problem statement can be translated to the following objectives:

1. To reduce the drop-velocity variations for each nozzle at each jetting frequency (≤ 1 m/s)
2. To reduce the drop-velocity variations over all the jetting frequencies (flat DoD curve), it has to be less than 1 m/s over the frequency range 20-70 kHz.
3. To reduce the effect of the crosstalk. For any arbitrary bitmap, the maximum drop-velocity variation of the jetted drops has to be less than 1 m/s.

Thus, given an arbitrary bitmap, our main objective is to design actuation pulses such that the same initial meniscus state at firing a drop is guaranteed.

2.6 Control limitations

To achieve these objectives, the actuation pulse should be designed to damp the residual vibrations and minimize the crosstalk. There are several control techniques to design the actuation input. However, there are two basic restrictions that don't allow full control of the printhead.

1. No sensors are available for online measurements of any variable. Consequently, this excludes any possibility for feedback control. Since the printheads behave in a predictable way based on their physical designs, feedforward control can still be a suitable option.
2. Only certain classes of actuation inputs can be used, since only trapezoidal-shaped pulses can be generated using the current driving circuits. This limits the control scope to a pulse shaping problem.

2.7 Methodology

In chapter 3, a model-based control approach to design the jetting pulses is described. In this approach, an inversion-based feedforward controller is proposed, where the controller dynamics are chosen to be the inverse of the printhead dynamics. This cancels all system dynamics and yields an overall unity transfer function. This is the Perfect Tracking Controller (PTC) strategy. Hence, the actual drop velocity will be exactly the same as the desired input velocity. A common difficulty in realizing a PTC strategy, however, is that the PTC may produce unbounded or oscillatory outputs. This will occur when the transfer function of the system contains zeros that cannot be canceled. Two classes of zeros are regarded in this respect, unstable zeros (non-minimum phase or unstable inverse) and stable oscillatory zeros (oscillatory inverse). The former implies an unstable controller, while the latter might generate oscillatory control efforts reaching the actuator saturation levels. Since the dynamics of the printhead shows a non-minimum phase behavior, various feedforward control algorithms are presented in chapter 3. An optimal inversion method is used to cope with the residual vibrations and the crosstalk.

In chapter 4, an experimental-based control is proposed with a printhead in the loop. The drop properties are measured using a high-speed camera. An image of the time history of the drops traveling from the nozzle plate to the printing medium is recorded. Based on this image, an image processing technique is developed to retrieve the actual velocity of each drop. The input pulse is optimized such the the error between the actual drop velocity and desired drop velocity is minimized. A novel jet pulse structure is proposed to cope with single channel residual vibrations, crosstalk, and even generalize optimization over each bitmap to be printed.

Both approaches result in strongly reduced interactions. The results are experimentally verified and provide very valuable steps towards flexible and robust printing systems [33].

Chapter 3

Model-Based Feedforward Control for a DoD Inkjet Printhead

Feedback control is based on the ability to measure the controlled variable. In the inkjet printer, no sensors are available for online measurement of the system variables. Therefore, feedback control is not possible and a feedforward controller is the only appropriate solution for controlling the printhead. Although residual vibrations and crosstalk effects are large, these effects are lightly predictable and reproducible. Hence, a model-based feedforward controller can be appropriate for this case. With a rather good model of the dynamics of the printhead, the construction of a feedforward controller as the inverse dynamics of the plant is a reasonable choice. In this chapter, we present the implementation of an inverse-based feedforward controller to deal with the residual vibrations and crosstalk.

3.1 Introduction

Model-based feedforward inversion of system dynamics is usually used to design inputs that achieve high-precision output tracking, this input is referred to as the inverse input. The inversion technique is applied to several output tracking applications, for example, aircraft control, high-precision positioning of piezoelectric probes, and robotic tracking control.

Major difficulties in realizing a model-based inversion strategy are that the resulting controller may produce unbounded or oscillatory outputs. This problem occurs when the system is non-minimum phase. Moreover, the model-based inversion strategy is sensitive to model uncertainty. These difficulties have been addressed in the development of optimal-inversion techniques in [25]. In particular, the optimal-inversion technique proves useful to account for modeling errors by inverting only the system model in frequency regions, where the model uncertainty is sufficiently small [26]. Another challenge in implementing the optimal-inversion approach is that the resulting input tends to be noncausal [26]. This approach therefore requires the knowledge of the entire future trajectory of the desired output to compute the inverse input at the current time instant. The noncausality of the optimal input restricts the stable-inversion technique to trajectory-planning applications. This restriction is alleviated through the development of the preview-based approach to the stable-inversion technique [27], which obtains the inverse input by using a finitely previewed trajectory rather than the entire future desired trajectory.

In this chapter, we present the application of the optimal inversion technique to cope with the residual vibrations and the crosstalk. We start with a review of the basics of the model-based inverse control. After that, we present the application of the feedforward control to a single channel with simulation and experimental results. Finally, multi-channels inversion is addressed to cope with the crosstalk between the channels.

3.2 Inverse-based control

As mentioned, inverse systems play an important role in feedforward control design. This section reviews the main principles of the inversion-based approaches to find feedforward inputs that improve the performance of the inkjet printhead. The existing models for the inkjet printhead are linear or can be linearized. Therefore, in this section we present the inversion problem of a linear system. Consider the linear time invariant system,

$$\dot{x}(t) = Ax(t) + Bu(t), \tag{3.1}$$

$$y(t) = Cx(t) + Du(t), \tag{3.2}$$

where $x(t) \in \mathbb{R}^n$ is the system state, and where the number of inputs is the same as the number of outputs, $u(t) \in \mathbb{R}^m$ and $y(t) \in \mathbb{R}^m$. This implies that the system is square. The transfer matrix is given by

$$G(s) = C(sI - A)^{-1}B + D. \quad (3.3)$$

Definition 3.2.1. A square rational function $G(s)$ is invertible if there exist a square rational function $H(s)$ (of the same dimension as $G(s)$) such that

$$G(s)H(s) = H(s)G(s) = I \quad \text{for all } s \in \mathbb{C}.$$

In case of non-square systems, the concept of a left inverse and right inverse is introduced. A left inverse of $G(s)$ is defined as $H^L(s)$, with the property that $H^L(s)G(s) = I$. Similarly, the right inverse is defined as $H^R(s)$, with the property that $G(s)H^R(s) = I$. For feedforward control design, the right inverse is more valuable because $u(s) := H^R(s)y_d(s)$ computes the input that, when applied to $G(s)$, gives the output y_d . A non-square system has different number of inputs and outputs. If the number of inputs of G is larger than the number of its outputs, there is no unique solution for the right inverse problem.

3.2.1 dc-gain inverse

The simplest feedforward method is dc-gain inversion, where the feedforward input u_{ff} is computed as

$$u_{ff}(t) = [G(0)]^{-1}y_d(t),$$

where y_d is the desired output of G and $G(0) := -CA^{-1}B + D$ (assuming that A^{-1} exists) denotes the dc-gain of the system whose inverse (as a matrix) is assumed to exist here. This approach is suitable for slow desired trajectories, but results in a significant tracking error if the operating frequency is increased since the dynamics is not taken into account. Note that the maximum tracking error increases with both the amplitude of the desired trajectory as well as the frequency that needs to be tracked.

3.2.2 Pole-zero cancellation inverse

If the system dynamics are stable and minimum phase, i.e there are no poles and zeros in the open right half of the complex plane, then the inverse feedforward is obtained by inverting the system dynamics

$$U_{ff}(s) = G^{-1}(s)Y_d(s).$$

Note that $U_{ff}(s)$ and $Y_d(s)$ denote here the Laplace transforms of $u_{ff}(t)$ and $y_d(t)$. An important issue with the exact inverse is that the inverse G^{-1} may not be proper. That

means that for some entries of G^{-1} , the order of the numerator is higher than the order of the denominator.

If G^{-1} is non-proper, let R_d be the minimal integer such that

$$\frac{1}{s^{R_d}}G^{-1}(s) = [s^{R_d}G(s)]^{-1}$$

is proper. We then define

$$U_{ff}(s) = [s^{R_d}G(s)]^{-1}\hat{Y}_d(s) = [s^{R_d}G(s)]^{-1}s^{(R_d)}Y_d(s), \quad (3.4)$$

set $H(s) := [s^{R_d}G(s)]^{-1}$ and $\hat{Y}_d(s) := s^{(R_d)}Y_d(s)$.

Therefore, the desired trajectory y_d is assumed to be sufficiently smooth (at least R_d times differentiable with respect to time). Based on this assumption, a proper exact inverse is obtained as

$$U_{ff}(s) = H(s)\hat{Y}_d(s).$$

Note that if the system is non-minimum phase, $H(s)$ will be unstable. Indeed the non-minimum phase system zeros at the right half plane become the unstable poles of $H(s)$. Therefore, (3.4) will typically result in an unbounded feedforward input u_{ff} over time for any desired non-zero trajectory y_d .

3.2.3 Optimal inversion

The inversion problem is presented as the minimization of a quadratic-cost function. For a sufficiently smooth desired output $y_d \in \mathcal{L}_2$ the optimal inversion problem is to minimize the following cost function,

$$\mathcal{J}(u) = \int_0^\infty u(t)^\top Ru(t) + [y(t) - y_d(t)]^\top Q[y(t) - y_d(t)]dt, \quad (3.5)$$

where, $R \succ 0$ and $Q \geq 0$ are weighting matrices.

Frequency domain solution

The optimal inverse is obtained as a filter as developed in [27] that minimizes \mathcal{J} . Suppose that the system (3.3) is invertible as a rational operator. Hence, there exists a rational transfer matrix $G^{-1}(s)$ such that $G^{-1}(s)G(s) = I$. We assume that system (3.3) and its inverse are analytic on the imaginary axis.

Define

$$G_{opt}(s) := [R + G^*(s)QG(s)]^{-1}G^*(s)Q. \quad (3.6)$$

The feedforward control input $u_{ff} = u_{opt}$ is defined using a filter $G_{opt}(s)$ and the desired output y_d as

$$U_{opt}(s) = G_{opt}(s)Y_d(s) \quad (3.7)$$

Therefore, this optimal input $u_{opt}(t) = \mathcal{L}^{-1}(U_{opt}(s))$ minimizes $\mathcal{J}(u)$. Assume that $G_{opt}(s)$ is proper, by proper choice of R, Q , the inverse filter $G_{opt}(s)$ can be decomposed into a stable and anti-stable part,

$$G_{opt}(s) = G_{opt}^{st}(s) + G_{opt}^{as}(s), \quad (3.8)$$

where

$$G_{opt}^{st}(s) = C_{st}(sI - A_{st})^{-1}B_{st} + D_{st}, \quad (3.9)$$

$$G_{opt}^{as}(s) = C_{as}(sI - A_{as})^{-1}B_{as} + D_{as}, \quad (3.10)$$

with $A_{st}, B_{st}, C_{st}, D_{st}$ and $A_{as}, B_{as}, C_{as}, D_{as}$ represent the state space realizations of $G_{opt}^{st}(s)$ and $G_{opt}^{as}(s)$, respectively so

$$\lambda(A_{st}) \subset \mathbb{C}^- := \{s \in \mathbb{C} | \operatorname{Re} s < 0\}$$

and

$$\lambda(A_{as}) \subset \mathbb{C}^+ := \{s \in \mathbb{C} | \operatorname{Re} s > 0\}$$

The bounded solution to the optimal inversion problem is then obtained by convolving the desired output y_d with the stable part of G_{opt} forward in time and with the anti-stable part backward in time as indicated in the following lemma.

Lemma 3.2.1. *Let the desired output $y_d \in \mathcal{L}_2$ be defined for $t \in \mathbb{R}$, and $G_{opt}(s)$ is proper. Then the optimal inverse input $u_{opt}(t)$ that minimizes \mathcal{J} for all time $t \in (-\infty, \infty)$ is given by*

$$u_{opt}(t) = u_{opt}^{st}(t) + u_{opt}^{as}(t), \quad (3.11)$$

with $u_{opt}^{st} \in \mathcal{L}_2, u_{opt}^{as} \in \mathcal{L}_2$ be defined by

$$u_{opt}^{st}(t) = C_{st} \int_{-\infty}^t e^{A_{st}(t-\lambda)} B_{st} y_d(\lambda) d\lambda + D_{st} y_d(t), \quad (3.12)$$

$$u_{opt}^{as}(t) = -C_{as} \int_t^{\infty} e^{A_{as}(t-\lambda)} B_{as} y_d(\lambda) d\lambda + D_{as} y_d(t). \quad (3.13)$$

Proof. the complete proof is given in [27] □

The computation of the optimal inverse input (3.11) at a time t requires the knowledge of all future values of the desired output y_d (unless G_{opt} is stable). In particular, the computation of $u_{\text{opt}}^{as}(t)$ in (3.13) requires knowledge of all future values of the desired output $y_d(t)$ for the time interval $[t, \infty)$. For practical reasons, $u_{\text{opt}}^{as}(t)$ is often approximated by truncating the integral in (3.13), by using the information of the desired output during finite time interval $[t, t + T_p]$

$$\hat{u}_{\text{opt}}^{as}(t) = -C_{as} \int_t^{t+T_p} e^{A_{as}(t-\lambda)} B_{as} y_d(\lambda) d\lambda + D_{as} y_d(t). \quad (3.14)$$

Hence, with this approximation the finite-preview-based optimal inverse input is given by

$$\hat{u}_{\text{opt}}(t) = u_{\text{opt}}^{st}(t) + \hat{u}_{\text{opt}}^{as}(t). \quad (3.15)$$

Note that the finite-preview-based implementation leads to tracking errors. The tracking error can be made arbitrarily small by choosing a sufficiently large preview time T_p . In addition, this approach is highly sensitive to model uncertainties.

Optimal state-space solution

The frequency domain solution method described in section 3.2.3 assumes that the system is square (square G) and stable, and G_{opt} is proper. This is not usually the case. Moreover, it ignores the role of initial conditions. With the state space solution these assumptions are not necessary. In this section, we present a generalized state space approach that minimizes the cost function (3.5), where the role of initial conditions is included and without any conditions on non-minimum phase zeros or stability. This approach is also valid for non-square systems and does not need to assume that G_{opt} is proper.

Theorem 3.2.1. *Let $y_d \in \mathcal{L}_2$ be the desired output. Then the optimal inverse input $u_{\text{opt}}(t)$ that minimizes \mathcal{J} for all time t is given by*

$$u_{\text{opt}}(t) = F_1 x(t) + F_2 p(t) + L y_d(t), \quad (3.16)$$

where

$$F_1 := -\bar{R}^{-1}(B^\top K + D^\top Q C), \quad F_2 := -\bar{R}^{-1} B^\top, \quad L := \bar{R}^{-1} D^\top Q,$$

and

$\bar{R} := R + D^\top Q D$, $K = K^\top \geq 0$ is the solution of the algebraic Riccati equation (ARE)

$$A^\top K + K A - (B^\top K + D^\top Q C)^\top \bar{R}^{-1} (B^\top K + D^\top Q C) + C^\top Q C = 0$$

and $p(t)$ is the solution of (the anti causal) system

$$\dot{p} = -(A + B F_1)^\top p + (C^\top + F_1^\top D^\top) Q y_d, \quad p(\infty) = 0.$$

Proof. Consider the candidate Lyapunov function

$$\begin{aligned} V(x, p) &= \frac{1}{2}x^\top Kx + x^\top p. \\ \dot{V} &= \frac{1}{2}(\dot{x}^\top Kx + x^\top K\dot{x}) + \dot{x}^\top p + x^\top \dot{p}, \\ &= \frac{1}{2}(Ax + Bu)^\top Kx + \frac{1}{2}x^\top K((Ax + Bu) + ((Ax + Bu)^\top p + x^\top \dot{p}), \end{aligned}$$

by completing the squares and using the ARE

$$A^\top K + KA - (B^\top K + D^\top QC)^\top \bar{R}^{-1}(B^\top K + D^\top QC) + C^\top QC = 0,$$

we obtain after long mathematical manipulations,

$$\begin{aligned} \dot{V} &= -u^\top Ru - (y - y_d)^\top Q(y - y_d) + \frac{1}{2}y_d(Q - QD\bar{R}^{-1}D^\top Q)y_d - p^\top B\bar{R}^{-1}B^\top p \\ &\quad + \frac{1}{2} \left\| u + \bar{R}^{-1}(B^\top K + D^\top QC)x + \bar{R}^{-1}B^\top p - \bar{R}^{-1}D^\top Qy_d \right\|_{\bar{R}}^2 \\ &\quad + x^\top (\dot{p} + (A - B\bar{R}^{-1}(B^\top K + D^\top QC))^\top p - (C^\top - \bar{R}^{-1}(B^\top K + D^\top QC)^\top D^\top)Qy_d). \end{aligned}$$

Now set

$$\begin{aligned} \dot{p} + (A - B\bar{R}^{-1}(B^\top K + D^\top QC))^\top p - (C^\top - \bar{R}^{-1}(B^\top K + D^\top QC)^\top D^\top)Qy_d &= 0 \\ \Rightarrow \dot{p} &= -(A + BF_1)^\top p + (C^\top + F_1^\top D^\top)Qy_d, \end{aligned}$$

Then, the time derivative of V with be

$$\begin{aligned} \dot{V} &= -u^\top Ru - (y - y_d)^\top Q(y - y_d) + \frac{1}{2} \|u - F_1x - F_2p - Ly_d\|_{\bar{R}}^2 \\ &\quad + \frac{1}{2}y_d(Q - QD\bar{R}^{-1}D^\top Q)y_d - p^\top B\bar{R}^{-1}B^\top p, \end{aligned}$$

This equation can be written as

$$\begin{aligned} u^\top Ru + (y - y_d)^\top Q(y - y_d) &= \frac{1}{2} \|u - F_1x - F_2p - Ly_d\|_{\bar{R}}^2 - \frac{dV}{dt} \\ &\quad + \frac{1}{2}y_d(Q - QD\bar{R}^{-1}D^\top Q)y_d - p^\top B\bar{R}^{-1}B^\top p. \end{aligned}$$

Integrating both sides we obtain

$$\begin{aligned} \mathcal{J}(u) &= \frac{1}{2}x_o^\top Kx_o + x_o^\top p_o + \frac{1}{2} \int_0^\infty \|u - F_1x - F_2p - Ly_d\|_{\bar{R}}^2 dt \\ &\quad + \int_0^\infty \frac{1}{2}y_d(Q - QD\bar{R}^{-1}D^\top Q)y_d - p^\top B\bar{R}^{-1}B^\top p dt, \end{aligned}$$

which is minimized for

$$u^* = F_1 x + F_2 p + L y_d.$$

That completes the proof. \square

Since the desired output is only known during finite time interval $[0, T_{\text{end}}]$, an approximate solution on the time interval is given as

$$\hat{u}_{\text{opt}}(t) = F_1 x(t) + F_2 \hat{p}(t) + L y_d(t),$$

with

$$\dot{\hat{p}} = -(A + B F_1)^\top \hat{p} + (C^\top + F_1^\top D^\top) Q y_d, \quad \hat{p}(T_{\text{end}}) = 0.$$

3.2.4 Data-based inversion

For data-based inversion, the key point is to utilize the inverse of the system dynamics from the frequency-domain implementation scheme. A schematic diagram for the proposed approach is shown in Figure 3.1.

If $(U(jw), Y(jw))$ is the frequency response data, then a data-based estimate of the system transfer function is

$$G(jw) = Y(jw)U(jw)^{-1} \quad w \in \mathbb{R} \quad (3.17)$$

where $Y(jw)$ and $U(jw)$ are the frequency-domain representation of the system output and input respectively. The inverse frequency response of the system is obtained as follows

$$H(jw) = U(jw)Y(jw)^{-1} \quad w \in \mathbb{R} \quad (3.18)$$

Let the desired output $y_d(t)$ be periodic and have finite energy, i.e. $y_d \in \mathcal{L}_2$. Then the inverse input can be calculated in the frequency-domain as

$$U_{\text{inv}}(jw) = H(jw)Y_d(jw) \quad (3.19)$$

Finally the feedforward inverse input is transformed to the time-domain

$$u_{\text{inv}}(t) = \mathcal{F}^{-1}(U_{\text{inv}}(jw)) \quad (3.20)$$

with \mathcal{F}^{-1} is inverse Fourier operator.

This approach is based on measured data which makes it insensitive to model uncertainties. However, the measured data should be sufficiently rich to capture the system dynamics. The causality-related limitations in the model-based inverse control approaches do not exist with the data-based inversion control approach. Particularly, the data-based inversion approach utilizes the inverse of the system dynamics from a frequency-domain implementation scheme. Due to the properties of the Fourier transform, the inverse input (3.20) will be always bounded even in case of the inversion of a non-minimum phase system.

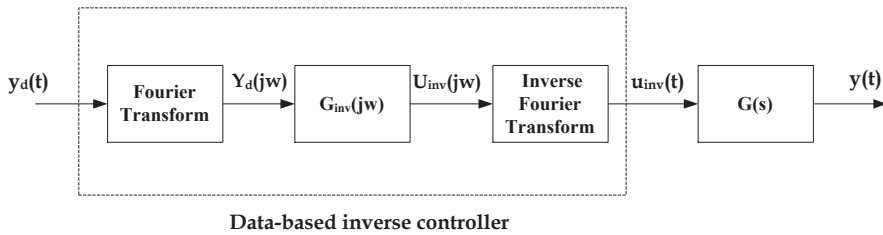


Figure 3.1: Data-based inverse control.

3.3 Control objectives

Our main concern is to improve the performance of an inkjet printhead with respect to productivity and drop-consistency. Improving the productivity is achieved by minimizing the effects of both the residual vibrations and the crosstalk. Drop-consistency is one of the most important performance issues. Currently, the drop-consistency requirement is only achieved at low jetting frequencies, 10-20 kHz. The jetting of any random bitmap yields large variations in the drop properties. These large variations originate from the residual vibrations and crosstalk, which are the major performance limiting factors when considering the drop-consistency.

Apparently, improving both the productivity and drop consistency require minimization of the residual vibrations and crosstalk. An inversion-based feedforward controller is employed to reduce the effect of the residual vibrations and crosstalk by perfect tracking of the reference trajectory.

3.4 Printhead model

Several analytical and numerical models, which describe the dynamics of the ink channel, are available in the literature [17]-[21]. In general, the numerical models are very accurate and they include high level of details. These models are usually finite element models in which the governing differential equations are numerically solved using complex meshes and numerical integration techniques. The main drawback of these models is that they have a very high computation time, typically 24 hours to analyze the jetting of one drop. That makes it not suitable for control design. On the other hand, analytical models are less complex since the governing differential equations are simplified to be solved analytically. Sometimes over-simplification results in models with poor accuracy while under-simplification leads to models with high complexity. Combined models that include both numerical and analytical models result in models with less computation time with a reasonable accuracy.

3.4.1 Lumped-parameter model

Lumped-parameter model adopts an equivalent electric circuit to describe the dynamics of the ink channel. This modeling technique is a useful and commonly applied analysis approach for designing piezoelectric inkjet systems. In this modeling framework, a single resonance is modeled with a capacitor, resistor, and inductor in series. Additional resonances are included by placing additional capacitor-resistor-inductor sets in parallel. The inductance represents the inertia, which is related to the fluid mass, the capacitance is a measure of fluid energy storage, and elasticity and the resistance is associated with any losses causing energy dissipation in the fluid, typically viscous losses. Accurate determination of the equivalent circuit parameters requires either a physical prototype or an accurate computational model to provide the data. In this model, it is assumed that the characteristic wavelength is larger than all dimensions in a channel. That means that the fluid in the flow direction is uniform at any instant in time. This assumption implies that the time required to transmit a change in the applied electric field on the piezoelectric actuator to a change in the meniscus shape at the nozzle is negligible. In [20], a transmission line model of the piezoelectric actuator, fluid chamber, and nozzle is proposed. This model permits analysis without the wavelength limitation and provides the ability to analyze the approximate interaction between multiple resonances in the complete system. However, this model still has a limited accuracy. Furthermore, a prediction error in the system response and the resonance frequencies may result from the assumption that the loss mechanisms are isolated to a single resistance in the motion component per resonance.

3.4.2 Two-port model

In [18], a two-port model is developed to describe the dynamics of the ink channel. This model employs the concept of bilaterally coupled systems. The ink channel is divided into subsystems, namely, reservoir, piezoelectric actuator, channel, connection, and nozzle. Each subsystem is modeled as a two-port system based on first principle modeling. To couple these subsystems, the Redheffer star product [24] is utilized. Consequently, the two-port model of an ink channel is obtained by connecting the subsystems and applying suitable boundary conditions. This model has less complexity and requires low computational time. However, due to the modeling error, this model cannot capture the first resonance frequency of the channel dynamics, which is the most important resonance frequency. Moreover, this model does not consider the interactions between an ink channel and its neighbors.

3.4.3 Narrow-gap model

The Narrow-gap model, proposed in [17], describes the dynamics of one ink channel based on the narrow channel theory. This model describes the dynamics of one ink

channel from the piezoelectric input voltage to the meniscus velocity. It also describes the interactions between one channel and five neighboring ink channels from the piezo input voltage $u(k) \in \mathbb{R}^m$ to the meniscus velocity $y(k) \in \mathbb{R}^p$.

The derivation of the narrow channel equations is based on the Navier-Stokes equations of motion and a continuity equation. The continuity equation results from the balance between the change in mass and the flux of mass in a control volume. The Navier-Stokes equation, which is the continuum version of Newton's second law, relates the inertial acceleration of particles of a fluid with internal and external forces that affect the channel.

In the narrow-gap model, the frequency response of the system is obtained using the swept sine technique. The frequency response of this model at a frequency ω_0 is computed based on solving the wave equations for a sinusoidal input with the same frequency ω_0 . The frequency response is computed by repeating the same procedure over a frequency range. The frequency response of the printhead is obtained as shown in Figure 3.2. The detailed derivation of this model is given in [17]. This model has a relatively low complexity. Since there is no sensor available to measure the meniscus velocity, we could not validate this model. Therefore, we have to assume that this model represent the dynamics of the ink channel with a reasonable accuracy.

3.5 Single-channel feedforward control

In [28], a model-based inverse feedforward controller is developed to design an input pulse for a single channel such that the initial values of the meniscus position and velocity are the same for all jetted drops. A reasonable assumption is that these initial values have to be zero at the starting of each input pulse. This is achieved by suppressing the residual vibrations. In this section, the optimal-inversion feedforward control is applied to damp the residual vibrations in one ink channel. For the inversion-based feedforward controller synthesis, a lower order transfer function is identified to fit the frequency response of the printhead, see Figure 3.3. Both simulation and experimental results are performed to investigate the performance of the proposed inverse control inputs and to compare with the performance of the currently used standard input pulse.

The choice of the reference meniscus velocity is a crucial issue since it is the link between the performance objectives and the adopted control objectives as explained in section 3.3. The drop properties highly depend on the meniscus velocity trajectory. However, it is not easy to find the relation between the resulting drop properties and the meniscus trajectory. Moreover, different meniscus trajectories might result in drops with similar properties due to the high nonlinearity, which is introduced by the jetting mechanism. Two important issues should be considered in the design of the reference meniscus trajectory. First, the reference trajectory should allow the refill of the channel, which requires not immediately to bring the channel at rest after the jetting of the drop.

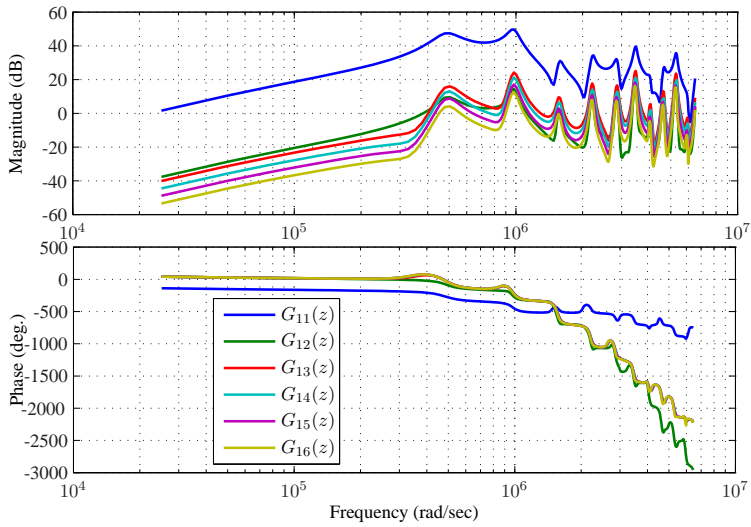


Figure 3.2: Frequency response of the narrow gap model. Mapping piezo voltage as input to meniscus velocity as output.

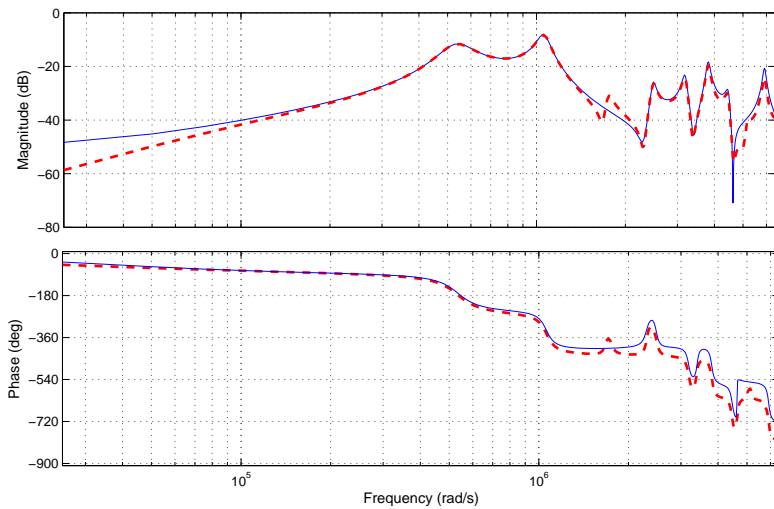


Figure 3.3: Frequency response of the narrow-gap model (dash-line) and the fitted transfer function (solid-line).

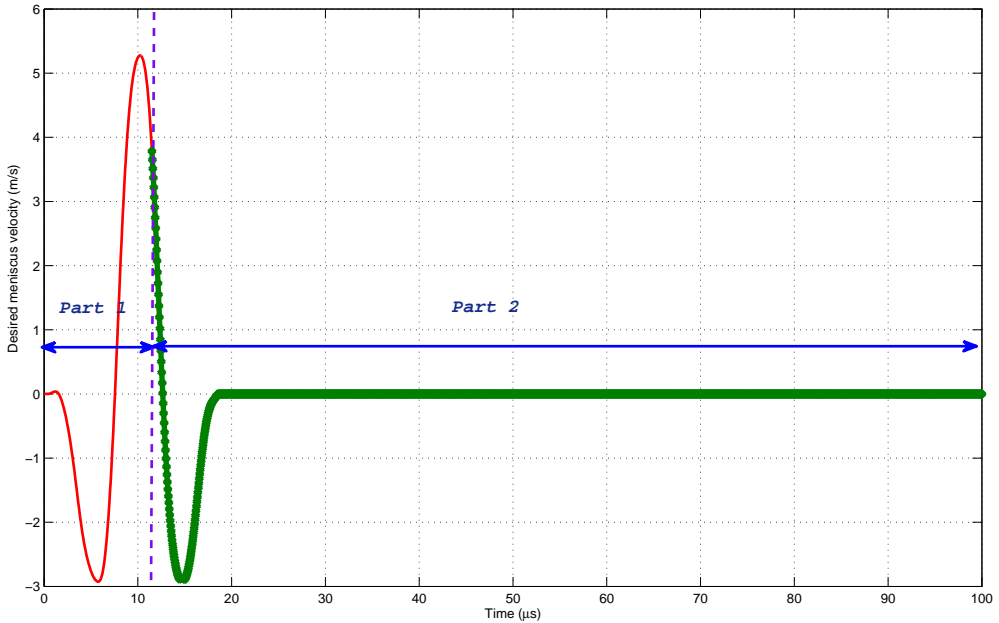


Figure 3.4: Reference meniscus velocity.

Secondly, the fluid dynamics should be brought gradually at rest to avoid a high input voltage. Therefore, as shown in Figure 3.4, the reference meniscus velocity is chosen to contain two parts, the first part determines the drop properties, drop velocity and volume, which are computed based on the response of the standard trapezoidal pulse. The second part is responsible for refilling the channel and after that the meniscus velocity is forced to settle at zero, to ensure zero initial condition of the subsequent drops. With the perfect tracking of the feedforward inverse control, the residual oscillations are damped out in time before the next pulse.

3.5.1 Simulation results

In this section, a SISO inversion-based feedforward control is implemented based on the narrow-gap model. Note that an ink channel shows a non-minimum phase behavior, which can be observed in Figure 2.9. Therefore, we implement the optimal inverse controller, as explained in section 3.2.3. Based on the optimal tracking of the feedforward inverse control, the residual oscillations will be damped out. The synthesis of the inversion-based feedforward controller includes identification of a lower order transfer function to fit the frequency response of the printhead, as shown Figure 3.3. The identified transfer function of the ink channel has an order of 16 and 4 non-minimum phase zeros.

We compare both the model-based input with the standard pulse in Figure 3.5. The feedforward input includes an additional negative pulse, which brings the channel to rest at $20 - 25 \mu s$. On the other hand, fluid dynamics take around $100 \mu s$ to settle using the standard pulse. Thanks to the feedforward input, the attainable jetting frequency is increased to 50 kHz compared with 10 kHz. For frequencies higher than 50 kHz, overlapping of the input is needed.

Figure 3.6 shows the simulation results of jetting 10 drops at 40 kHz. For the standard pulse, the meniscus velocity does not quickly come to rest after jetting a droplet. Therefore, the initial meniscus state is non-zero before jetting the next pulse. This causes a difference in the velocity profiles of the subsequent drops, which is observed in Figure 3.6. As explained earlier in this chapter, the meniscus trajectory is a major feature and a changed meniscus velocity will result in drops having different velocities. The feedforward inverse inputs are able to highly damp the residual oscillations and ensure the same initial meniscus state for all subsequent drops. The difference in the velocity profiles of the proposed inverse input is negligible. Consequently, this controlled scheme will result in consistent drop properties for all drops.

3.5.2 Experimental results

The simulation results show that a considerable improvement can be achieved by implementing the feedforward inverse control. Thus, the proposed inverse feedforward control is applied to a real printhead and the results are compared with a standard pulse. We have fitted the feedforward input to a trapezoidal waveform. Since any arbitrary waveform can be generated using the waveform generator, we have applied both the original and fitted waveform. Both waveforms show very similar results. Therefore, we present here only the experimental results of the fitted waveform.

The time history on the time interval $[0, T]$ of the drop traveling from the nozzle plate to the paper are collected to analyze the performance of the printhead. Several experiments are carried out for various jetting frequencies ranging from 20 to 70 kHz and the performance of the printhead is analyzed in terms of the drop velocity. The drop velocity of jetting 10 drops over jetting frequencies 20 – 70 kHz is depicted in Figures 3.7-3.8, for the standard pulse and the model-based feedforward inverse input, respectively. The model-based feedforward input shows less drop velocity variation compared to the standard pulse.

The performance is evaluated based on the maximum drop velocity variation over the whole range of the DoD frequencies, the behavior of the first drop, and the maximum drop velocity variation at each DoD frequency.

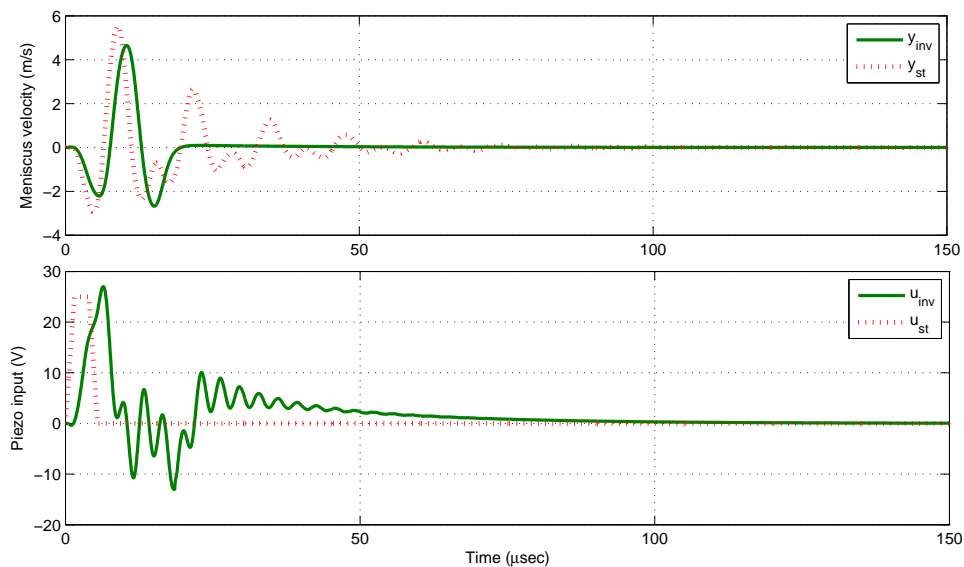


Figure 3.5: System response for jetting one drop (simulation).

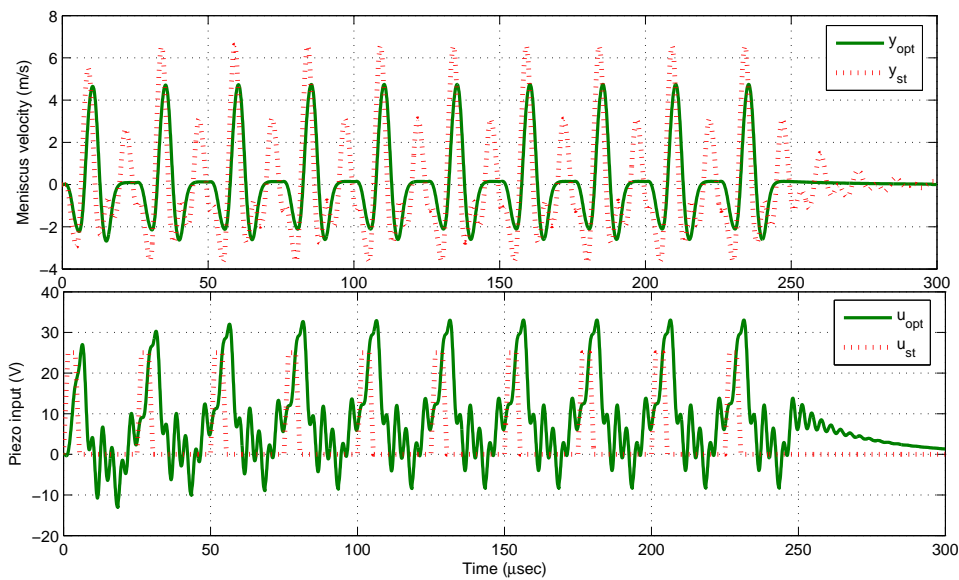


Figure 3.6: System response for jetting 10 drops at 40 kHz (simulation).

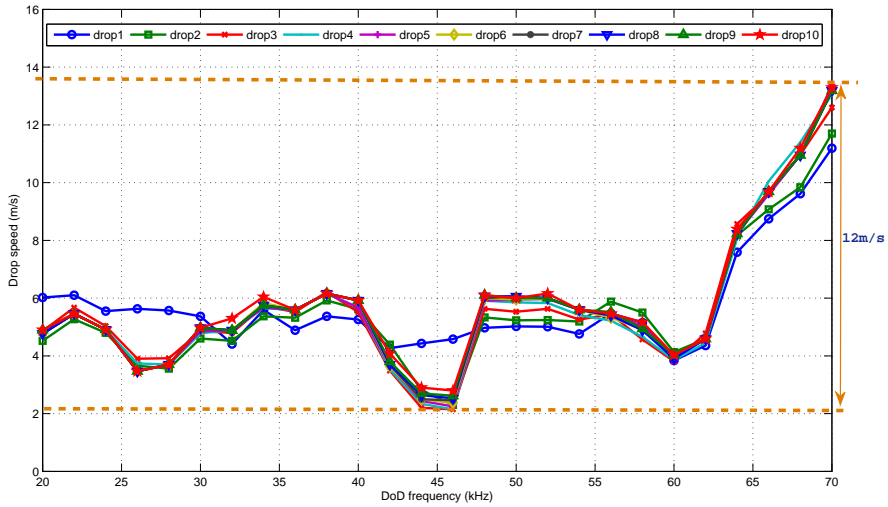


Figure 3.7: Jetting 10 drops at different DoD frequencies, 20–70 kHz using the standard pulse.

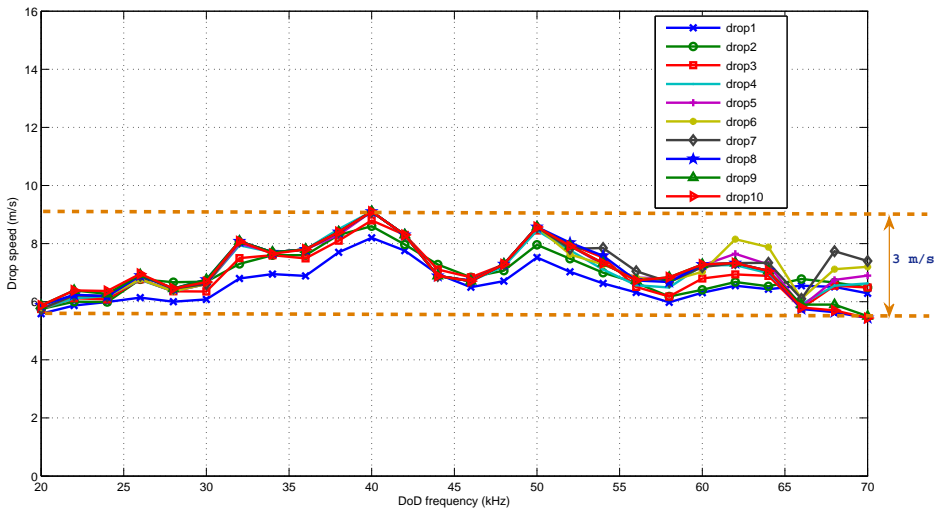


Figure 3.8: Jetting 10 drops at different DoD frequencies, 20 – 70 kHz using the model-based feedforward pulse.

For the standard pulse, the drop velocity varies from 2 to 13.5 m/s, which is a considerable variation over the whole DoD frequencies. Figure 3.7 shows that the first drop behaves in a completely different manner compared to the subsequent drops. At 65% of the frequencies, the first drop is faster than the remaining drops. As a consequence, a poor printing quality is obtained and a shadow appears in the printed bitmap. Moreover, the maximum drop velocity variation at each jetting frequency is around 3 m/s, which is calculated as

$$\Delta v_{max} = \max_f \Delta v(f). \quad (3.21)$$

with

$$\Delta v(f) = v_{max}(f) - v_{min}(f), \quad (3.22)$$

with

$$v_{max}(f) := \max_{t \in [0, T]} |v(t, f),$$

$$v_{min}(f) := \min_{t \in [0, T]} |v(t, f).$$

By applying of the model-based feedforward pulse, the drop velocity variation over the whole frequency range is reduced from 12 to 3 m/s. As depicted in Figure 3.8, the first drop behaves in a similar manner as the remaining drops. At each DoD frequency, all the drops have similar velocity. We compute the maximum drop-velocity variation based on (3.21) and it is less than 1.5 m/s.

The simulation results show very small variations in the drop velocity. That implies a flat DoD curve and less drop-velocity variations at each jetting frequency. However, the experimental results shows 3 m/s variations in the DoD curve. That is due to modeling errors and unmodeled dynamics. Improving the printhead model will result in a better pulse design and therefore less drop-velocity variations.

3.6 Multi-channel control

In this section, a MIMO inverse control is implemented for a DoD inkjet printhead. The narrow-gap model is utilized for MIMO inverse feedforward control synthesis purpose, since it describes the dynamics of six ink channels from the piezo input voltage $u(k) \in \mathcal{R}^m$ to the meniscus velocity $y(k) \in \mathcal{R}^p$. The frequency response of this model is shown in Figure 3.2. A low order stable transfer matrix $G(z)$ is identified to fit to the frequency response obtained from the narrow-gap model. The accompanying transfer

function $G(z)$ and from the piezo input voltage $u(k)$ to the meniscus velocity $y(k)$ is denoted as:

$$G(z) = \begin{bmatrix} G_{11}(z) & G_{12}(z) & \cdots & G_{1m} \\ \vdots & \ddots & \cdots & \vdots \\ G_{i1}(z) & \cdots & G_{ii}(z) & G_{im}(z) \\ G_{p1}(z) & \cdots & \cdots & G_{mm}(z) \end{bmatrix} \quad (3.23)$$

and satisfies

$$Y(z) = G(z)U(z) \quad (3.24)$$

where $G_{ii}(z)$ represents the dynamics of channel i , $G_{ij}(z)$, $j \neq i$ denotes the transfer function from the input of the channel i to the output of channel j , and $m = p = 6$. The transfer function (3.23) is discretized from the continuous model with sampling interval $0.1\mu sec$.

According to the assumption that all channels are identical and symmetric, the transfer matrix $G(z)$ is symmetric i.e. $G_{ij}(z) = G_{ji}(z)$ and diagonal terms are the same i.e. $G_{ii}(z) = G_{jj}(z)$ for $i \neq j$.

Figure 3.4 shows the reference meniscus velocity for one drop for one channel. If the actuation pulse, $u(k)$ [V], is designed such that the meniscus velocity, $y(k)$ [m/sec], follows the desired trajectory, $y_d(k)$ [m/s], then the channel will come to rest very quickly after jetting the drop. This will reduce the interaction between the jetted drops at higher jetting frequencies.

Several jetting bitmaps are tested, Figure 3.9 shows a sample of the tested bitmaps. This bitmap is transformed to a desired meniscus velocity with jetting frequency 50 kHz as shown in Figure 3.10. The preview time is chosen to include the whole jetting pattern. Figure 3.10 shows the response of the MIMO inverse feedforward control. It is clear that the residual oscillations have been highly damped using the feedforward input as shown in Figure 3.11. Moreover, the effect of the crosstalk is not visible in the system response. The perfect tracking of the designed feedforward input leads to improvement of the damping of the channel, which brings the channel at rest after jetting the droplet and, therefore, ensures the same initial meniscus state for all the subsequent drops. Therefore this will result in consistent drop properties for all drops.

The simulation results show that a considerable improvement in the printhead performance can be achieved by implementing the MIMO inverse controller compared with the performance of the standard pulse. Thus, the inverse input, shown in Figure 3.11, is applied to a real printhead and the results are compared with a standard pulse. The time history of the drops traveling from the nozzle plate to the paper are collected to analyze

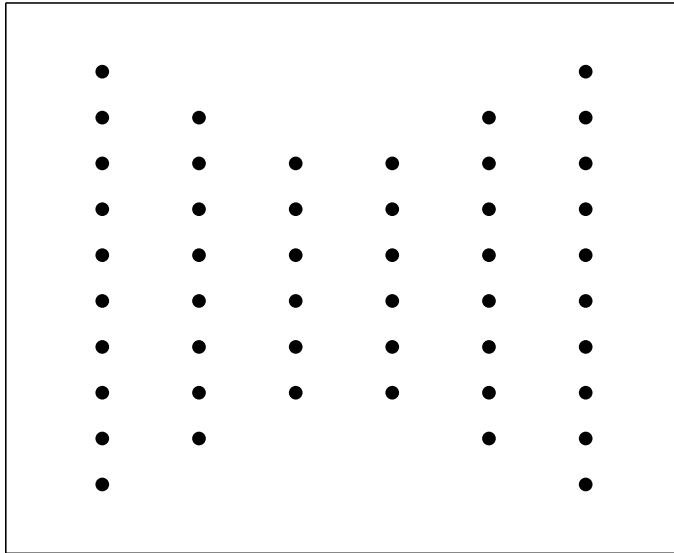


Figure 3.9: The bitmap to be printed.

the performance of the printhead. Figure 3.12-3.13 show the drop velocity of the jetted bitmap using the proposed MIMO inverse input and the standard pulse respectively. The performance is evaluated based on maximum drop velocity variation of the jetted drops. The maximum drop velocity variation is less than 1 m/sec for the inverse input while it is 2 m/sec for the standard pulse. The improvement in the drop velocity consistency achieved using the MIMO inverse has a great consequences on the print quality as depicted in Figures 3.14-3.15. Figure 3.14 shows the printed bitmap, which has regular pattern when compared with Figure 3.15. Using the feedforward input results in droplets with similar velocity and small position error of the dots. Only few drop are misplaced and merged together. On the other hand, the difference in the velocity of the drops printed by the standard pulse leads to large gap between the first two drops and the remaining drop. Moreover, many drops are merged together and form one large dot on the printing media.

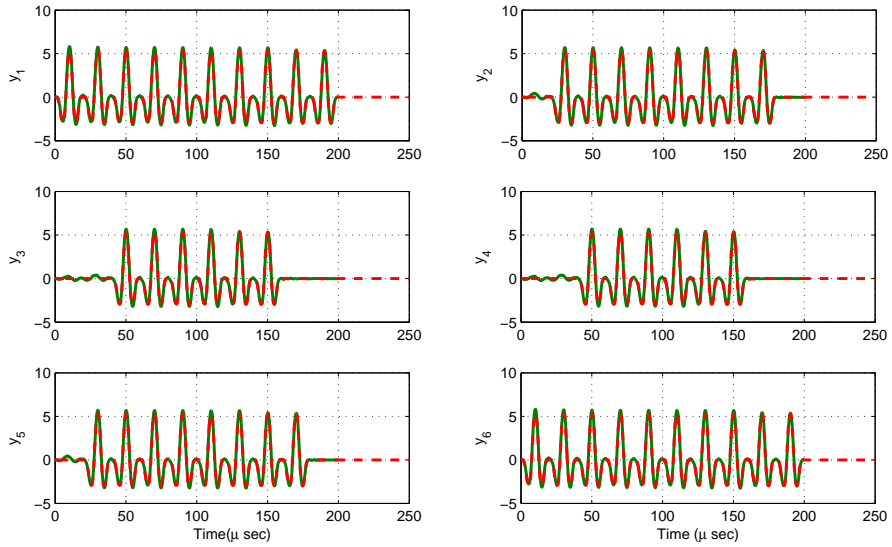


Figure 3.10: Reference meniscus velocity (dashed-line) and meniscus velocity using the proposed MIMO inverse feedforward input response (solid-line).

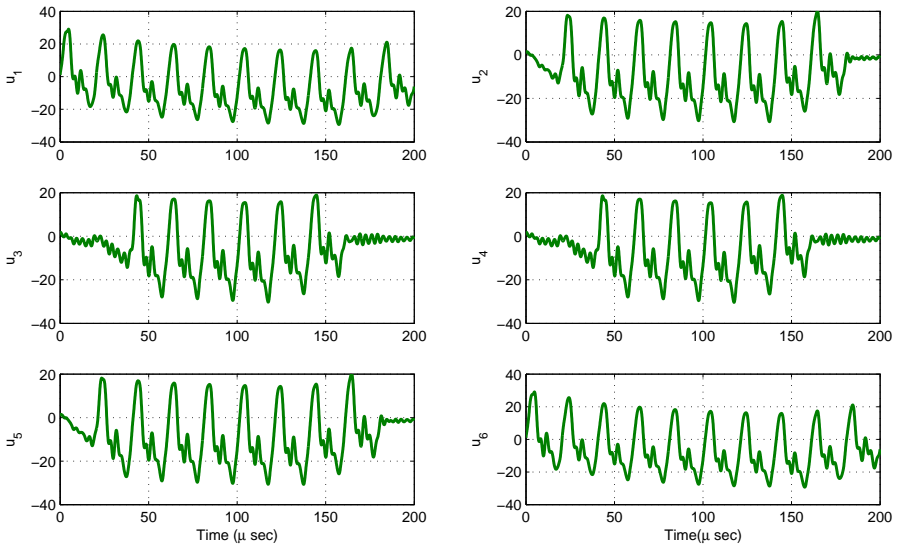


Figure 3.11: The feedforward control inputs.

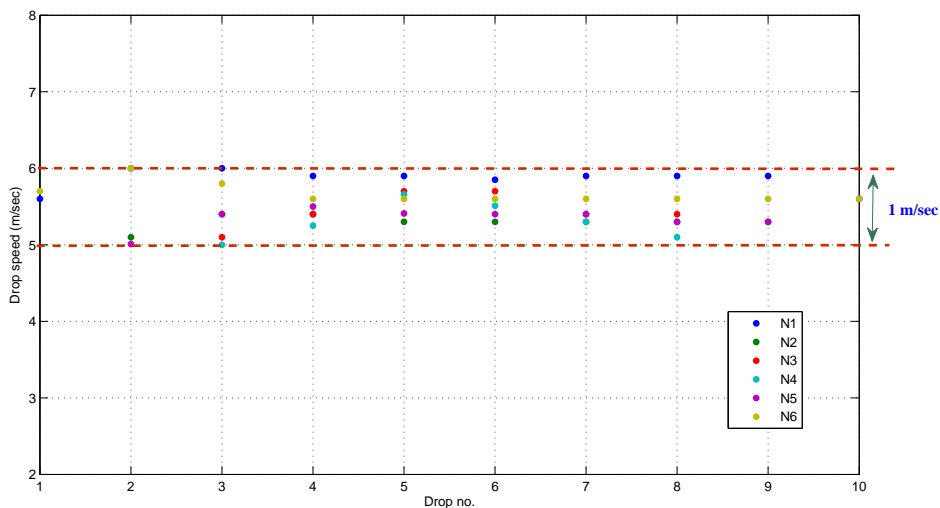


Figure 3.12: Optimal inversion: Drop velocity of the jetted bitmap for the 6 channels.

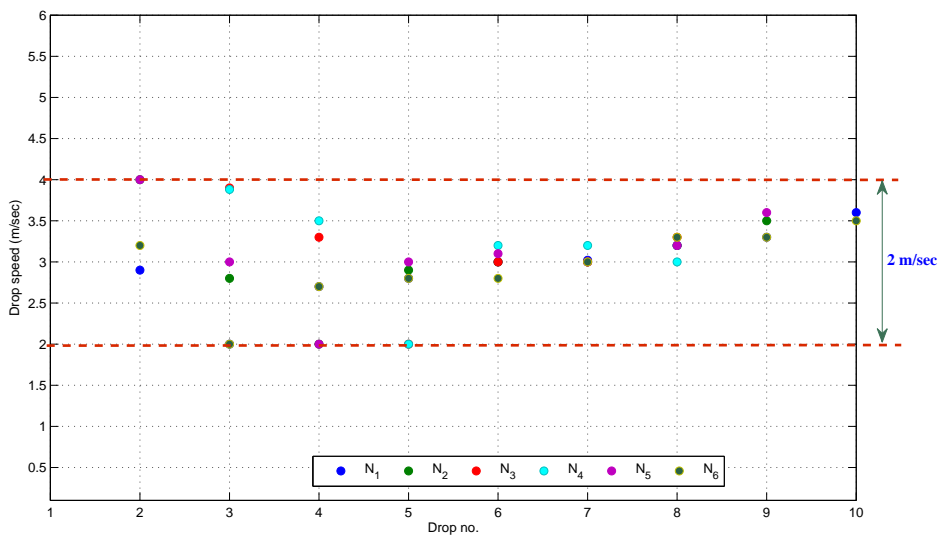


Figure 3.13: Standard Pulse: Drop velocity of the jetted bitmap for the 6 channels.

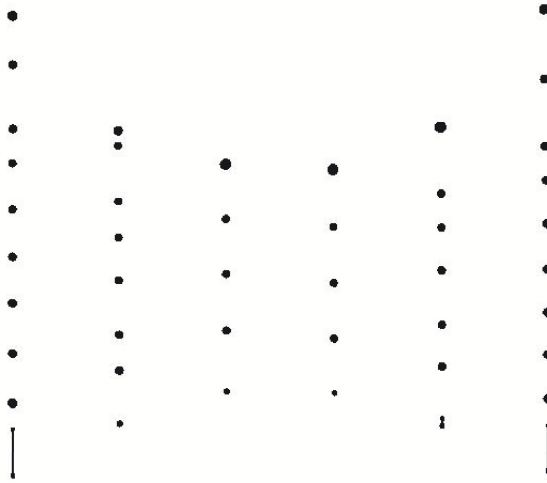


Figure 3.14: Printed bitmap using the proposed MIMO optimal inversion.

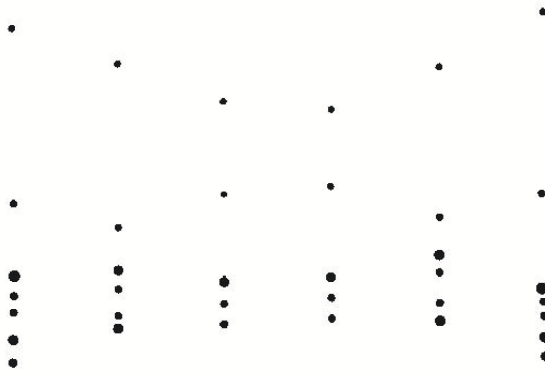


Figure 3.15: Printed bitmap using the standard pulse.

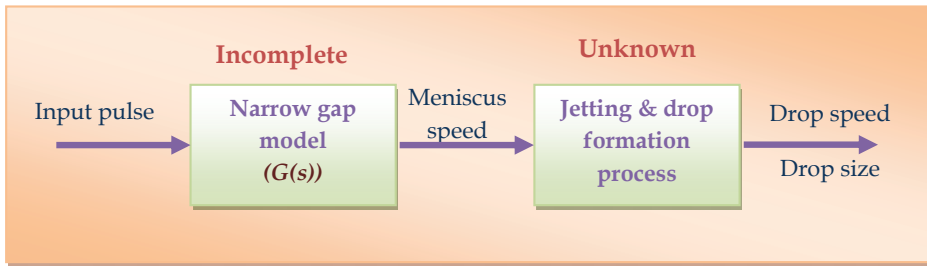


Figure 3.16: Schematic diagram of the inkjet printhead modeling.

3.7 Conclusions

It has been demonstrated that feedforward control is a suitable control strategy to overcome the residual vibrations and the crosstalk. Consequently, the printing quality of the inkjet printhead is considerably improved, beyond current achievements. The experimental results have shown the validity of the inverse-based feedforward approach. Although the implementation of the inverse-based feedforward control leads to a considerable improvement of the printhead performance compared to the current performance, the required performance is not achieved yet, the drop-velocity variations are still higher than 1 m/s. As illustrated in Figure 3.16, the main reason is that the design of the input pulse is based on a model, which is incomplete. The narrow-gap model does not predict the meniscus position, which has a major effect on the drop velocity. Moreover, this model does not include the refill dynamics of ink inside the channel after jetting a drop. The jetting process and drop formation dynamics are not considered in the design of the input pulse.

Chapter 4

Experimental-Based Control for a DoD Inkjet Printhead

In chapter 3, we have presented a model-based feedforward control technique using the narrow-gap model. Although the implementation of the model-based technique has a considerable improvement of the printhead performance compared to the current performance, the desired performance is still not achieved yet. The printing quality is related to the drop velocity, which is affected by the meniscus state (both meniscus position and velocity) at firing instant. The state at the firing depends on the previous pixels in the bitmap (pixels on/off). The narrow-gap model does not include the dynamics of the meniscus position. The model of the jetting process and the drop formation is unknown. Consequently, with the available models, a proper input pulse cannot be designed. Moreover, there is no sensor available to measure the meniscus state and, therefore, we cannot identify a model based on measured data. The only available sensor is the CCD camera, which is used to monitor the jetted drops. Therefore, in this chapter, we develop a vision-based control strategy where the drop properties, i.e. velocity and volume, are measured using a CCD camera and the input pulse is optimized directly using the experimental setup. The input pulse is parameterized as function of the two resonance frequencies and the damping factor of the printhead. Moreover, we show that using this pulse structure, one can efficiently cope with single channel residual vibrations, crosstalk, and even generalize to optimization over arbitrary bitmaps that need to be printed.

4.1 Introduction

Recently, process performance optimization has received a great deal of attention, since it naturally allows for reducing production costs, improving product quality, and meeting safety requirements and environmental regulations. Optimization is typically based on a model that is used by a numerical algorithm to compute the optimal solution. In practice, however, an accurate model of the complex processes can hardly be identified or derived with affordable effort. The system identification is further complicated because the system measured data are usually noisy and signals often do not have sufficient information to allow for efficient system identification [29]. Therefore, optimization using an inaccurate model might result in suboptimal solutions or, even worse, infeasible solutions when constraints are present. Model uncertainty results primarily from trying to fit a model of limited complexity to a complex process system. Two main classes of optimization methods are available to handle these uncertainties. The first one is *robust optimization*, where it is assumed that the problem data is uncertain and it is only known to belong to some uncertainty set. The optimization is then performed by considering the *worst case scenario* [30]-[31]. However, this kind of methods requires the optimization of a highly complex model and that the optimal solution may become conservative. The second optimization method is the experimental-based optimization. Instead of initially building a model, the experimental-based optimization uses experimental measurements directly in conducting the optimization for the printing quality control. However, an experiment is different from a model prediction in the sense that it costs more time during the iterations.

In this chapter, an experimental-based control strategy is developed to reduce the drop velocity variations due to the residual vibrations in case that a single channel is jetting. In [32], a new input pulse is presented, see Figure 4.1, which consists of two trapezoidal pulses, namely, a jetting pulse and a quenching pulse. The positive jetting pulse is used to form and jet the drop, however this pulse cannot damp the residual vibrations generated after jetting of the ink drop. Therefore, a negative quenching pulse is added to damp the residual vibrations. The optimal pulse parameters are obtained by solving an optimization problem, which minimizes the error between the actual drop velocity and a desired drop velocity. The drop properties depend on the bitmap to be printed. Therefore, based on the bitmap the input pulse is updated. The 0-pixel in the pattern will result in succeeding drops with different properties. The input pulse has to be updated based on the number of preceding 0-pixels in the pattern. Thus an optimization problem is formulated for several jetting patterns. This optimization problem results in a set of pulses, which reduces the drop velocity variations for any random bitmap.

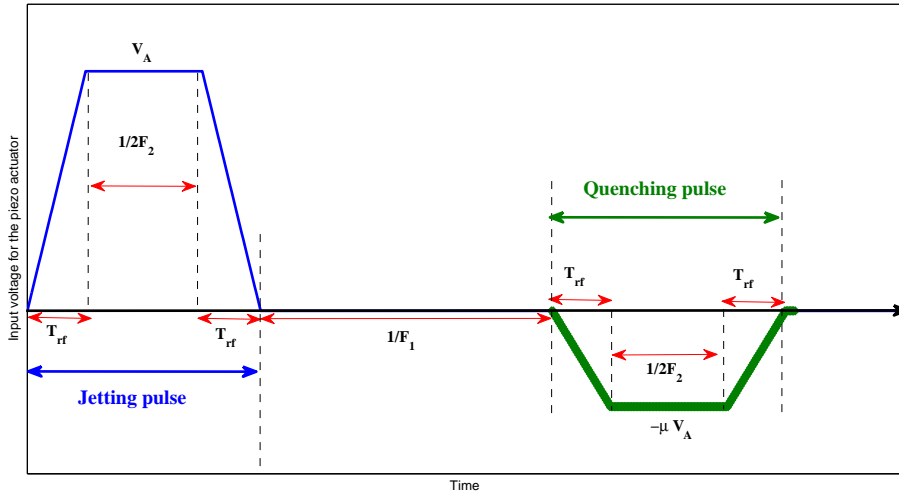


Figure 4.1: Parametrized input pulse.

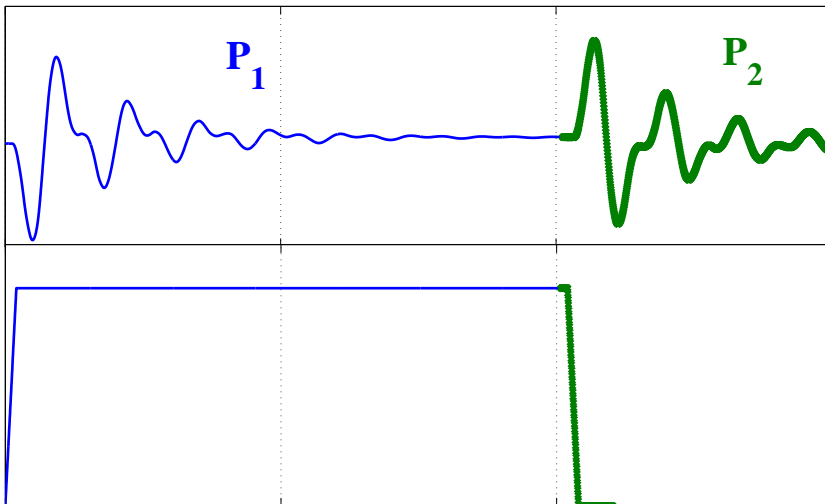


Figure 4.2: System response to the rising and falling edge of the input pulse.

4.2 Input pulse parametrization

Based on the physical effect of the input pulse parameters on the channel acoustics, the voltage pulse is parameterized as a function of two resonance frequencies and the damping factor of the printhead, see Figure 4.1. As explained in chapter 2, the jetting mechanism is related to the pressure wave of ink inside the channel. However, the pressure wave in ink generated by a waveform voltage is difficult to measure directly.

In the setup, a self-sensing signal from a piezoelectric, the PAINT signal, can be used to measure the pressure wave behavior in a single nozzle printhead. However, this signal has a very low signal to noise ratio, which makes this signal little accurate. The motion of the meniscus at the nozzle plate results from a pressure wave of ink generated from piezoelectric actuation.

The rising and falling times of the jetting pulse are used to generate the pressure wave inside the channel. The dwell time changes the relative phase of the generated pressure waves. At the rising edge, a negative pressure wave is generated, say P_1 , while a positive pressure is generated at the falling edge, say P_2 , see Figure 4.2. The rising and falling time of the jetting pulse is chosen to be the same to obtain the same characteristics of the pressure waves. To achieve the maximum pressure inside the channel and, therefore, the maximum drop velocity, the pressure waves, P_1 and P_2 , have to be in phase. If the pressure waves generated from the rising and falling times have the same period with half period phase shift, an amplified pressure wave will be generated as a sum of the two pressure waves P_1 and P_2 .

The period of the generated pressure waves is related to the jetting resonance frequency of the printhead, which is the second mode F_2 in the frequency response shown in Figure 3.3. Thus, the optimal dwell time of the pulse is chosen as half of the period of the second resonance frequency F_2 as shown in Figure 4.1. The amplitude of the jetting pulse is designed to jet a droplet with specific properties: drop velocity and drop volume.

For better printing performance, subsequent drops should not be jetted until the residual vibrations from the jetted drop have sufficiently damped out. These oscillations last for about $100 \mu\text{sec}$, which limits the maximum jetting frequency to 10 kHz. However, industrial applications require jetting at higher frequencies to achieve higher printing speed and/or higher print resolution. The quenching pulse is introduced to suppress the residual vibrations and, therefore, a higher jetting-frequency is obtained. To achieve perfect cancellation of the residual oscillations, the quenching pulse is chosen similar to the jetting pulse but with a negative sign. The optimal amplitude of the quenching pulse is equal to the amplitude of the resonating pulse multiplied by the damping factor μ of the printhead with opposite sign of the resonating pulse. The choice of the quenching time instant is very crucial. The quenching time should be chosen such that the

pressure wave generated by the jetting pulse is in anti-phase with the one generated by the quenching pulse. Therefore, the quenching pulse is placed at one period of the first resonance frequency F_1 . Both T_{rf} and V_A are chosen to achieve desired drop properties.

If the exact values of the two frequency modes and the damping factor are known, the optimal pulse parameters to cope with the residual vibration can be easily obtained. To validate this new pulse parameterization and our assumptions, the narrow gap model is used to show that the residual vibration will be damped. We know that in this model $F_1 = 78$ kHz, $F_2 = 160$ kHz and the damping factor is $\mu = 0.5$, by designing a pulse based on these parameters the residual vibration is highly damped as shown in Figure 4.3.

4.3 Experimental-based optimization

In this section, we present an optimization-based approach to obtain the optimal parameters of the input pulse, see Figure 4.1. In this approach, the optimization is carried out on a real setup instead of using a printhead model. A schematic diagram of the approach is illustrated in Figure 4.4. We will be concerned with improving the drop properties, mainly the drop velocity. Therefore, we optimize the input pulse based on the drop velocity. In this approach, a high-speed camera is used to capture the drop, which is traveling from the nozzle plate to the printing media. A time history of the jetted drop is obtained. Using an image processing technique, the velocity of the jetted drops is estimated. The input pulse is optimized such that the error between the measured drop velocity v_{actual} and a desired drop velocity $v_{desired}$ is minimized. The optimization process is done with a real printhead in the loop. No models are being used, hence all modeling issues are avoided. A schematic diagram of the approach is illustrated in Figure 4.4.

4.3.1 Image processing

Image processing refers to the use of different computer algorithms to extract or modify specific information in (digital) images. The purpose is to transform the digital image into another digital image which is usually used for image coding, image enhancement, image restoration, and/or image feature extraction [34]- [35]. In our approach, image processing is used for feature extraction. The goal of image feature extraction technique is to transform the image into another image from which specific image features can be derived.

Image based measurement has been widely applied in various kind of scientific applications as well as in many industrial and medical applications. The first scientific area that uses image processing is astronomy. In that area, the image processing techniques have

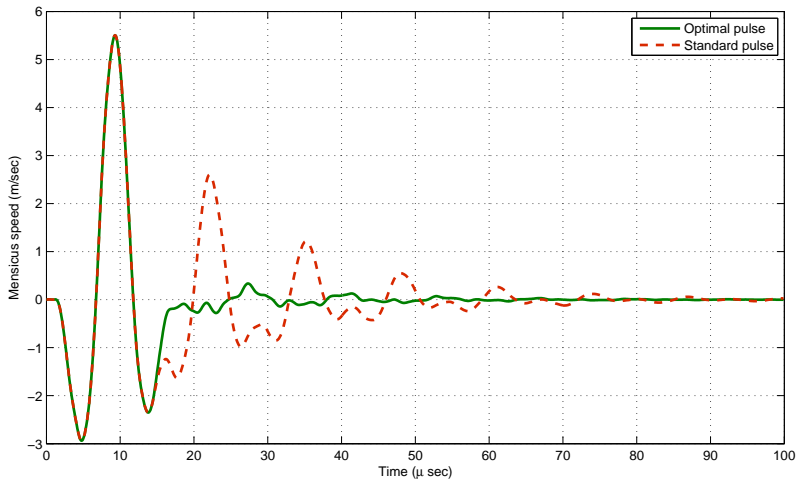


Figure 4.3: Simulation based on the narrow-gap mode.

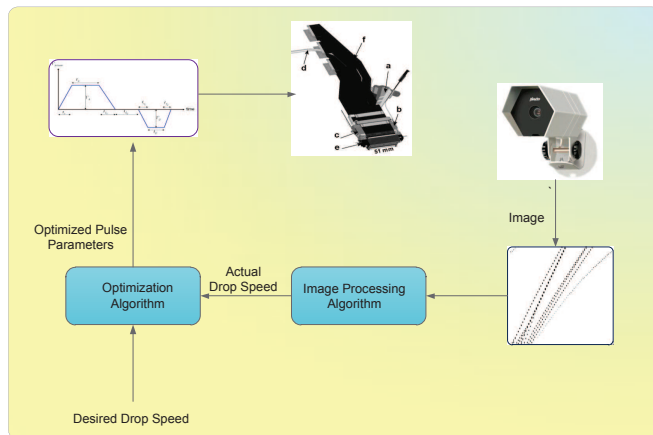


Figure 4.4: Experimental-based optimization feedforward control approach.

been used to improve the quality of the pictures of the moon. Nowadays, vision feedback control has been introduced as a popular technique to increase the flexibility and the accuracy of robotic systems [36]. For example, the aim of the visual servo approach is to control a robot using the information provided by a vision system. It involves visual tasks, which are used in real time control of a production system, or in autonomous vehicle guidance such as navigation and collision avoidance. Moreover, image based measurement is very useful in situations when it is not possible to use human vision, such as underwater inspections, or in heavy polluted or hazardous environments such as nuclear power plants.

In our approach, a high-speed camera is used to record the time history of the drops traveling from the nozzle plate to the printing media. An image processing technique is developed to retrieve the actual velocity of each drop. Two different samples of the time history of 5 drops are shown in Figure 4.5. These images illustrate the measured positions of drops with respect to the nozzle of the printhead as function of time. Both the jetted drops and small satellite drops are shown. The image processing algorithm extracts only informations of the jetted drops. Towards this objective, the image is converted into a binary image, which has only two possible values for each pixel. Typically the two colors used for a binary image are black and white, where a “0” is assigned for black and a “1” for white. After that, the image is filtered to remove the small dots that represent the satellites. The filter, used in our approach, creates a flat disk-shaped structuring element with a specific neighborhood. The neighborhood is defined as a matrix containing 1’s and 0’s; the location of the 1’s defines the neighborhood for the morphological operation. The center of the neighborhood is its center element. Based on the number of 1’s in the neighborhood, the image is filtered. Finally, a pattern recognition technique based on the 2D pixel search is developed to obtain the positions of each drop. Figure 4.5 shows examples of the time history of the five drops and the reconstructed image. Once the image is reconstructed, the velocity of each drop is computed based on linear fit of the drop position and the traveling time.

4.3.2 Optimization problem

Experimental-based optimization adopts experimental measurements as function evaluations for optimization. Points are iteratively generated by a proper algorithm that provides the direction of improvement for the decision variables. An optimization algorithm, which reduces the number of test experiments, is desirable.

As explained in section 4.2, the input pulse, see Figure 4.1, is parameterized with,

$$\theta := \text{col}(T_{rf}, F_1, F_2, \mu, V_A) \in \mathbb{R}^5.$$

with T_{rf} [μs] denotes the rise and fall time, V_A [V] is the jetting pulse amplitude,

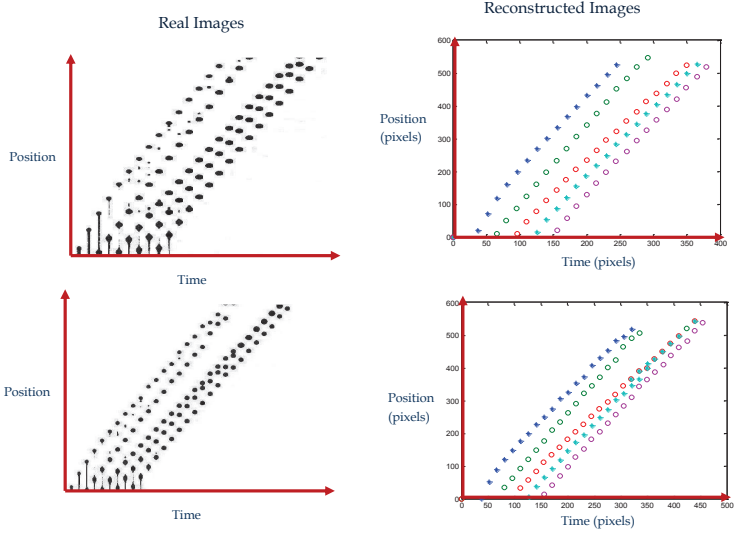


Figure 4.5: Input and output of the image processing algorithm.

F_1 [kHz] and F_2 [kHz] represent the first and the second resonance frequency of the printhead, respectively, and $\mu[-]$ is damping factor of the channel.

The optimization problem is defined as

$$\mathcal{J}(\theta) = \sum_{f=F_{min}}^{F_{max}} \sum_{t=0}^T (v_{desired}(t, f) - v_{actual}(\theta, t, f))^2, \quad (4.1)$$

subject to

$$\theta_{min} \leq \theta \leq \theta_{max}, \quad (4.2)$$

where f is the jetting frequency, which is the basic frequency of jetting a train of drops and it is sampled with sampling frequency 0.5 kHz, $v_{desired}(t, f) = 6m/s \forall t, \forall f$ is the desired drop velocity, v_{actual} [m/s] is the actual drop velocity, T denotes the total time of the experiment, and t is the time instant when a measurement is taken with sampling time $5 \mu s$. θ_{min} and θ_{max} denote the lower and upper bounds of the decision variables, respectively, which are defined as

$$\theta_{min} := col(0.5, 65, 150, 0.25, 12), \quad \theta_{max} := col(2, 85, 170, 0.75, 40).$$

The optimization is performed for jetting frequency range $[F_{min}, F_{max}] = [20, 60]$ kHz.

The optimal pulse that minimizes the cost function is given by

$$\theta_{opt} = \arg \min_{\theta} \mathcal{J}(\theta), \quad (4.3)$$

This problem formulation leads to a nonlinear optimization problem. A standard optimization algorithm is used to solve this constrained nonlinear optimization problem, which is not convex. The search algorithm can be generally categorized into two types, the gradient-based and gradient-free methods [37]-[39]. Gradient-based algorithms utilize gradients to provide search directions for improvement. The calculation of the gradient at a given point can be conducted by perturbations. Finite differencing is one method that is widely used for gradient calculations. Generally, gradient-based algorithms converge faster as the gradient leads to a good search direction for minimization. The gradient calculation based on the finite differences for the experimental-based optimization, however, needs a large number of experiments in case of a large number of decision variables. On the other hand, the gradient-free algorithm can be performed without computing the gradients, which in turn reduces the number of experiments required for the optimization. One of the standard gradient-free methods is based on Nelder-Mead simplex [40]. However, this technique is a heuristic search method that can converge to non-stationary points [41]. Therefore, we used a standard gradient-based algorithm to solve the optimization problem to minimize (4.1), namely, the trust region reflective algorithm [42]. This algorithm can efficiently handle the nonlinear constrained optimization problem. To avoid the algorithm getting trapped into a local minimum, the optimization problem is carried out several times using different initial values.

4.3.3 Experimental results

In this section, the optimized pulse is applied to a real printhead and the results are compared with a standard pulse. Several tests are carried out to evaluate the efficiency of the optimized pulse. Figure 4.6 shows the DoD drop velocity curve for the optimized pulse and the standard pulse. The DoD curve is the velocity of the drop at several jetting frequencies when the nozzle is continuously jetting. The drop velocity variation for the optimized pulse is less than 1.4 m/s compared with variations of 6 m/s in case of the standard pulse over the jetting frequency range 20-60 kHz.

We observe that the main contribution of the error is due to the low drop velocity at jetting frequencies between 20-32 kHz. The reason for the slow drop velocity at this frequency range could be that the two frequency modes, F_1 and F_2 , and damping ratio μ of the printhead are different at this frequency range. Therefore, we focus on optimizing a second pulse only over this frequency range, $F_{min} = 20$ kHz and $F_{max} = 32$ kHz, and we obtained a new optimized pulse for this range, the optimized parameters are summarized in Table 4.1.

	θ_1 (20-32 kHz)	θ_2 (32-70 kHz)
T_{rf}	1.5	1.5
F_1	78	78
F_2	160	165
μ	0.3	0.36
V_A	26	25

Table 4.1: Optimized pulse parameters

Now by defining two pulses, one for the low jetting frequency, 20-32 kHz, and another one for the rest of the jetting frequencies, the maximum drop velocity variation is less than 0.9 m/sec as shown in Figure 4.7. As depicted in Figure 4.8, the optimized pulse at the low-frequency range is not just a scaled version of the high-frequency optimized pulse. Note that the optimized pulses can be used for jetting drops with a DoD frequency up to jetting frequency 53 kHz without overlapping of the pulse. The sudden change in the DoD speed curve at the jetting frequency 53 kHz is due to hardware limitations since the waveform generator cannot overlap the pulses.

The second test is jetting a train of drops at several jetting frequencies and analyzing the time history of the drop traveling from the nozzle plate to the printing media. Figure 4.9 shows the time history of the train of drops for both the experimental-based optimized pulse and standard pulse, with a jetting frequency of 48 kHz. The Figure compares the experimental results of using the optimized pulse (4.9-a) with the standard pulse (4.9-b).

The application of the optimized pulse results in all the 16 drops traveling with the same velocity. The drops are disposed at an equal distance on the printing media. The first drop is, however, slower and therefore the drop is merged with the second drop. A small satellite drop is visible after the last drop. However, jetting with the standard pulse results in drops where the first drop travels to the printing media with high velocity, the subsequent drops travel with different velocities. Several drops are merged together into a single large drop. Consequently, the drops are misplaced on the printing media and have different sizes.

Several experiments are carried out for various jetting frequencies ranging from 20 to 70 kHz and the performance of the printhead is analyzed in terms of the drop velocity. The drop velocity of jetting 10 drops over jetting frequencies 20 – 70 kHz is depicted in Figures 4.10- 4.11, for the standard pulse and the vision-based feedforward optimized pulse, respectively. The vision-based feedforward pulse shows less drop velocity variation compared with the model-based feedforward input and standard pulse.

The performance is evaluated based on the maximum drop velocity variation over the whole range of the DoD frequencies, the behavior of the first drop, and the maximum drop velocity variation at each DoD frequency. The maximum drop velocity variation

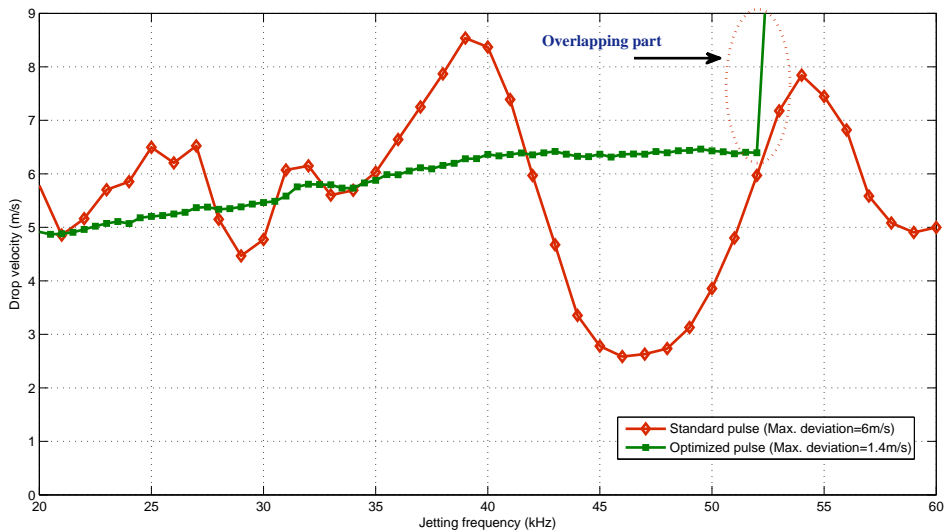


Figure 4.6: DoD curve comparison of the standard and optimized pulses

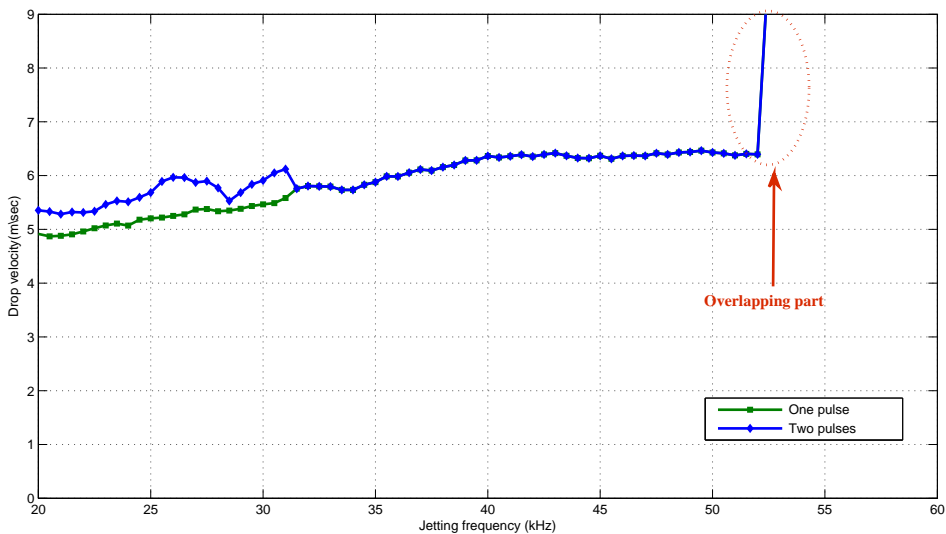


Figure 4.7: Optimized DoD curve with two optimized pulses.

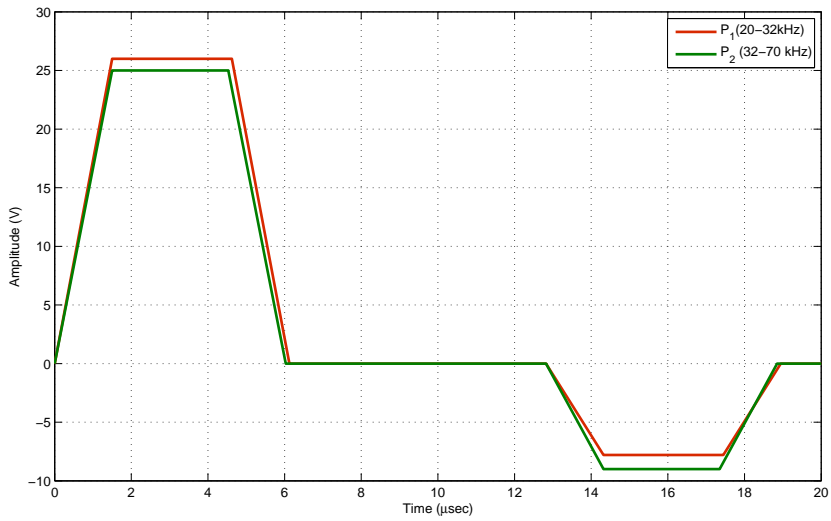
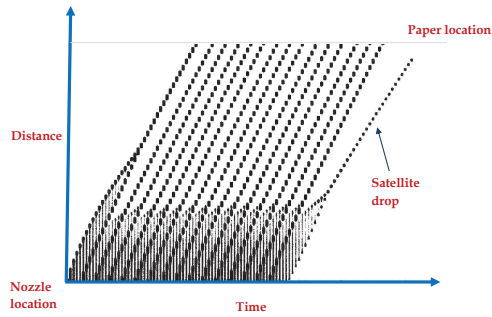
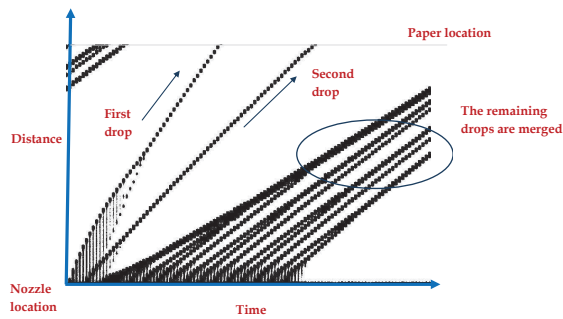


Figure 4.8: Optimized pulses based on vision-based optimization.



(a) Optimized pulse



(b) Standard pulse

Figure 4.9: Jetting 16 drops at a DoD frequency 48 kHz.

over the DoD frequencies is computed as

$$\Delta v_{DoD} = v_{max_{DoD}} - v_{min_{DoD}},$$

where

$$v_{max_{DoD}} = \max_f v_{DoD}(f), \quad v_{min_{DoD}} = \min_f v_{DoD}(f),$$

and $v_{DoD}(f)$ is the drop velocity with continuous jetting at frequency f .

For the standard pulse, the drop velocity varies from $v_{min_{DoD}} = 2$ to $v_{max_{DoD}} = 13.5$ m/s, which is a considerable variation over the whole DoD frequencies. Figure 4.10 shows that the first drop behaves in a completely different manner compared with the subsequent drops. At 65% of the frequencies, the first drop is faster than the remaining drops. As a consequence, a poor printing quality is obtained and a shadow appears in the printed bitmap. Moreover, the maximum drop velocity variation at each jetting frequency is around 3 m/s, which is computed as

$$\Delta v_{max} = \max_f \Delta v(f). \quad (4.4)$$

with

$$\Delta v(f) = v_{max}(f) - v_{min}(f), \quad (4.5)$$

with

$$v_{max}(f) := \max_{t \in [0, T]} |v(t, f),$$

$$v_{min}(f) := \min_{t \in [0, T]} |v(t, f).$$

A great improvement is achieved by implementing the vision-based feedforward pulse. The drop velocity variation, over the considered frequency range, is reduced to $\Delta v_{DoD} = 0.8$ m/s compared with $\Delta v_{DoD} = 12$ m/s for the standard pulse. Figure 4.11 shows that the difference between the first drop the subsequent drops is negligible. Therefore, a bitmap printed with the optimized pulse does not contain the shadow effect. At each DoD frequency, the figure shows that all the drops have similar velocity. The maximum drop velocity variation (4.4) is less than $\Delta v_{max} = 0.6$ m/s for the optimized pulse compared with $\Delta v_{max} = 3$ m/s for the standard pulse.

4.4 Multi-channel control

As inkjet channels become larger, the crosstalk between closely spaced firing channels becomes more severe resulting in an adverse impact on print quality. A method of

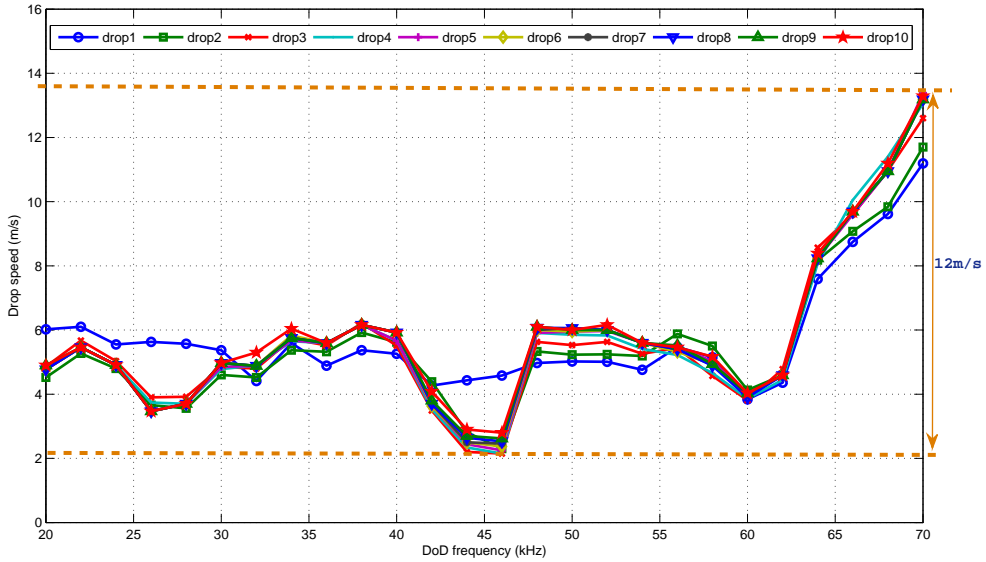


Figure 4.10: Jetting 10 drops at different DoD frequencies, 20 – 70 kHz using the standard pulse.

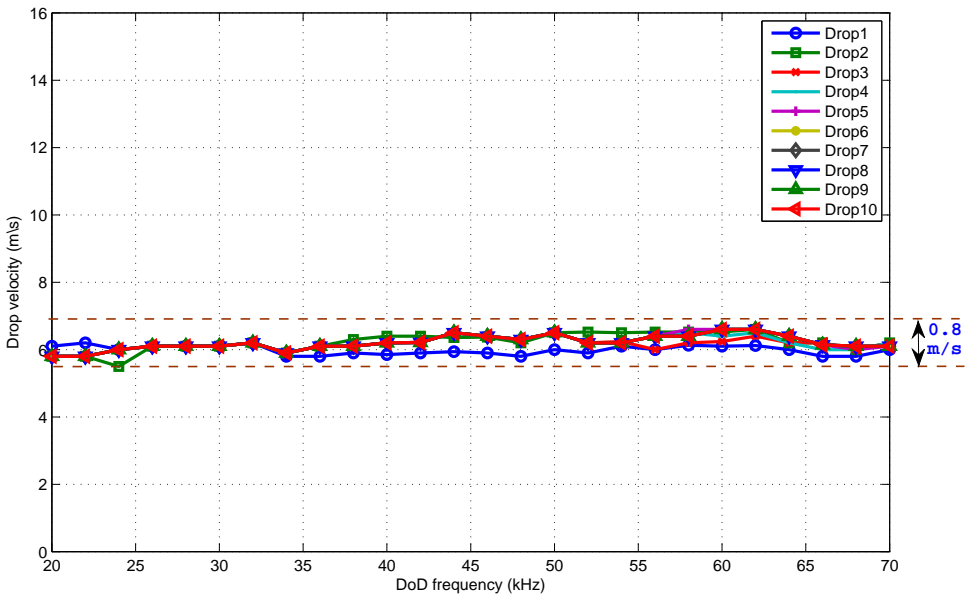


Figure 4.11: Jetting 10 drops at different DoD frequencies using the two optimized pulses.

addressing this problem, which is applicable to the DoD inkjet without any physical changes to the ink-channel design and with minimal changes to the channel configuration, is described. The individual channels are divided into N interspersed groups and the permitted firing time of each group has its own small time delay T_D . The time delay is optimized for each group such that when all channels are fired, a maximum amount of crosstalk cancellation is achieved. Because the firing channels are the source of the acoustic wave train, predominantly at a resonant frequency of the channel, the interaction with neighboring firing channels depends strongly on the phase relationship with the arriving wave. For a given printhead, several basic experimental measurements are carried out, and the data are used to calculate the change in drop velocity as a function of the delays for a channel near the center of the array when all channels are firing.

The inkjet printhead consists of an array of piezoelectric actuators, each of which may rapidly change the volume of an ink chamber. The objective is to minimize the crosstalk between the piezoelectric actuators. Towards this objective, an optimized time delay is included between the firing instant of the channels. In other words, the piezoelectric actuators are divided into groups and a time delay is applied between the inputs of these groups. For example, all the odd channels are fired and then after the time delay the even channels are fired. This delay scheme is known as a two-phase firing scheme. Another alternative is a three-phase scheme, where one third of the channels are fired simultaneously, after a time delay T_{d1} the second third of the channels are fired, and finally, the third group of channels is fired after time delay T_{d2} . Similar delay schemes, such as four-phase or five-phase schemes, can also be implemented.

4.4.1 Minimization of the crosstalk

In this section, we consider the two-phase firing scheme to minimize the effect of the crosstalk between the ink channels. Figure 4.12 illustrates the effect of crosstalk on the drop velocity. This figure shows the DoD velocity curve for one jetting channel and the DoD velocity curve of a center channel while 16 neighbors are jetting at several time delays. As depicted, the drop velocity is drastically decreased due to the crosstalk between the channels. Note that a time delay of $0 \mu\text{s}$ shows the influence of the crosstalk on the drop velocity. A time delay between the odd and even channels is considered and the time delay is varied from 0 to $5 \mu\text{s}$. The effect of crosstalk can be effectively reduced by the time delay, see Figure 4.12. As shown, the crosstalk effect depends on the time delay. When a proper value for the time delay is chosen, for instance $3 \mu\text{s}$, the deviations in the drop velocity are limited.

An optimization problem is formulated to obtain the optimal time delay between the odd and even channels to minimize the effect of the crosstalk. Since no precise model is available to describe the dynamics of the crosstalk between the channels, the optimization problem is formulated based on the measured data that are provided by the

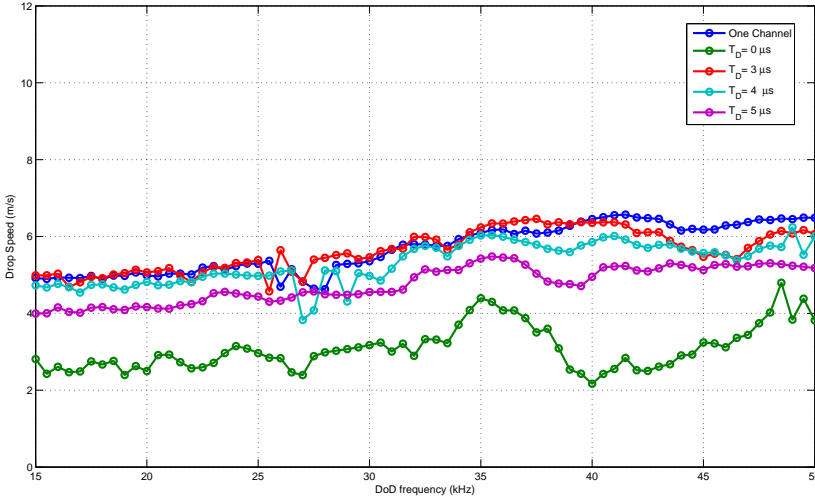


Figure 4.12: The DoD velocity curve with different time delays between the odd and even labeled channels.

high-speed camera. The objective is to minimize differences between drop velocity of the odd and even channels at all jetting frequencies.

Define the optimization problem as

$$\mathcal{F}(T_D) := \sum_{f=F_{min}}^{f=F_{max}} \sum_{t=0}^{t=T} (v_{odd}(t, f) - v_{even}(t, f))^2, \quad (4.6)$$

subject to

$$T_{D_{min}} \leq T_D \leq T_{D_{max}}, \quad (4.7)$$

where f is the jetting frequency, v_{odd} [m/s] is the odd channels average drop velocity, v_{even} [m/s] is average drop velocity of the even channels, T_D [μs] denotes the time delay between the jetting of the odd and even channels, T denotes the total time of the experiment, and t is the time instances when the measurements are taken with sampling time $5 \mu s$. $T_{D_{min}}$ and $T_{D_{max}}$ denote the lower and upper bounds of the decision variables, respectively, which are chosen as

$$T_{D_{min}} := 0 \mu s, \quad T_{D_{max}} = 5 \mu s.$$

The optimization is performed for jetting frequency range $[F_{min}, F_{max}] = [20, 60]$ kHz with sampling frequency 0.5 kHz.

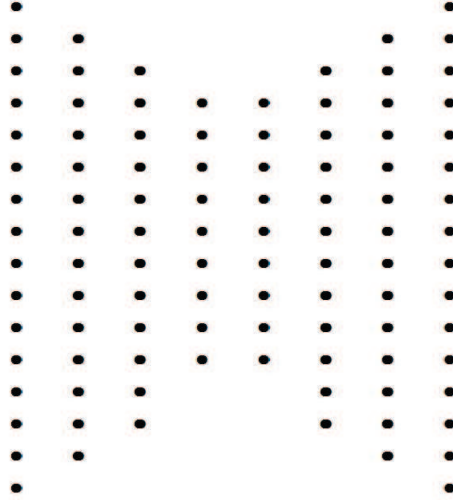


Figure 4.13: The bitmap to be printed. In this bitmap, we consider 8 nozzles jetting different number of drops at a DoD frequency of 48 kHz.

The optimal time delay that minimizes the cost function is given by

$$T_{D_{opt}} = \arg \min_{T_D} \mathcal{F}. \quad (4.8)$$

This optimization problem is a constrained nonlinear optimization, which is solved using a standard optimization solver. The optimization problem is solved with the printhead in loop. The results of this optimization problem are implemented in the next section.

4.4.2 Experimental results

A time delay of $T_d = 4\mu s$ minimizes the cost function (4.6) with 16 channels are jetting. The optimized pulse with the optimized time delay is used to jet several bitmaps, a sample of these bitmaps is shown in Figure 4.13 with jetting frequency 48 kHz. The time history of the drops traveling from the nozzle plate to the printing media are collected to analyze the performance of the printhead. Figures 4.16-4.17 show the drop velocity of the jetted bitmap using the optimized and the standard pulse, respectively.

The performance is evaluated based on the maximum drop velocity variation of all jetted drops. At a given jetting frequency of the bitmap, we compute the maximum drop velocity variation as

$$\Delta v_{max_{bitmap}} = v_{max_{bitmap}} - v_{min_{bitmap}}, \quad (4.9)$$

where

$$v_{max_{bitmap}} := \max_{t \in [0, T], n=1, \dots, \mathcal{N}} |v(t, n)|,$$

$$v_{min_{bitmap}} := \min_{t \in [0, T], n=1, \dots, \mathcal{N}} |v(t, n)|,$$

and $\mathcal{N} = 8$ is the number of jetting nozzles.

The maximum drop velocity variation is less than $\Delta v_{max_{bitmap}} = 1$ [m/s] for the optimized pulse, while the variation is $\Delta v_{max_{bitmap}} = 3$ [m/s] for the standard pulse. The overall improvement in the drop velocity consistency achieved using the optimized pulse has a considerable influence on the print quality as depicted in Figures 4.14-4.15. Figure 4.14 shows the printed bitmap, which has a regular pattern when compared with Figure 4.15. The improvement in the drop velocity consistency, which is achieved using the optimized pulse, has a positive influence on the print quality. On the other hand, the large variations in the drop velocity, in case of the standard pulse, result in an unacceptable poor printing quality. Figure 4.15 shows that the first drop is faster than the subsequent drops and several drops are merged together and form drops with large volume. The original pattern cannot be retrieved from the printed bitmap.

4.5 Bitmap-based control

The trajectory in the phase plane of the meniscus position and meniscus velocity is input frequency dependent. For continuous jetting (so all 1's), the phase plane of the meniscus velocity and meniscus position will converge to a stable limit cycle. That limit cycle generates stable drops with stable volume and velocity, see Figure 4.18. When the jetting pattern includes 0-pixels the periodic behavior is destroyed, see Figure 4.19, and thus the stable limit cycle. It requires several jetting drops to converge again to the stable limit cycle. The convergence rate depends on the dynamics of the channel and of the input frequency. The measurements show that after 100 μ s the transient is damped out. Thus, with jetting frequencies above 10 kHz, there will always be transients. As jetting frequencies up to 100 kHz are desired for higher throughput / accuracy, any design of a pulse shape has to explicitly deal with these transients.

Our proposal is to sustain the limit cycle to preserve the correct values of the initial conditions (meniscus position and velocity) when a drop will be fired, independent of whether the previous pixel is on or off. Towards this objective, we propose a non-jetting pulse for a 0-pixel just before jetting a 1-pixel. This non-jetting pulse ensures that the trajectory in the phase plane is at the same position as when a drop is being jetted.

The measurements shown in Figures 4.18-4.19 are based on the wave model that is described in [19]. In this model, the behavior of the printhead is described with traveling

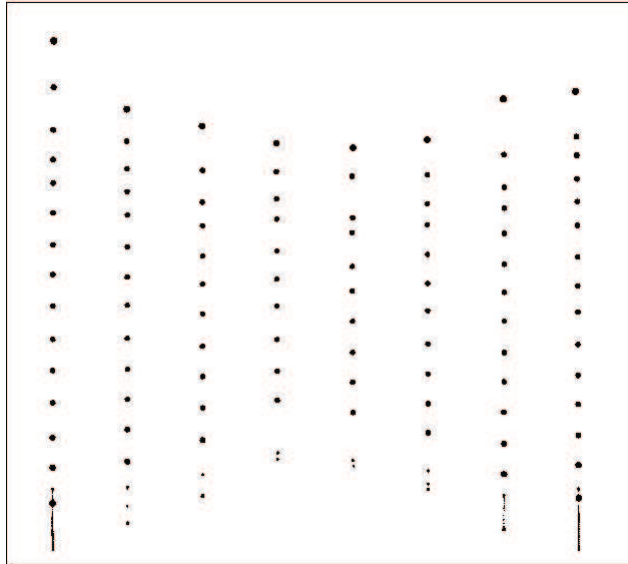


Figure 4.14: Printed bitmap using the optimized pulse.



Figure 4.15: Printed bitmap using the standard pulse. The variation in the drop velocity results in a poor printing quality. The first drop is faster than the subsequent drops, several drops are merged together and form drops with large volume.

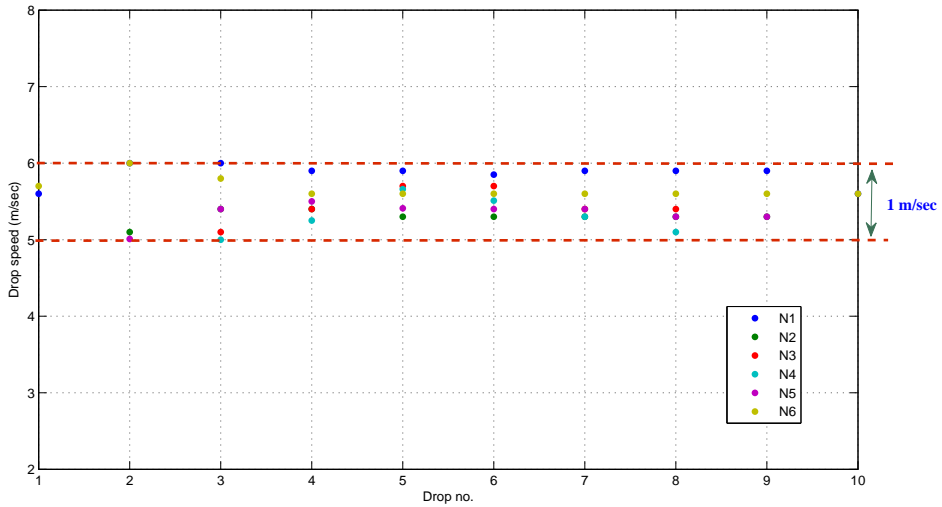


Figure 4.16: Drop velocity of the jetted bitmap for the 8 nozzles using the optimized pulse. The drop velocity variation is kept less than 1 m/s.

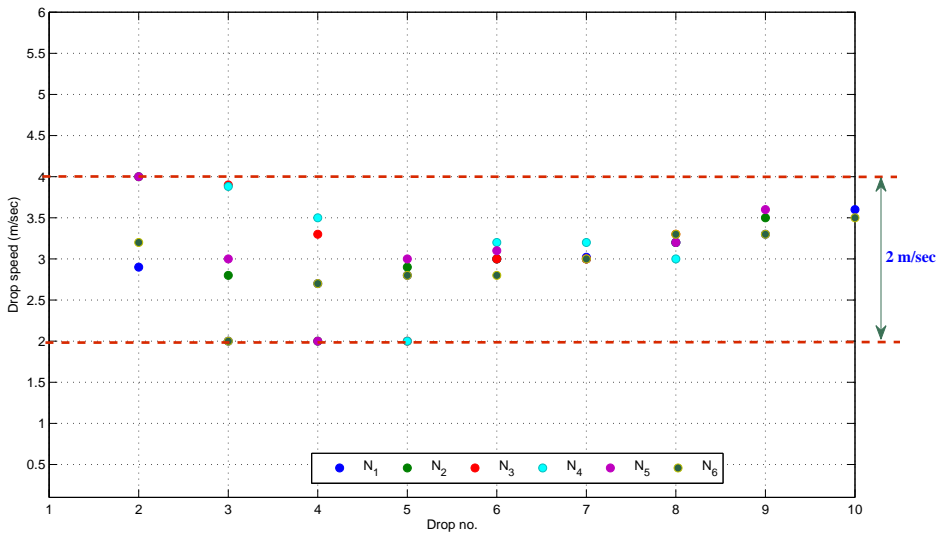


Figure 4.17: Drop velocity of the jetted bitmap for the 8 nozzles using the standard pulse. The drop velocity variation is around 3 m/s.

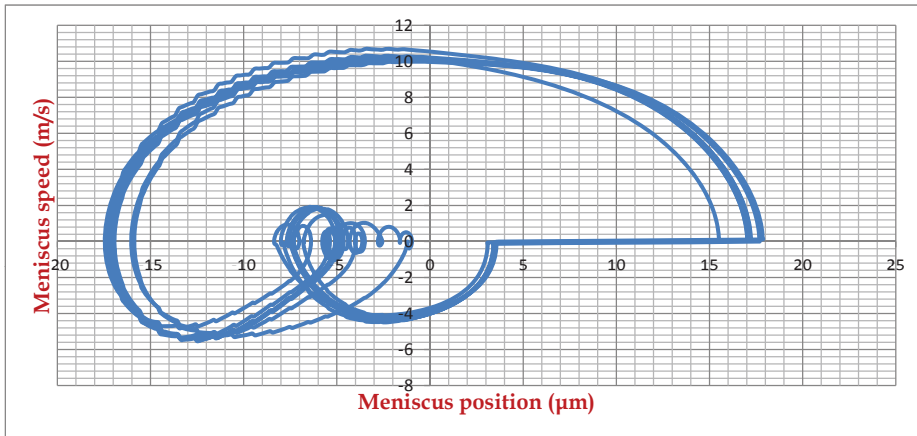


Figure 4.18: Phase plane for continuous jetting

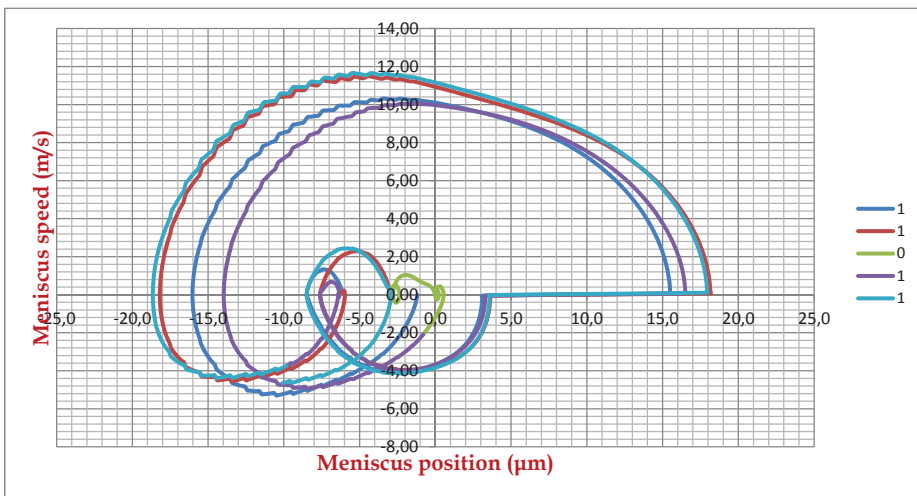


Figure 4.19: Phase plane for jetting pattern 11011

waves, which is used to solve the differential equations implicitly. The droplet formation is calculated simultaneously with the wave transport. This is a good link between the wave reflection at the nozzle and the flow in the nozzle. The main advantage of this model is that it takes the time-varying degree of filling of the nozzle into account. Moreover, this model can predict the meniscus state (velocity and position), which is useful to understand the behavior of the printhead. Here, we use this model to have more insight in the physics of the printhead.

As explained, the drop properties depend on the bitmap which is printed. Therefore, based on the bitmap the input pulse is updated. The 0-pixel in the pattern will result in succeeding drops with different properties. The input pulse has to be updated based on the number of preceding 0-pixels in the pattern. In our optimization problem, we consider a 4 pixels pattern and we optimize the input pulses for the 4th droplet taking into account all possible patterns of the preceding 3 pixels. Since the drop velocity of 4th pixel depends on the number of preceding 0-pixels, the optimization is simplified to only 4 cases. The four cases are 0001, 1101, 1001, and xx11.

We start with the pattern 0001 and we optimize the input of the 4th drop such that the jetted drop has a desired velocity. The resulting optimized pulse of the pattern 0001 is considered as an input for the first drop for the subsequent optimization problems. Figure 4.20 summarizes the optimized pulses and the corresponding patterns. We can distinguish 4 different pulses, 3 pulses are based on how many 0-pixels occur just before the 4th pixel. While the 4th pulse is used in case that 3rd pixel is 1 and independent on the first two pixels.

In Figures 4.21 - 4.22, we compare print quality when jetting an arbitrary bitmap with basic jetting frequency 52 kHz using the standard pulse and the optimized pulses, respectively. The standard pulse shows a poor printing quality and many drops are merged together and the jetting pattern cannot be retrieved. Using the optimized pulse with pattern adaptation, the quality of the print is improved. Thanks to the non-jetting pulse, there are no large differences in drop velocity between the low and high frequency drops. The maximum position error is improved to 0.15 mm compared with 0.4 mm for the standard pulse.

4.6 Conclusions

In this chapter, we have shown that the present physical models are not suitable for pulse design since these models do not include dynamics of the meniscus position, these dynamics play an important role in the prediction of the drop velocity. The DoD velocity curve optimization is not enough to improve the print quality since it neglects essential effects of 0-pixels in bitmaps. The state of the meniscus (velocity, position) at the start

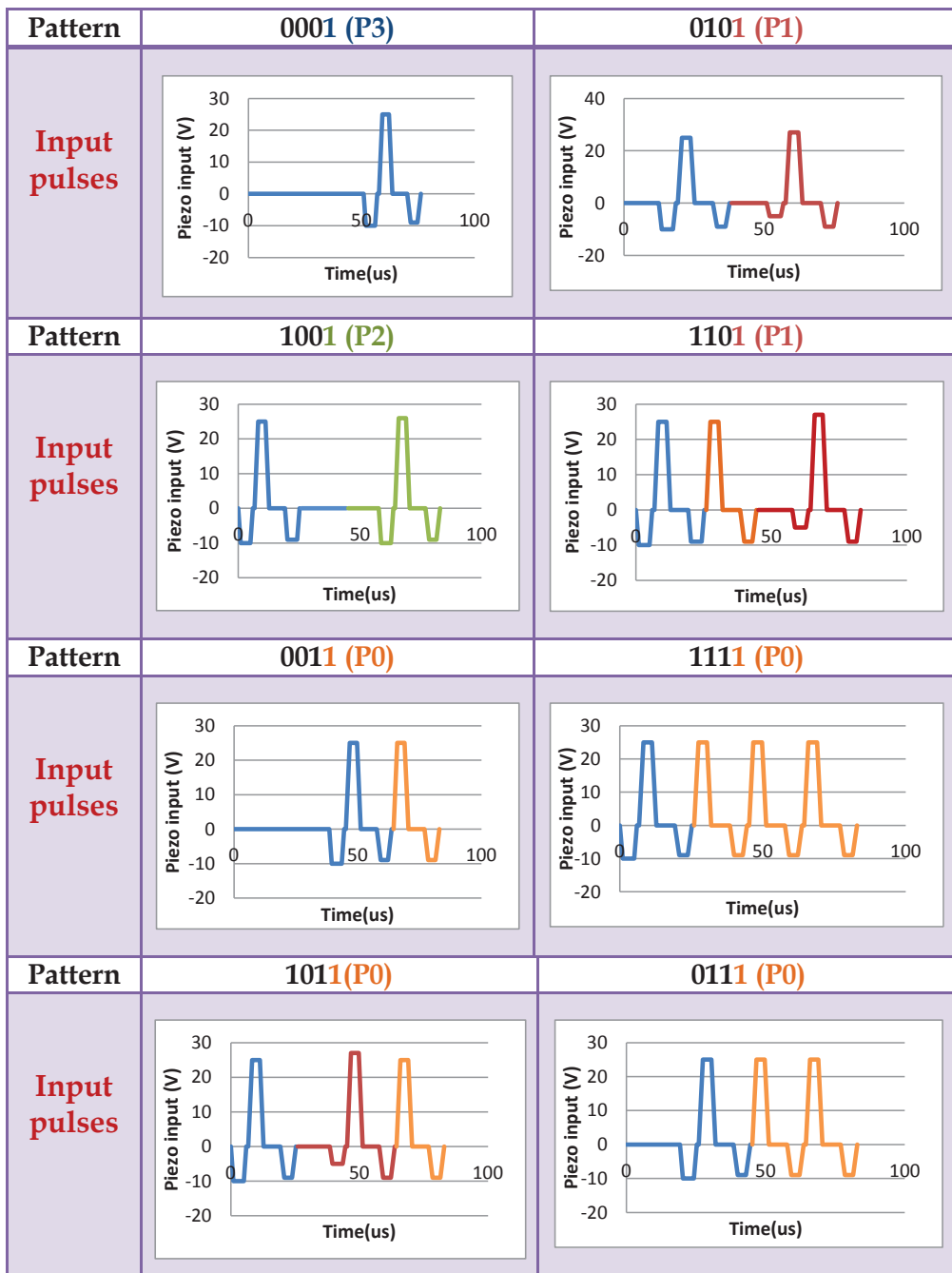


Figure 4.20: Optimized pulses for different jetting patterns

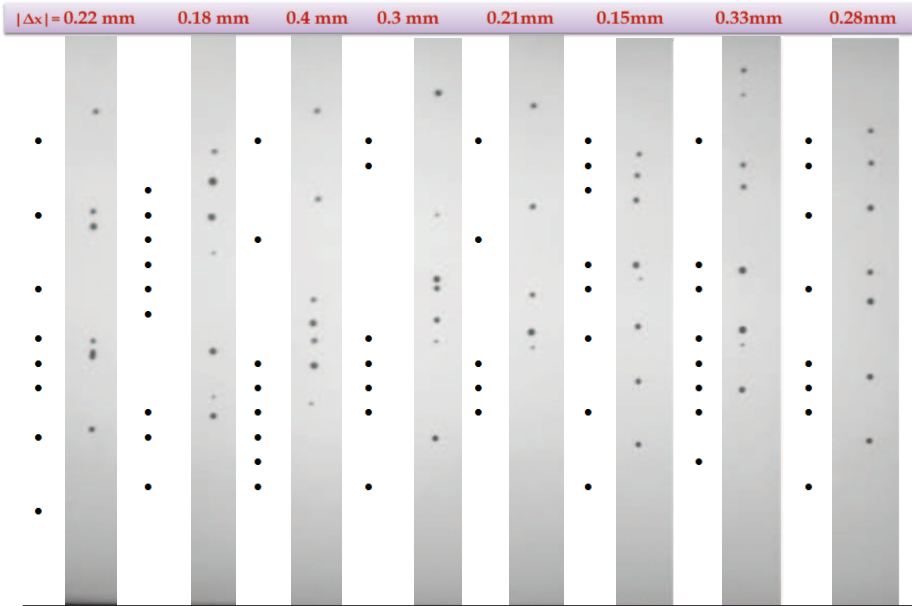


Figure 4.21: Printed bitmap using the standard pulse (desired bitmap, printed bitmap (gray))

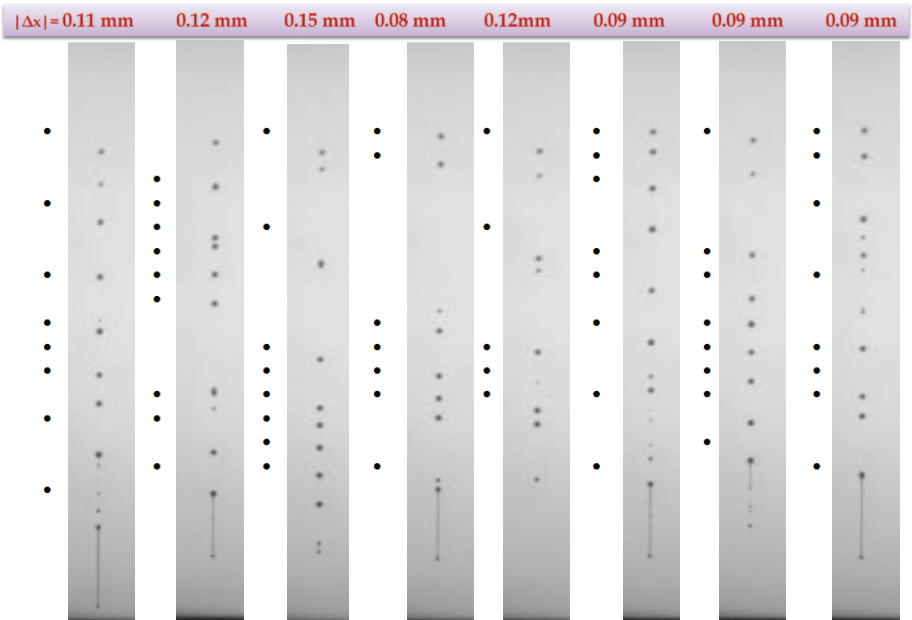


Figure 4.22: Printed bitmap using the optimized pulses (desired bitmap, printed bitmap (gray))

of the pulse influences the drop velocity considerably. Any pulse design has to guarantee almost the same initial meniscus state at firing a drop. An experimental-based optimization scheme is proposed to minimize the drop velocity variations. In this optimization, there is no need for an accurate model. The pulse design is based on controlling the drop velocity and not on an intermediate state. A new pulse parameterization is proposed. The input pulse is parametrized as a function of the physical properties of the printhead that leads to less optimization parameters.

Owing to this parameterization, online adaptation of the pulse is possible. Suppose that the PAINT signal (or meniscus velocity) is measured online. The damping factor μ and the two frequency modes F_1, F_2 are obtained by computing the frequency content of the measured variable and thus the pulse can be adapted online. We have demonstrated that dividing the channels into a number of groups and introducing a proper time delay between the actuation of the channels are sufficient to cope with the effect of the crosstalk between the channels. For jetting patterns containing zeros (0's), a non-jetting pulse is proposed to increase the velocity of the subsequent drop. Based on the jetting bitmap, a set of input pulses is optimized. Using these pulses result in less drop velocity variations for random bitmaps and, therefore, better printing quality. Different experimental results show the effectiveness of the optimized pulses.

Chapter 5

Professional Laser Printers

Laser printing systems have a great commercial success and currently drive an important segment of the printing market. The performance requirements become strict and have to be achieved under uncertain operating conditions, especially for color printing. Unfortunately, laser printing systems have not received widespread attention in the control system community. Nevertheless, control has played an important role in the evolution of printing systems. Today, high quality and high-speed laser printers with efficient power utilization is required. These printing systems should be able to print on several sizes of media, allow for media with different weights, automatically print on both sides of media and include stapling, booklet production, or other types of finishing. To maintain the printing quality, such printers should be adaptable with respect to variations in media and variations in timing parameters. In this chapter, we present an overview of the digital printing industry, give a brief description of the printing processes, we provide a heat flow model of the thermal aspects of printing process, and finally we identify a set of challenging control problems that are relevant to the printing process.

5.1 Introduction

Color document production systems are multifaceted systems whose quality highly depends on the appropriate combination of several design factors. The physical printing process involves multiple temperature set points at different places, precise electromagnetic conditions, transfer of toner through certain pressures and layouts, and many other technical considerations. The development of laser printers tends to achieve high printing quality with high printing speed.

The popularity of the laser printers results from their ability to print at high speed with high level of precision at relatively low cost. A laser can move very quickly, so it can write with much higher speed than an inkjet. Moreover, since the laser beam has a constant diameter, it can draw more precisely, without spilling any excess ink. On the other hand, laser printers tend to be more expensive than inkjet printers, but their running cost is lower. The toner powder is relatively cheap and it lasts for a long time. When they were first introduced, laser printers were too expensive to use as a personal printer. But now laser printers have become much more affordable, can print with speeds up to 200 pages per minute in black and white and around 100 pages per minute in color [43]. Very high-speed laser printing systems are competing in lithography in several commercial applications, such as mass mailings and personalized documents [44]. As technology advances, laser-printer prices continue to decrease, while performance improves. This will introduce several possibilities of new applications using laser printing.

5.2 Development of laser printer

In 1937, Chester Carlson invented the first dry copying process. After several experiments, the use of a Sulfur on zinc electrostatic medium and Lycopodium powder as a toner was recorded as the first successful experiment. However, it took several years before the first public announcement of *xerography* technology in 1948. The name *xerography* is derived from the Greek word for dry writing. In 1950, the first copier, based on the xerography technology, was available in the market. By 1960 the name of xerography changed to Xerox Corporation. The laser printer was invented by modifying an existing Xerox copier. The modifications included replacing the lens assembly with a laser and the paper imaging with a character generator. Gary Starkweather is generally credited as the inventor of the laser printer at Xerox research center in 1969 [45]. One year later, network functionality was incorporated in the laser printer. By 1977 the Xerox 9700 with built in Ethernet capabilities could print up to 120 pages per minute. At the same time, Burroughs developed an electrostatic printer in the early 1970s, which induced an image using a page width array of electrodes [43]-[46].

A faster xerographic printer was developed by IBM. This printer could print around

20,000 lines or 167 pages per minute on 28 cm forms. This printer had an optical forms overlay station in which the laser is only needed to write variable information. This printer was used for high-volume printing of documents such as invoices and mailing labels. It is often cited as "taking up a whole room," implying that it was a primitive version of the later known printers used with a personal computer.

In 1981, Xerox released the first innovative laser printer design for office use. However it was an expensive system that limits the purchasing to a relatively small number of institutions and businesses. With the widespread use of personal computers, the first laser printer intended for a mass market was the Hewlett Packard *LaserJet I*, which was released in 1984. The HP LaserJet printer was quickly followed by several laser printers from Brother Industries, Apple, IBM and others. First-generation printing machines consisted of large drums that are photosensitive, with circumferences larger than the length of the paper. When the coatings were developed, the drums contact the paper multiple times in a pass, and therefore became smaller in diameter. Thanks to laser printers, fast and high quality text printing with several fonts and sizes on a page were brought to the business and consumer markets. With the rapid developments of the electronic technology, the price of laser printers has been considerably reduced over the last years.

5.3 Description of the printing system

The printing process consists of six main steps. Charging of a photo-conductor, exposing the photo-conductor drum or belt or image exposure, the development of the latent image, transferring the image from the photo-conductor to a sheet of paper or any other printing media, fusing the developed image to the printing media and finally cleaning any residual toner from the photo-conducting drum or belt in preparation for the next print [48]-[50]. These steps are illustrated in Figure 5.1.

5.3.1 The corona charging

Prior to the image exposure, an electrical field is established within the photo-conductor film. A charge distribution on the photo-conductor surface is generated by absorption of ionized gas molecules that arise from an electrical corona device. A corona discharge device usually consists of several thin wires, typically 3-8 corona wires, which are strung within a metal enclosure. A high voltage is applied to these wires, typically 5-10 kV, which generates an electric field around the wires. This electric field ionizes the air molecules and results in charged ions. The charged ions are driven onto the photo-conductor surface. The uniformity of the charge distribution on the surface of the photo-conductor is important to avoid non-uniformities in the developed image.

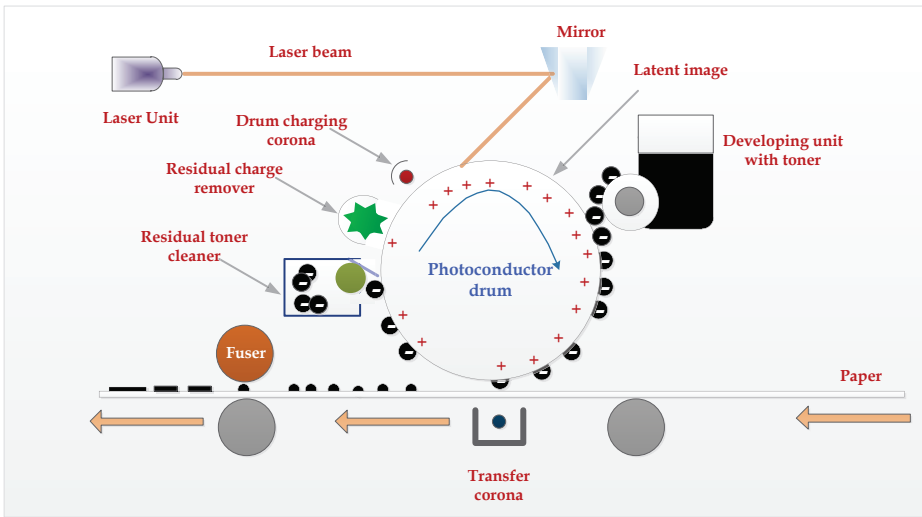


Figure 5.1: Laser printer schematic diagram.

The emission uniformity is good for a positive potential but very poor for the negative corona potential. The scorotron was invented to deal with the problem of charging a photo-conductor with uniform negative potential. The scorotron consists of a series of corona wires with a screen of larger diameter, $250 \mu\text{m}$, wires with a lower voltage level, $500 - 1000 \text{ V}$, is applied between the corona wires and the photo-conductor surface.

5.3.2 The photo-conductor drum

One of the main components in the printing process is the photo-conductor, it is also known as the toner transfer belt (TTF). Photo-conductors are conductors in the light and insulators in the dark. These properties are essential to the process. At this point, the photo-conductor has a uniform surface potential associated with it. The next step is to expose the image of a document onto the surface of the photo-conductor. By using lenses and mirrors, a latent image is exposed and forms the charged photo-conductor. The image is converted into a visible one by depositing charged toner particles on the photo-conductor. The imaged areas of the photo-conductor remain unexposed and charged, while the areas that receive light become neutralized. In a neutralized area the charge is drained away from the surface of the photo-conductor to the metalized ground. What remains is the electrostatic latent image. Earlier photo-receptors consisted of selenium coated on a metalized drum. Nowadays, they are coated on aluminized Mylar and are made into smoothly continuous belts. Once an electrostatic latent image is formed on the photo-conductor, it is ready for development.

5.3.3 Electrostatic image development

The image in static electricity needs to be developed. The developer disposes small particles of toner, colored plastic dust, onto the statically-charged surface of the photo-conductor drum. The developer is often a hopper filled with toner and mixed with iron fillings. The developer roller faces the drum, with just a fractional separation. The developer roller rotates carrying a thin layer of filings and toner out towards the drum. The developer roller has an electrical charge equal to the charged area of the drum, so toner will only stick where the light has discharged the photo-conductor. Moreover, it contains a magnet which causes the filings coated in toner to stand on end as they pass the drum. Nowadays, resin rollers and sheets are used to create a finer developer coating. The developer brushes the drum gently with plastic dust which is repelled from the charged area and sticks to those areas with no charge.

5.3.4 Image transfer

The developed image is now ready to be transferred to the printing media. A transfer corona unit is used to transfer the developed image to the printing media. The transfer corona unit generates an attractive electric field. If a machine is using positive toner then it must use a negative transfer corona unit and vice versa. Without the attractive electric field, the toner will remain on the photo-conductor. The toner can now be directly transferred to metal sheets, insulating films, or paper. Since the photo-conductor drum rotates with the same speed as the printing media, the image is transferred with relatively high precision. The printing media now carries the developed image and moves to the fuser.

5.3.5 Fusing the image

After the image has been transferred to the paper it needs to be made permanent. Prior to this step the formed toner-image is somewhat loosely bound to the paper surface and can easily be disturbed or rubbed off. Various methods of fusing include hot roll pressure fusing, cold pressure fusing, radiant fusing, flash fusing, and vapor fusing. Most of the high-speed fusing is done using hot roll pressure fusers. This technique employs steel rollers, which are loaded against each other by compression spring. These rollers are usually heated using a tungsten quartz lamp. The printing media is then passed between the two rollers and, therefore, the image is fused on the printing media. The typical fusing temperature is around 130 °C.

5.3.6 Residual toner cleaning

The last step is to clean the photo-conductor drum from the toner that is not transferred to the printing media. Some of the toner particles remain on the photo-conductor sur-

face. The remaining particles are usually smaller than the particles that are transferred to the printing media. Since the larger particles tend to shield the smaller ones on transfer. These particles have to be removed from the photo-conductor surface, since otherwise they might interfere with the corona charging and the image exposure. Scraper blades or rotating brushes are utilized to clean the photo-conductor drum. An erase lamp and a corona unit are also involved in the cleaning process. The erase lamp removes the latent electrostatic image and the corona device neutralizes the surface charges.

5.4 Printing system heat flow

In this thesis, we focus on the fusing part and the heat flow in the printing system. The heat flow is very relevant in a printer [51]-[52], since it is linked to the fundamental goal of the printing system, namely, to achieve high-quality prints and high throughput. The printing quality is highly affected by the fuse temperature. Therefore, it is required to monitor and accurately control the fuse temperature. If the fuse temperature is too low, the toner will not properly penetrate the paper and a toner layer will be formed on top of the paper, which can be easily removed by bending and scratching. On the other hand, a too high fuse temperature will cause the toner to melt and stick to any other surfaces. Moreover, the amount of heat lost during printing affects the printing speed and, consequently, the throughput. The average energy consumption of the printer over a working day is part of the running costs for a printer. Most of the power consumed by a printer is used to maintain heat flows and certain temperature levels. Moreover, the power consumption is evidently limited by the available power. These issues illustrate the importance of proper heat control for a printing system.

5.4.1 Heat flow model

The heat storage behavior can be modeled as the storage of electrical charge [53]. For example, a capacitor stores electrical charge, resulting in an electrical potential over the capacitor. In this section, we utilize the electrical analogy to model the heat flow in the printing system. As such, the elements that can store heat are modeled as the capacitor, the transportation of heat is modeled as an electrical charge, which is transported through resistors. The heat resistors are not heat storage elements. In the printing system, heat is transported in three different ways, namely, conduction, convection, and radiation. The heat is transported by conduction through the mechanical components. Heat flow is convected via the air flow, and radiated by hot surfaces. In addition, heat is transported via the movement of objects in the printer, such as the printing media or the TTF belt.

Heat conduction and convection are modeled as linear thermal resistances, where the resistance might depend on system parameters such as rotational speed. Heat radiation

is modeled as a non-linear resistance. Heat, which is inserted into the printer, is represented as electrical power. The printing system, which we study in this thesis, has two heaters that generate heat from electrical energy. The preheater, P_{pre} , is responsible for warming up the paper to a desired temperature before fusing. The TTF rollers are usually heated using a tungsten quartz lamp P_{TTF} .

The following assumptions are made to derive the heat flow model (5.1)

- The printer is modeled as lumped. Only the most interesting temperatures are explicitly included.
- The sheets are not modeled individually but as a continuous paper mass flow, when they interact with the TTF.
- The interaction between areas of different temperatures are modeled using heat resistors between the lumped capacitances.
- The printing media (the paper) extracts heat from the preheater and exchanges heat with the TTF.

As mentioned, controlling the fuse temperature is the key to achieve high printing quality. The fuse temperature T_{fuse} is determined by the temperature of the paper sheets and the temperature of the TTF belt at the fuse pinch. The fuse temperature cannot be measured, therefore, the preheating temperature T_{pre} and the TTF temperature T_{TTF} are used as a good estimation of the fuse temperature. The dynamics of the preheating and TTF systems are given by the following lumped model

$$\begin{aligned}
 \dot{T}_{pre} &= \frac{1}{C_{pre}} \left(P_{pre} - m_{pap} v c_{pap} (T_{pap} - T_{init}) - \frac{T_{pre} - T_{env}}{R_{env}} \right), \\
 \dot{T}_{TTF} &= \frac{1}{C_{TTF}} \left(N_{TTF} P_{TTF} - \frac{T_{TTF} - T_{env}}{R_{env}} - \frac{T_{TTF} - T_{pap}}{R_{pap}} \right. \\
 &\quad \left. - \frac{T_{TTF} - T_{slow}}{R_{slow}} - \frac{T_{TTF} - T_{roller}}{R_{roller}} \right), \\
 \dot{T}_{roller} &= \frac{1}{C_{roller}} \left(\frac{T_{TTF} - T_{roller}}{R_{roller}} \right), \\
 \dot{T}_{slow} &= \frac{1}{C_{slow}} \left(\frac{T_{TTF} - T_{slow}}{R_{slow}} \right),
 \end{aligned} \tag{5.1}$$

with

$$T_{pap} = T_{init} + (T_{pre} - T_{init}) \left(1 - e^{-\frac{\lambda L_{pre}}{m_{pap} v}} \right),$$

where T [K] denotes the temperature of different objects, C [J/K] represents the thermal capacity, R [K/w] is the thermal resistance, P_{pre} [w] and P_{TTF} [w] denote the input

power to the preheater and the TTF heater, respectively, N_{TTF} [-] denotes the TTF heater thermal efficiency, m_{pap} [kg] is the paper mass, v [m/s] is the belt speed, T_{pap} [K] is the average temperature of the paper, and L_{pre} [m] represents the length of the preheater. T_{roller} [K] and T_{slow} [K] represent the temperature of the various rollers that are in contact with the TTF. T_{env} [K] denotes the environment temperature to which heat is leaked.

Due to physical and practice considerations, the fusing temperature cannot be measured directly. Therefore, the fuse temperature is estimated as follows,

$$T_{fuse} = T_{TTF} + \frac{\alpha P_{TTF}}{\sqrt{v}}, \quad (5.2)$$

where α is an estimator parameter and v is belt speed. The model (5.1) is connected to a higher level controller, which determines the amount of the available power and printer speed. Several parameters of the model (5.1) are time varying, since these parameters depend on the different printing jobs and the rotation speed, while other parameters are unknown.

5.5 Control challenges for the printing system

In the printing system there are several challenging issues, such as uncertainty arising from the printer itself, the printing media, and external disturbances. Most of the printing process variation results from changes in various element properties, e.g. toner, carrier, photoreceptor, etc.

- Slowly varying property changes are typically in response to external disturbances and/or wear. For instance, the adhesion of the toner particles might change as a function of the humidity level in the developer, which, in turn, impacts the ability of the toner to develop and transfer. Gradual wear alters photoreceptor properties resulting in changes to the behavior of development and transfer.
- Large and fast varying properties are mainly related to the printing speed and different printing jobs (paper mass, humidity, size, media, etc.). Consider, for example, a customer print job that involves multiple media types such as heavy-weight cover stock and light-weight coated paper. These media types have considerable different transfer and fusing performance characteristics and thus different parameters in the model (5.1).
- The primary external disturbance that affects the performance of a printing system is the environment. Environment refers to the ambient operating temperature, relative humidity, and altitude of the printer, which can all vary significantly depending on whether the printer is operating in the summer or in winter. In particular, the ambient environment affects the electrical properties of developer and media materials, which, in turn, influence the development and transfer processes.

These issues have a negative effect on the stability and performance of the printing system. For future applications, laser printers have to produce higher quality prints, be more reliable under a broader range of conditions, and at a reduced per-print cost. As a result, such printers should be adaptable with respect to variations in media, and the environmental variations. These challenges give rise to the research questions explained in chapter 1. Adaptive control strategies will play an increasingly important role to answer these questions. In the next two chapters, we discuss two different control strategies that tackle these research questions. In chapter 6, we propose a novel Model Reference Adaptive Controller (MRAC) scheme to cope with the large parameter variations and disturbances. We propose two methods to improve the adaptation speed of the MRAC to deal with fast parameter variations, namely, using nonlinear adaptation gain and multiple adaptation gain. We propose an adaptation gain as a function of the tracking error. Thanks to this choice, a faster controller parameter adaptation is achieved when the tracking error is large and thus a faster error convergence is obtained. A new Lyapunov function is introduced to investigate the stability of both state and output feedback MRAC.

In the second approach, unlike the standard MRAC, which uses a single adaptation gain, multiple adaptation gains are proposed. The adaptive control problem formulation involves recasting the error dynamics, which comprise of the tracking error and error of the controller parameters, into a Takagi-Sugeno model. A sufficient condition is derived to ensure the asymptotic stability of the system for both state and output feedback cases. The adaptive control problem is formulated as a minimization of the \mathcal{L}_2 gain. The optimal adaptation gains are obtained by solving a linear matrix inequality problem.

Both approaches show a faster error convergence compared to a constant adaptation gain. Moreover, the implementation of the proposed approaches elucidates that the performance of the printing system can be considerably improved in the presence of large parameter variations compared to the present industrial controller.

In chapter 7, the robust control problem of a laser printing system, using an \mathcal{L}_2 observer-based output feedback controller, is analyzed. The nonlinear printing system is approximated by a Takagi-Sugeno (T-S) model at different operating conditions. A robust control technique is proposed to cope with the effect of the approximation error between the nonlinear model of the printing system and the approximated T-S model. A sufficient condition is derived to ensure robust stability of an \mathcal{L}_2 observer-based output feedback controller with guaranteed disturbance attenuation level. A parameterized Lyapunov function is employed in our approach. A transformation formulates the problem in terms of a linear matrix inequality for which efficient optimization solvers are used to test feasibility. This approach is an optimal gain scheduling technique, where the print jobs are used to choose the proper controller. The implementation of this approach yields considerable improvements of the printing system performance compared with the preset industrial controller.

Chapter 6

Improved Convergence of MRAC Designs for Laser Printer

This chapter deals with the improved design of model reference adaptive controllers (MRAC). Two different approaches are proposed to improve the performance of MRAC. First, we introduce a nonlinear adaptation gain. Uniform asymptotic stability of the system is demonstrated for both state and output feedback cases. In the second approach, multiple adaptation gains are employed. The formulation involves recasting the error dynamics, which comprise of the tracking error and error of the controller parameters, into a Takagi-Sugeno model. A sufficient condition is derived to ensure the asymptotic stability of the system for both state and output feedback cases. The adaptive control problem is formulated as a minimization of the \mathcal{L}_2 gain. The optimal adaptation gains are obtained by solving a linear matrix inequality problem. A numerical example compares the proposed approaches with the standard MRAC. Moreover, the proposed approaches are applied to control a model of printing system to improve the printing quality where large parameter variations, owing to different print jobs, and disturbances are present.

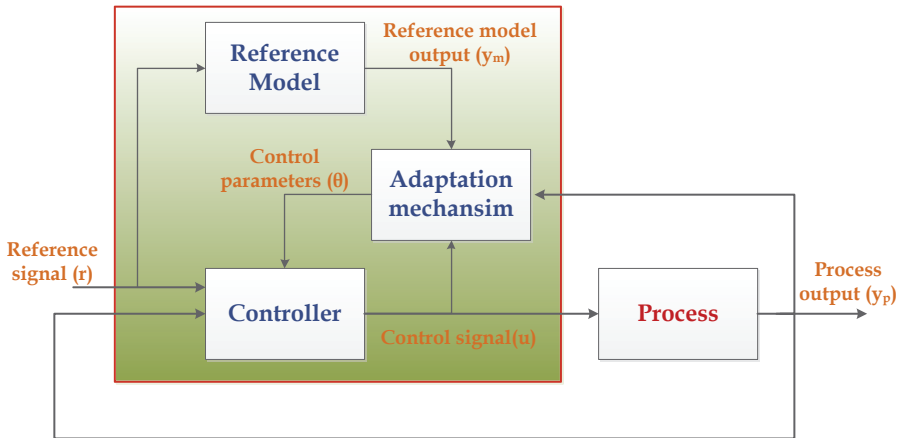


Figure 6.1: Main structure of MRAC.

6.1 Introduction

An adaptive controller modifies a control law used by a controller to cope with the time-varying or uncertain parameters of the system being controlled [54]- [55]. MRAC is one of the approaches to adaptive control. MRAC was first introduced by Whitacker in 1958. Over the past several years, various model-reference adaptive control (MRAC) methods have been investigated. The majority of MRAC methods may be classified as direct, indirect, or a combination thereof. Indirect adaptive control methods are based on identification of unknown plant parameters and certainty-equivalence control schemes derived from the parameter estimates, which are assumed to be their true values. Parameter identification techniques such as recursive least-squares and neural networks have been used in indirect adaptive control methods. On the other hand, direct adaptive control methods directly adjust control parameters to account for system uncertainties without identifying unknown plant parameters explicitly. In this chapter we focus on direct adaptive control.

The basic structure of a direct MRAC scheme is shown in Figure 6.1. MRAC attempts to reduce the tracking error $e_1 = y_p - y_m$ between the plant output y_p and the output of the reference model y_m . A stable reference model is designed to achieve a desired control performance. The closed-loop system consists of an ordinary control configuration with a feedback control law that contains the plant and a controller $C(\theta)$ and an adjustment mechanism that optimally adjusts the controller parameters $\theta(t)$ on-line to force the controlled plant to follow the reference-model output. The design procedure involves the use of a wide class of adaptive laws that include least-squares, gradient and SPR-Lyapunov design approaches [56]-[57].

Adaptive control has been successfully implemented in several applications. However, the high-gain control for fast adaptation is an issue. In some applications, fast adaptation is required to improve tracking performance when a system is subject to large uncertainties. In this case, a large adaptation gain must be used to reduce the tracking error rapidly. However, there typically exists a balance between stability and speed of adaptation. A fast adaptation gain results in high-frequency oscillations, which can excite unmodeled dynamics that could adversely affect the stability of an MRAC system. On the other hand, small adaptation gains will result in an unacceptable slow response. Several methods are discussed in [54] to choose the adaptation gain. In [58], two algorithms are proposed to tune the adaptation gain for a gradient based parameter update law used for a class of nonlinear discrete-time systems. These algorithms require the knowledge of the system model as well as the system states. Moreover, these methods require a considerable on-line computation time. In [60] an \mathcal{L}_1 adaptive control is addressed, where a low-pass filter is used to prevent the high frequency oscillation that might occur due to fast adaptation. In this case, the reference output is no longer preserved and it has to be reconstructed using a predictor model. A hybrid direct-indirect adaptive control is investigated in [62]. An indirect adaptive law based on a recursive least-squares parameter estimation identifies the parameters of a nominal controller to reduce the modeling error, and the remaining tracking error signal is then handled by a direct adaptive law with a smaller learning rate.

In this chapter, we address two different methods to improve the convergence of the MRAC, namely, using a nonlinear varying adaptation gain and using multiple adaptation gains with a new adaptation law.

In [62], we have proposed a nonlinear varying adaptation gain. The design does not require any knowledge of the parameters of the system. To improve the system performance, the adaptation gain should be chosen as a function of the controller parameter error. However, the optimal controller parameters depend on the process parameters, which are usually unknown. The error between the outputs of the process and of the reference model gives also a good indication of the controller parameter error. Hence, we propose an adaptation gain as a function of the output error instead of controller parameter error. A new Lyapunov function is introduced to investigate the stability of both state and output feedback MRAC systems. A faster convergence of MRAC is achieved using the nonlinear adaptation gain.

A further performance improvement of MRAC is obtained in [63], where a novel adaptation law is introduced for both state and output feedback. Unlike the standard MRAC, which uses a single constant adaptation gain, multiple adaptation gains are employed in this approach. The error dynamics, which are composed of the output tracking error and the controller parameter estimation error, are first represented by a Takagi-Sugeno

(T-S) model. The T-S model is considered as an exponentially stable system perturbed by an external disturbance. Therefore, the adaptive control problem is formulated as minimizing the \mathcal{L}_2 gain. By this formulation, the optimal adaptation gains are obtained by solving a linear matrix inequality (LMI) problem.

The chapter is organized as follows, First we present the standard MRAC. Then we introduce the modified state and output feedback MRAC design using nonlinear varying adaptation gain. Afterwards, the new adaptation law with multiple adaptation gain is addressed. The proposed approaches are compared with the standard MRAC using a numerical example. Finally we illustrate the application of the proposed approaches for a printing system.

6.2 Preliminary

In this section, we review the basics of the MRAC approach for SISO systems. Consider a linear slowly time-varying system given by

$$\begin{aligned}\dot{x}_p(t) &= A_p(t)x_p(t) + B_p(t)u(t), \\ y_p(t) &= C_p(t)x_p(t),\end{aligned}\tag{6.1}$$

where $x_p(t) \in \mathbb{R}^n$ is the state vector of the plant, $y_p(t) \in \mathbb{R}$ is the plant output, $A_p(t) \in \mathbb{R}^{n \times n}$, $B_p(t) \in \mathbb{R}^n$ and $C_p^\top(t) \in \mathbb{R}^n$ are the state space matrices, which are assumed to be time varying, and $u(t) \in \mathbb{R}$ denotes the plant input.

The stable reference model is given by

$$\begin{aligned}\dot{x}_m(t) &= A_m x_m(t) + B_m r(t), \\ y_m(t) &= C_m x_m(t),\end{aligned}\tag{6.2}$$

where $r(t) \in \mathbb{R}$ is a reference input signal $x_m(t) \in \mathbb{R}^{m_r}$ is the state vector of the reference model, $y_m(t) \in \mathbb{R}$ is the reference output, $A_m \in \mathbb{R}^{m_r \times m_r}$, $B_m \in \mathbb{R}^{m_r}$ and $C_m^\top \in \mathbb{R}^{m_r}$ are the state space matrices of the reference system. The reference model is chosen to represent a desired performance of the closed-loop system. Here, both the plant model (6.1) and the reference model (6.2) are represented in the controller

canonical form [64]. That is,

$$A_p(t) = \begin{bmatrix} 0 & 1 & 0 & 0 \\ \vdots & 0 & \ddots & 0 \\ 0 & \cdots & 0 & 1 \\ a_{p1}(t) & a_{p2}(t) & \cdots & a_{pn} \end{bmatrix}, \quad B_p(t) = \begin{bmatrix} 0 \\ \vdots \\ \vdots \\ b_p(t) \end{bmatrix}$$

Similarly,

$$A_m = \begin{bmatrix} 0 & 1 & 0 & 0 \\ \vdots & 0 & \ddots & 0 \\ 0 & \cdots & 0 & 1 \\ a_{m1} & a_{m2} & \cdots & a_{mn} \end{bmatrix}, \quad B_m = \begin{bmatrix} 0 \\ \vdots \\ \vdots \\ b_m \end{bmatrix}$$

6.2.1 State feedback MRAC

Consider the state feedback control law

$$u(t) = K_{ff}(t)r(t) + K_{fb}^\top(t)x_p(t), \quad (6.4)$$

which is written in a compact form as

$$u(t) = \theta^\top(t)w(t), \quad (6.5)$$

where $\theta(t) = \text{col}(K_{ff}(t), K_{fb}^\top(t)) \in \mathbb{R}^{1+n}$ denotes the controller parameter vector and $w(t) = \text{col}(r(t), x_p(t)) \in \mathbb{R}^{n+1}$ is the regressor vector.

The time-varying closed-loop system is expressed as

$$\begin{aligned} \dot{x}_p(t) &= (A_p + B_p K_{fb}^\top) x_p(t) + B_p K_{ff} r(t), \\ &= A_{cl}(\theta(t)) x_p(t) + B_{cl}(\theta(t)) r(t). \end{aligned} \quad (6.6)$$

We will assume the existence of an *idealized controller*

$$u_m(t) = K_{ff}^m(t)r(t) + K_{fb}^m(t)x_p(t), \quad (6.7)$$

which is parameterized by the vector

$$\theta_m(t) = \text{col}(K_{ff}^m(t), K_{fb}^m(t)) \in \mathbb{R}^{1+n} \quad t \geq 0,$$

that consists of ideal controller parameters. Here, ideal means that the reference model (6.2) coincides with the closed-loop system defined by (6.6) when controlled by (6.5). This is known as the perfect model following condition, more precisely, we assume that

$$A_{cl}(\theta_m(t)) = A_m(t), \text{ for all } t \geq 0,$$

$$B_{cl}(\theta_m(t)) = B_m(t), \text{ for all } t \geq 0.$$

This condition is satisfied by choosing the controller parameters that implies

$$A_p - A_m = -B_p K_{fb}^\top, \quad B_m = B_p K_{ff}.$$

Based on the system representation (6.3), the idealized controller parameter is given as

$$\begin{aligned} K_{ff}^m(t) &= \frac{b_m}{b_p}, \\ K_{fb}^{m\top} &= -\frac{1}{b_p} \Delta A, \end{aligned} \tag{6.8}$$

where

$$\Delta A := [a_{p1} - a_{m1} \quad \cdots \quad a_{pn} - a_{mn}].$$

Define the state tracking error be

$$e(t) = x_p(t) - x_m(t). \tag{6.9}$$

The dynamics of the tracking error are described by

$$\begin{aligned} \dot{e}(t) &= A_m e(t) + (A_{cl}(\theta(t)) - A_m)x_p(t) + (B_{cl}(\theta(t)) - B_m)r(t), \\ &= A_m e(t) + [B_{cl}(\theta(t)) - B_m \quad A_{cl}(\theta(t)) - A_m] \begin{bmatrix} r(t) \\ x_p(t) \end{bmatrix}, \\ &= A_m e(t) + B_I \tilde{\theta}^\top(t) w(t). \end{aligned} \tag{6.10}$$

where $B_I = [0 \quad \cdots \quad 0 \quad 1]^\top \in \mathbb{R}^n$ and

$$\tilde{\theta}^\top(t) := B_I^\top B_p \theta^\top(t) + [-B_I^\top B_m \quad B_I^\top (A_p - A_m)]$$

defines the error of the parameters of the controlled system and of the model, which can be written in terms of the idealized controller as

$$\tilde{\theta}^\top(t) := B_I^\top B_p (\theta^\top(t) - \theta_m^\top(t)).$$

Lemma 6.2.1. *For time invariant models (6.1) and (6.2), the closed-loop system (6.6) is asymptotically stable ($e \rightarrow 0$) using the control law (6.5) and the update law*

$$\dot{\tilde{\theta}} = \dot{\theta} = -\Gamma w B_I^\top P e, \tag{6.11}$$

where $\Gamma \succ 0$ is the adaptation gain and $P \succ 0$ a positive definite matrix, which satisfies $A_m^\top P + P A_m \prec 0$.

Proof. Consider the Lyapunov function

$$V(e, \tilde{\theta}) = e^\top P e + \tilde{\theta}^\top \Gamma^{-1} \tilde{\theta}, \quad (6.12)$$

The time derivative of (6.12) along the trajectory of (6.10) is given as

$$\dot{V} = e^\top (A_m^\top P + P A_m) e + 2(\tilde{\theta}^\top w) B_I^\top P e + 2\tilde{\theta}^\top \Gamma^{-1} \dot{\tilde{\theta}}, \quad (6.13)$$

selecting the adaptation law

$$\dot{\tilde{\theta}} = \dot{\theta} = -\Gamma w B_I^\top P e, \quad (6.14)$$

we obtain

$$\frac{d}{dt} V(e, \tilde{\theta}) = -e^\top (A_m^\top P + P A_m) e < 0.$$

That completes the proof. \square

Adaptive control systems may exhibit unbounded parameter drift even for bounded disturbances. The method of σ -modification [65] is proposed to avoid the parameter drift. Towards this end, the update law (6.11) is modified to

$$\dot{\tilde{\theta}} = \dot{\theta} = -\Gamma w B_I^\top P e - \sigma \tilde{\theta} \quad (6.15)$$

where $\Gamma \succ 0$, $P \succ 0$ satisfy $A_m^\top P + P A_m \prec 0$.

6.2.2 Output feedback MRAC

In practice the plant states are not measurable and only the plant output is measurable. In such a case, a state observer, such as a Kalman-filter, is difficult to use since the plant parameters are unknown. Several techniques are proposed for the design of the output feedback MRAC [59], [72]. The *augmented error method* is accepted in the literature as the standard approach for MRAC with output feedback. The augmented error method is a combination of a primary controller and a set of adaptive laws. The structure of the primary controller is shown in Fig. 6.2. The primary controller includes two auxiliary signal generators (ASGs) to produce vectors $z_1(t) \in \mathbb{R}^{n-1}$ and $z_2(t) \in \mathbb{R}^{n-1}$, which are filtered signals of the plant input $u(t)$ and the plant output $y_p(t)$, respectively. For more details about how to design the ASGs, the reader is referred to [59].

Consider the reference model

$$\begin{aligned} \dot{x}_m(t) &= A_m x_m(t) + B_m r(t), \\ y_m(t) &= C_m x_m(t), \end{aligned} \quad (6.16)$$

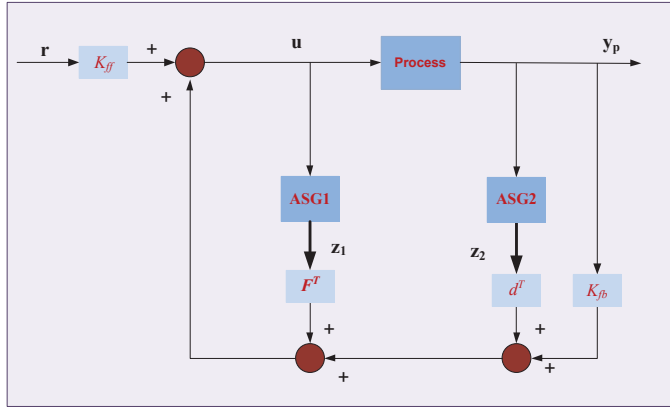


Figure 6.2: Main structure of the primary controller of the augmented error method.

The primary controller is defined as

$$u(t) := K_{ff}r(t) + F^T z_1 + K_{fb}y_p + d^T z_2,$$

which is written in the compact form

$$u(t) = \theta^T(t)w(t) \quad (6.17)$$

with

$$\theta^T = \begin{bmatrix} K_{ff} & F^T & K_{fb} & d^T \end{bmatrix}$$

are the controller parameter and

$$w(t)^T = \begin{bmatrix} r(t) & z_1^T(t) & y_p(t) & z_2^T(t) \end{bmatrix}.$$

The adaptive laws are derived using Lyapunov's second method. However, it is not a straightforward to derive the error equations as in the state feedback case. This is because the ASGs introduce extra states in the closed-loop system. In this case, the closed-loop system has a higher order than the reference model. It is shown in [72] that the output error $e_1 = y_p - y_m$ can be written as

$$e_1 = G_m \tilde{\theta}^T w$$

where $G_m = C_m(sI - A_m)^{-1}B_m$ represents the transfer function of the reference model (6.16) and $\tilde{\theta} = \theta - \theta_m$.

Therefore, the error equation is expressed as

$$\dot{e}(t) = A_m e(t) + B_m \tilde{\theta}^T w, \quad (6.18)$$

with $e(t) = \begin{bmatrix} e_1 & \dot{e}_1 & \cdots & e_1^{(n-1)} \end{bmatrix}^\top$.

Assume that the reference model (6.16) is strictly positive real (SPR) and it is represented in the controller canonical form. Then, there exist positive definite matrices $P = P^\top \succ 0$ and $Q \succ 0$ such that the following conditions hold,

$$\begin{aligned} A_m^\top P + P A_m &= -Q \\ P B_m &= C_m^\top \end{aligned} \quad (6.19)$$

Consider the quadratic Lyapunov function

$$V(e, \tilde{\theta}) = e^\top P e + \tilde{\theta}^\top \Gamma^{-1} \tilde{\theta}, \quad (6.20)$$

with $\Gamma = \Gamma^\top \succ 0$ denotes the adaptation gain. The time derivative of (6.20) along the trajectory of (6.18) is given as

$$\frac{d}{dt} V(e, \tilde{\theta}) = e^\top (A_m^\top P + P A_m) e + 2(\tilde{\theta}^\top w) B_m^\top P e + 2\tilde{\theta}^\top \Gamma^{-1} \dot{\tilde{\theta}}, \quad (6.21)$$

applying the SPR properties (6.19) yield

$$\frac{d}{dt} V(e, \tilde{\theta}) = -e^\top Q e + 2(\tilde{\theta}^\top w) e_1 + 2\tilde{\theta}^\top \Gamma^{-1} \dot{\tilde{\theta}}. \quad (6.22)$$

Selecting the adaptation law

$$\dot{\tilde{\theta}} = \dot{\theta} = -\Gamma w e_1, \quad (6.23)$$

we obtain

$$\frac{d}{dt} V(e, \tilde{\theta}) = -e^\top Q e \leq 0.$$

Note that the derivative of V with respect to time is thus negative semi-definite. This implies that $V(t) \leq V(0)$ and, therefore, e and $\tilde{\theta}$ are bounded. This implies that the controller parameters θ and the system output y_p will be bounded. It follows that the second derivative of V with respect to time \ddot{V} will be bounded, and hence $\frac{d}{dt} V(e, \tilde{\theta})$ is uniformly continuous. This implies that the error e will converge to zero. However, the controller parameters θ will not necessarily converge to their correct values. This result shows that the controller parameters will be bounded. To guarantee the convergence of parameters, it is necessary to impose conditions, such as persistence of excitation and uniform observability, on the reference signal and on the system.

6.3 Nonlinear time varying adaptation gain

The adaptation gain Γ determines the rate at which the controller parameter will converge to steady state values. Moreover, the adaptation gain influences the performance of the system. Hence, the adaptation gain should be properly chosen. A too high adaptation gain may lead to badly damped behavior, while a too low adaptation gain will lead to an unacceptable slow response. In this section, we propose a nonlinear time varying adaptation gain, which does not require any knowledge of the parameters of the system. To improve the system performance, the adaptation gain could be chosen as a function of the controller parameters error. However, the idealized controller parameters depend on the process parameters, which are usually unknown. The error between the outputs of the process and of the reference model gives also a good indication about the controller parameters error. Hence, we propose an adaptation gain as a function of the output error instead of controller parameters error. A new Lyapunov function is introduced to investigate the stability of both state and output feedback MRAC systems.

6.3.1 Modified state feedback

In this subsection, a new MRAC state feedback design is introduced based on a nonlinear adaptation gain. The adaptation gain Γ is chosen as a function of the error e such that if the error is large, the adaptation gain Γ will be large. This implies that the controller will adapt its parameters faster and thus a faster convergence of the error is achieved. Let the adaptation gain be

$$\Gamma = \gamma_0 + \gamma_1 e^\top P e, \quad \gamma_0 > 0, \quad \gamma_1 > 0, \quad P \succ 0, \quad \text{therefore} \quad \Gamma > 0. \quad (6.24)$$

Theorem 6.3.1. *Using the state feedback control law (6.5), the adaptation law (6.11), and the nonlinear adaptation gain (6.24), the closed-loop system is asymptotically stable.*

Proof. Consider the candidate Lyapunov function

$$V(e, \tilde{\theta}) = \left(\frac{\gamma_1}{2} e^\top P e + \gamma_0\right) e^\top P e + \tilde{\theta}^\top \tilde{\theta}, \quad (6.25)$$

where $\gamma_0 \in \mathbb{R}_+$, $\gamma_1 \in \mathbb{R}_+$, and $P \succ 0$ is a positive definite symmetric matrix. The time derivative of (6.25) along the trajectory of (6.10)

$$\begin{aligned} \frac{d}{dt} V(e, \tilde{\theta}) &= \left(\frac{\gamma_1}{2} e^\top P e + \gamma_0\right) (\dot{e}^\top P e + e^\top P \dot{e}) + \frac{\gamma_1}{2} (\dot{e}^\top P e + e^\top P \dot{e}) e^\top P e \\ &\quad + 2\tilde{\theta}^\top \dot{\tilde{\theta}}, \end{aligned} \quad (6.26)$$

$$\frac{d}{dt} V(e, \tilde{\theta}) = (\gamma_1 e^\top P e + \gamma_0) (\dot{e}^\top P e + e^\top P \dot{e}) + 2\tilde{\theta}^\top \dot{\tilde{\theta}}. \quad (6.27)$$

Using the error dynamics (6.10) and the adaptation gain (6.24), the time derivative of V yields

$$\frac{d}{dt}V(e, \tilde{\theta}) = \Gamma(e^\top(A_m^\top P + PA_m)e + 2(\tilde{\theta}^\top w)B_I^\top Pe) + 2\tilde{\theta}^\top \dot{\tilde{\theta}}. \quad (6.28)$$

With the adaptation gain law

$$\dot{\tilde{\theta}} = \dot{\theta} = -\Gamma w B_I^\top Pe$$

as given in (6.24) we infer that

$$\frac{d}{dt}V(e, \tilde{\theta}) = \Gamma e^\top(A_m^\top P + PA_m)e < 0 \quad \text{if } e^\top e \neq 0. \quad (6.29)$$

Therefore, V is a Lyapunov function for the system. \square

Note that γ_0 and γ_1 are design parameters. The nonlinear adaptation gain (6.24) is more generic than the standard MRAC with a constant adaptation gain ($\gamma_1 = 0$).

6.3.2 Modified output feedback

In practice, limited state information may be available, and only the process output may be measurable. In this subsection, a nonlinear adaptation gain is considered to improve the system behavior of MRAC using output feedback. We derive an MRAC for adjusting the parameters of a controller based on output feedback. It is assumed that the dynamics are linear and that the control problem is formulated as a model matching.

Theorem 6.3.2. *Using the control output law*

$$u(t) = K_{ff}r(t) + F^\top z_1 + K_{fb}y_p + d^\top z_2,$$

and the update rule (6.23) with the time varying adaptation gain (6.24), the closed-loop system is asymptotically stable.

Proof. Consider the time varying adaptation gain (6.24) and the candidate Lyapunov function (6.25), the time derivative of V along the trajectories of the error dynamics (6.18) is

$$\begin{aligned} \frac{d}{dt}V(e, \tilde{\theta}) &= \left(\frac{\gamma_1}{2}e^\top Pe + \gamma_0\right)(\dot{e}^\top Pe + e^\top P\dot{e}) + \frac{\gamma_1}{2}(\dot{e}^\top Pe + e^\top P\dot{e})e^\top Pe \\ &\quad + 2\tilde{\theta}^\top \dot{\tilde{\theta}}, \end{aligned} \quad (6.30)$$

$$= (\gamma_1 e^\top Pe + \gamma_0)(\dot{e}^\top Pe + e^\top P\dot{e}) + 2\tilde{\theta}^\top \dot{\tilde{\theta}}. \quad (6.31)$$

With (6.10) and the adaptation gain (6.24), this gives

$$\frac{d}{dt}V(e, \tilde{\theta}) = \Gamma(e^\top (A_m^\top P + PA_m)e + 2(\tilde{\theta}^\top w)B_m^\top Pe) + 2\tilde{\theta}^\top \dot{\tilde{\theta}}, \quad (6.32)$$

Applying the SPR property (6.19) yields

$$\frac{d}{dt}V(e, \tilde{\theta}) = \Gamma(e^\top (-Q)e + 2\tilde{\theta}^\top we_1) + 2\tilde{\theta}^\top \dot{\tilde{\theta}}. \quad (6.33)$$

Let the adaptation law be

$$\dot{\tilde{\theta}} = \dot{\theta} = -\Gamma we_1,$$

we obtain

$$\frac{d}{dt}V(e, \tilde{\theta}) = \Gamma e^\top (-Q)e < 0$$

if $e^\top e \neq 0$ and Γ as defined in (6.24). We conclude that the closed-loop system is asymptotically stable. \square

Using the adaptation gain (6.24) leads to a faster error convergence for both state and output feedback compared with a constant adaptation gain. However, this adaptation gain contains two design parameters, γ_0 and γ_1 . By trial and error, high performance can be achieved. There is no systematic algorithm to obtain these design parameters optimally. In the next section, we propose a novel adaptation mechanism with multiple adaptation gains, which are designed based on an optimization criterion.

6.4 Multiple-adaptation gain MRAC design

To improve the adaptation transients the use of multiple adaptation gains offers a very appealing solution. The key idea of this approach is to select in real time the best adaptation gain from an a priori designed set of adaptation gains. The adaptation gain is selected based on the operating point of the system states. In this approach, a Takagi-Sugeno (T-S) model is employed to represent the error dynamics, which are composed of the output tracking error and the controller parameter estimation error.

The Takagi-Sugeno (T-S) model has been widely used in various applications since it can efficiently model and control complex nonlinear systems. A T-S model, which was introduced in [66], is composed of the weighted sum of local linear models. A T-S model approximates a nonlinear system and the weights in the T-S model depend on the operating point of the nonlinear system. According to the universal approximation theorem [67], a T-S model can approximate a nonlinear system arbitrarily well. Recently,

T-S model-based controllers have been applied to stabilize nonlinear systems [68]-[69].

The T-S model is formally presented as a weighted average of several linear models through weighting functions. First, consider a finite set of linear models of the form:

$$\begin{aligned} \dot{x}(t) &= A_i x(t) + B_i u(t), \\ y(t) &= C_i x(t), \end{aligned} \quad (6.34)$$

for $i = 1, \dots, L$, where $A_i \in \mathbb{R}^{n \times n}$, $B_i \in \mathbb{R}^{n \times m}$, $C_i \in \mathbb{R}^{p \times n}$, and L denotes the number of linear models. Note that all matrices have dimensions independent of their index i .

The T-S model is defined as:

$$\Sigma : \begin{cases} \dot{x}(t) = \sum_{i=1}^L h_i(z(t)) (A_i x(t) + B_i u(t)), \\ y(t) = \sum_{i=1}^L h_i(z(t)) C_i x(t), \end{cases} \quad (6.35)$$

with $h_i(z(t)) \geq 0$ for $i = 1, \dots, L$, $\sum_{i=1}^L h_i(z(t)) = 1$ and $z(t)$ is a triggering variable, which is usually dependent on the current value of the system state $x(t)$. Observe that this makes (6.35) nonlinear.

6.4.1 Modified state feedback MRAC

In this section, a new adaptation law is proposed for state feedback MRAC. The adaptive control problem is formulated as a linear matrix inequality (LMI) feasibility problem to obtain the optimal adaptation gains.

State feedback MRAC

Suppose the system states are measured. The state feedback control law is defined as (6.5).

Define the new adaptation law as

$$\dot{\theta}(t) = \sum_{i=1}^L h_i(w(t)) (\Gamma_i e(t) + \beta_i \theta(t)) \quad (6.36)$$

with $h_i : \mathbb{R}^{n+1} \rightarrow \mathbb{R} \ \forall i$ s.t. $h_i(w) \geq 0$ and $\sum_{i=1}^L h_i(w) = 1$ for all $w \in \mathbb{R}^{1+n}$ and Γ_i and β_i are adaptation design variables.

Here, the state space is divided into a number of regions L and the triggering variable w chooses the proper adaptation gain based on the operating point. We assume that the

system is slowly time varying such that $\dot{\theta}_m(t) = 0$. Hence, the controller parameter error dynamics is defined as

$$\begin{aligned}\dot{\tilde{\theta}} &= b_p \dot{\theta}(t), \\ &= \sum_{i=1}^L h_i(w(t)) \left(b_p \Gamma_i e(t) + \beta_i (\tilde{\theta} + \theta_m) \right), \\ &= \sum_{i=1}^L h_i(w(t)) \left(\alpha_i e(t) + \beta_i (\tilde{\theta}(t) + \theta_m(t)) \right),\end{aligned}\quad (6.37)$$

with α_i and β_i denote the adaptation gains.

That allows the description of the error dynamics composed of the tracking error and the controller parameters estimation error are described by

$$\begin{bmatrix} \dot{e}(t) \\ \dot{\tilde{\theta}}(t) \end{bmatrix} = \begin{bmatrix} A_m & B_I w^\top \\ \sum_{i=1}^L h_i(w(t)) \alpha_i & \sum_{i=1}^L h_i(w(t)) \beta_i \end{bmatrix} \begin{bmatrix} e(t) \\ \tilde{\theta}(t) \end{bmatrix} + \begin{bmatrix} 0 \\ \sum_{i=1}^L h_i(w(t)) \beta_i \end{bmatrix} \theta_m(t).\quad (6.38)$$

The augmented system (6.38) is approximated at L different operating points $w_i \in \mathbb{R}^{1+n}$ by a T-S model:

$$\begin{bmatrix} \dot{e}(t) \\ \dot{\tilde{\theta}}(t) \end{bmatrix} = \sum_{i=1}^L h_i(w(t)) \left(\begin{bmatrix} A_m & B_I w_i^\top \\ \alpha_i & \beta_i \end{bmatrix} \begin{bmatrix} e(t) \\ \tilde{\theta}(t) \end{bmatrix} + \begin{bmatrix} 0 \\ \beta_i \end{bmatrix} \theta_m(t) \right).\quad (6.39)$$

Note that the design method is developed based on an interesting theoretical result called universal approximation [67]. The validity of using a T-S model as a universal approximator depends on using a sufficiently large number of subsystems. Here, we assume that the T-S model (6.39) represents the augmented system (6.38) arbitrary well.

In the sequel, we adopt the following abbreviations:

$$\tilde{e}(t) := \begin{bmatrix} e(t) \\ \tilde{\theta}(t) \end{bmatrix}, \quad \tilde{A}_i := \begin{bmatrix} A_m & B_I w_i^\top \\ \alpha_i & \beta_i \end{bmatrix}, \quad \text{and} \quad E_i := \begin{bmatrix} 0 \\ \beta_i \end{bmatrix}.$$

Therefore, the closed-loop system (6.39) is expressed as

$$\begin{aligned}\dot{\tilde{e}}(t) &= \sum_{i=1}^L h_i(w) \left(\tilde{A}_i \tilde{e}(t) + E_i \theta_m(t) \right), \\ \xi(t) &= M \tilde{e}(t),\end{aligned}\quad (6.40)$$

where $M \neq 0$ is an arbitrary output matrix that reflects our interest in specific components in $\tilde{e}(t)$. Now using the T-S model (6.40), the adaptive control problem is

formulated as the stabilization of the nonlinear system (6.40) and attenuation of the disturbance $\theta_m(t)$.

Towards this end, the objective is to design a state feedback controller (6.5) with the adaptive control law (6.36) such that the closed-loop system (6.40) has an \mathcal{L}_2 gain from θ_m to \tilde{e} less than or equal to $\rho > 0$. A convenient method of proving that a system has finite \mathcal{L}_2 gain is to prove existence of a (generalized) storage function. Specifically, a storage function $V(\tilde{e})$ associated with a quadratic supply rate $s(\theta_m, \tilde{e})$ is a positive definite function which satisfies the relationship

$$\int_0^T s(\theta_m(t), \tilde{e}(t)) dt \geq V(\tilde{e}(T)) - V(\tilde{e}(0)) \quad (6.41)$$

for all trajectories (θ_m, \tilde{e}) generated by the system (6.40).

If V is a storage function of the controlled system (6.40) which is dissipative with respect to

$$s(\theta_m, \tilde{e}) := \rho^2 \theta_m^\top \theta_m - \tilde{e}^\top \tilde{Q} \tilde{e},$$

for some $\tilde{Q} = M^\top M \succ 0$, then in particular for all $T \geq 0$

$$\int_0^T \|M\tilde{e}\|_2^2 dt - \rho^2 \|\theta_m\|_2^2 dt \leq 0 \quad \forall \theta_m \in \mathcal{L}_2(0, T), \quad (6.42)$$

provided that $\tilde{e}(0) = 0$. This shows that

$$\sup_{T>0} \sup \frac{\int_0^T \|M\tilde{e}\|_2^2 dt}{\int_0^T \|\theta_m\|_2^2 dt} \leq \rho^2. \quad (6.43)$$

Hence, the control law (6.5) with the adaptation law (6.36) achieves that the \mathcal{L}_2 gain in (6.40), with $\tilde{e}(0) = 0$, is less than ρ if (6.43) holds.

Theorem 6.4.1. *Using the state feedback control law (6.5) with the adaptation law (6.36), the error dynamics of the closed-loop system (6.40) is asymptotically stable if there exists a symmetric positive definite matrix P which satisfies the matrix inequality*

$$\tilde{A}_i^\top P + P\tilde{A}_i + \frac{1}{\rho^2} P E_i E_i^\top P + \tilde{Q} \prec 0, \quad i = 1, \dots, L \quad (6.44)$$

where $\tilde{Q} := M^\top M$

Proof. Consider the candidate storage function:

$$V(\tilde{e}) := \tilde{e}^\top P \tilde{e}.$$

The time derivative $\frac{d}{dt}V(\tilde{e}(t))$ along the system trajectories is given by:

$$\frac{d}{dt}V(\tilde{e}(t)) = \dot{\tilde{e}}^\top(t)P\tilde{e}(t) + \tilde{e}^\top(t)P\dot{\tilde{e}}(t).$$

Then using (6.40), we can write the following sequence of equalities:

$$\begin{aligned} \dot{V}(\tilde{e}(t)) &= \sum_{i=1}^L h_i \tilde{e}^\top \tilde{A}_i^\top P \tilde{e} + \tilde{e}^\top P \left(\sum_{i=1}^L h_i \tilde{A}_i \tilde{e} \right) + \theta_m^\top E_i^\top P \tilde{e} + \tilde{e}^\top P E_i \theta_m, \\ &= \sum_{i=1}^L h_i \tilde{e}^\top \left(\tilde{A}_i^\top P + P \tilde{A}_i + \frac{1}{\rho^2} P E_i E_i^\top P \right) \tilde{e} + \rho^2 \theta_m^\top \theta_m \\ &\quad - \left(\frac{1}{\rho} E_i^\top P \tilde{e} - \rho \theta_m \right)^\top \left(\frac{1}{\rho} P E_i^\top \tilde{e} - \rho \theta_m \right). \end{aligned}$$

Consequently,

$$\dot{V}(\tilde{e}(t)) \leq \sum_{i=1}^L h_i \tilde{e}^\top(t) \left(\tilde{A}_i^\top P + P \tilde{A}_i + \frac{1}{\rho^2} P E_i E_i^\top P \right) \tilde{e}(t) + \rho^2 \theta_m^\top \theta_m.$$

Or,

$$\dot{V}(\tilde{e}(t)) \leq \sum_{i=1}^L h_i \tilde{e}^\top(t) (-\tilde{Q}) \tilde{e}(t) + \rho^2 \theta_m^\top(t) \theta_m(t). \quad (6.45)$$

From the properties of $h_i(w(t))$, $\sum_{i=1}^L h_i = 1$, the inequality (6.45) therefore implies that:

$$\dot{V}(\tilde{e}(t)) \leq \rho^2 \theta_m^\top \theta_m - \tilde{e}^\top(t) \tilde{Q} \tilde{e}(t).$$

Integrating both sides from t_0 to t_1 shows that,

$$V(\tilde{e}(t_1)) - V(\tilde{e}(t_0)) \leq \rho^2 \int_{t_0}^{t_1} \theta_m^\top(t) \theta_m(t) dt - \int_{t_0}^{t_1} \tilde{e}^\top(t) \tilde{Q} \tilde{e}(t) dt.$$

That implies that the \mathcal{L}_2 gain performance specified in (6.43) is guaranteed.

Setting $\theta_m = 0$ in (6.45) implies that $\dot{V}(\tilde{e}(t)) \leq 0$ and therefore the error dynamics (6.40) is asymptotically stable. \square

LMI formulation

Linear matrix inequality (LMI) problems have received significant attentions over the last decades [73]-[74]. For systems and control, the importance of LMI optimization

stems from the fact that various control problems can be recast as LMI problems [73]. Finding a positive definite matrix $P = P^\top$ that solves (6.44) is the key solution of the adaptive control problem. Hence, the adaptation law gains, α_i and β_i , can be determined such that the closed-loop system (6.40) is asymptotically stable. Note that (6.44) is not an LMI, thus it is not easy to find a solution P nor the adaptation law gains α_i and β_i for (6.44). To formulate the inequalities (6.44) as an LMI feasibility problem, we apply the Schur complement [73] and change of variables.

Theorem 6.4.2. *Given the reference model (6.2) and the weighting matrices \tilde{Q}_1, \tilde{Q}_2 , consider the following linear matrix inequalities in the variables $P_1, P_2, \gamma_i, \lambda_i$:*

$$\begin{aligned} & \begin{bmatrix} P_1 & 0 \\ 0 & P_2 \end{bmatrix} \succ 0 \\ & \begin{bmatrix} H_{11} & H_{12} & 0 \\ H_{21} & H_{22} & H_{23} \\ 0 & H_{32} & H_{33} \end{bmatrix} \prec 0 \end{aligned} \quad (6.46)$$

where

$$\begin{aligned} H_{11} &= P_1 A_m + A_m^\top P_1 + \tilde{Q}_1, & H_{12} &= H_{21}^\top = P_1 B_I w_i^\top + \lambda_i^\top, \\ H_{22} &= \gamma_i + \gamma_i^\top + \tilde{Q}_2, & H_{23} &= H_{32}^\top = \gamma_i^\top, & H_{33} &= -\rho^2 I. \end{aligned}$$

Then for any feasible solution $\gamma_i, \lambda_i, P_1 \succ 0, P_2 \succ 0$ of (6.46), the adaptation law (6.36) with $\beta_i = P_2^{-1} \gamma_i$ and $\alpha_i = P_2^{-1} \lambda_i$ and the state feedback control law (6.4) are well defined and the corresponding closed-loop system (6.38) has a guaranteed \mathcal{L}_2 gain performance as specified in (6.43).

Proof. Suppose that

$$\tilde{Q} = \begin{bmatrix} \tilde{Q}_1 & 0 \\ 0 & \tilde{Q}_2 \end{bmatrix} \text{ and } P = \begin{bmatrix} P_1 & 0 \\ 0 & P_2 \end{bmatrix} \quad (6.47)$$

By substitution of (6.47) into (6.44) we get

$$\begin{bmatrix} D_{11} & D_{12} \\ D_{21} & D_{22} \end{bmatrix} \prec 0 \quad (6.48)$$

where

$$\begin{aligned} D_{11} &= P_1 A_m + A_m^\top P_1 + \tilde{Q}_1, \\ D_{12} &= D_{21}^\top = P_1 B_I w_i^\top + \alpha_i^\top P_2, \\ D_{22} &= P_2 \beta_i + \beta_i^\top P_2 + \frac{1}{\rho^2} P_2 \beta_i \beta_i^\top P_2 + \tilde{Q}_2, \end{aligned}$$

for $i = 1, 2, \dots, L$.

Applying the Schur complement on D_{22} and a change of variables $\gamma_i = P_2\beta_i$ and $\lambda_i = P_2\alpha_i$, we obtain that (6.48) and $P \succ 0$ are equivalent to (6.46). This completes the proof. \square

Now (6.46) is an LMI with P_1, P_2, γ_i and λ_i as variables, which can be solved using standard LMI optimization software. Therefore, the adaptive control problem can be formulated as the following minimization problem:

$$\begin{aligned} \min_{P_1, P_2, \gamma_i, \lambda_i} \quad & \rho^2 \\ \text{subject to} \quad & (6.46). \end{aligned} \tag{6.49}$$

6.4.2 Modified output feedback MRAC

In practice the plant states are not measurable and only the plant output is measurable. In this section, a modified output feedback MRAC using multiple adaptation gains is presented. An LMI feasibility problem is derived to synthesis the adaptation gains.

Output feedback MRAC

The output feedback control law is given by

$$u(t) = \theta^\top(t)w(t) \tag{6.50}$$

with

$$\theta^\top = \begin{bmatrix} K_{ff} & F^\top & K_{fb} & d^\top \end{bmatrix}$$

are the controller parameters and

$$w(t)^\top = \begin{bmatrix} r(t) & z_1^\top(t) & y_p(t) & z_2^\top(t) \end{bmatrix}.$$

The error equation is given by

$$\dot{e}(t) = A_m e(t) + B_m \tilde{\theta}^\top w(t), \tag{6.51}$$

where $e(t) = \begin{bmatrix} e_1 & \dot{e}_1 & \dots & e_1^{(n-1)} \end{bmatrix}^\top$ and $e_1(t) = y_p - y_m = C_m e(t)$.

Define the adaptation law as

$$\dot{\theta}(t) = \sum_{i=1}^L h_i(w(t)) (\alpha_i e_1(t) + \beta_i \theta(t)) \tag{6.52}$$

Hence, the augmented error is represented by a T-S model as

$$\dot{v}(t) = \sum_{i=1}^L h_i(w(t)) \left(\hat{A}_i v(t) + E_i \theta_m(t) \right), \quad (6.53)$$

with

$$v(t) := \begin{bmatrix} e(t) \\ \tilde{\theta}(t) \end{bmatrix} \quad \hat{A}_i := \begin{bmatrix} A_m & B_m w_i^\top \\ \alpha_i C_m & \beta_i \end{bmatrix} \quad \text{and} \quad E_i := \begin{bmatrix} 0 \\ \beta_i \end{bmatrix}.$$

Again, the adaptive control problem is considered as the stabilization of the augmented system (6.53) and the attenuation of the disturbance $\theta_m(t)$. The objective is to design the adaptation gains in the update law (6.52) and the output feedback controller (6.50) such that the error dynamics of the closed-loop system (6.53) has an \mathcal{L}_2 gain from the disturbance $\theta_m(t)$ to the augmented error vector $v(t)$ less than or equal to $\rho > 0$.

Theorem 6.4.3. *Using the output feedback control law (6.50) and the update law (6.52) guarantee that the closed-loop system is asymptotically stable if there exists a symmetric positive definite matrix P that satisfies the matrix inequalities*

$$\hat{A}_i^\top P + P \hat{A}_i + \frac{1}{\rho^2} P E_i E_i^\top P + \tilde{Q} \prec 0, \quad i = 1, \dots, L \quad (6.54)$$

Proof. It is similar to the state feedback case. □

LMI formulation

From the above analysis, the most important issue to design the MRAC is to find a common matrix $P \succ 0$ that satisfies the matrix inequalities (6.54). Since inequalities (6.54) are not convex, in general, it is difficult to find a solution $P \succ 0$ analytically. Fortunately, (6.54) can be reformulated as a minimization problem subject to some LMIs which can be solved in a computationally efficient manner using some standard convex optimization solvers. The following Theorem presents the synthesis of the adaptation law (6.52) in terms of an LMI feasibility problem.

Theorem 6.4.4. *Given the reference model (6.2) and the weighting matrices \tilde{Q}_1, \tilde{Q}_2 , consider the following linear matrix inequalities in the variables $P_1, P_2, \gamma_i, \lambda_i$:*

$$\begin{bmatrix} P_1 & 0 \\ 0 & P_2 \end{bmatrix} \succ 0 \quad (6.55)$$

$$\begin{bmatrix} G_{11} & G_{12} & 0 \\ G_{21} & G_{22} & G_{23} \\ 0 & G_{32} & G_{33} \end{bmatrix} \prec 0$$

where

$$\begin{aligned} G_{11} &= P_1 A_m + A_m^\top P_1 + \tilde{Q}_1, & G_{12} &= G_{21}^\top = P_1 B_m w_i^\top + C_m^\top \kappa_i^\top, \\ G_{22} &= \mu_i + \mu_i^\top + \tilde{Q}_2, & G_{23} &= G_{32}^\top = \mu_i^\top, & G_{33} &= -\rho^2 I. \end{aligned}$$

Then for any feasible solution $\mu_i, \kappa_i, P_1 \succ 0, P_2 \succ 0$ and (6.55), the adaptation law (6.52) with the adaptation gains $\beta_i = P_2^{-1} \mu_i$ and $\alpha_i = P_2^{-1} \kappa_i$ and the output feedback control law (6.50) are well defined and the corresponding closed-loop system (6.38) has guaranteed \mathcal{L}_2 gain performance as specified in (6.43).

Proof. Suppose that

$$\tilde{Q} = \begin{bmatrix} \tilde{Q}_1 & 0 \\ 0 & \tilde{Q}_2 \end{bmatrix} \text{ and } P = \begin{bmatrix} P_1 & 0 \\ 0 & P_2 \end{bmatrix}. \quad (6.56)$$

By substitution of (6.56) into (6.54) we get

$$\begin{bmatrix} S_{11} & S_{12} \\ S_{21} & S_{22} \end{bmatrix} \prec 0 \quad (6.57)$$

where

$$\begin{aligned} S_{11} &= P_1 A_m + A_m^\top P_1 + \tilde{Q}_1, \\ S_{12} &= S_{21}^\top = P_1 B_m w_i^\top + C_m^\top \alpha_i^\top P_2, \\ S_{22} &= P_2 \beta_i + \beta_i^\top P_2 + \frac{1}{\rho^2} P_2 \beta_i \beta_i^\top P_2 + \tilde{Q}_2, \end{aligned}$$

for $i = 1, 2, \dots, L$.

Applying the Schur complement on S_{22} and change of variables $\mu_i = P_2 \beta_i$ and $\kappa_i = P_2 \alpha_i$, we obtain that (6.57) and $P \succ 0$ is equivalent to the LMI (6.55). This completes the proof. \square

Note that (6.55) is an LMI with P_1, P_2, μ_i and κ_i as variables, which can be solved using dedicated LMI optimization software. Similarly, the output-feedback adaptive control problem is transformed to the following minimization problem

$$\begin{aligned} & \min_{P_1, P_2, \mu_i, \kappa_i} \rho^2 \\ & \text{subject to } (6.55). \end{aligned} \quad (6.58)$$

6.5 Numerical comparison

This section presents a comparison example to show the effectiveness of both MRAC designs with the nonlinear adaptation gain and multiple adaptation gain. Consider a

second order system [55]

$$G_p = \frac{12}{s^2 + 2s + 8},$$

the reference model is described by the state space realization

$$\begin{aligned}\dot{x}_m(t) &= A_m x(t) + B_m u(t), \\ y_m(t) &= C_m x(t),\end{aligned}$$

where

$$A_m = \begin{bmatrix} 0 & 1 \\ -8 & -16 \end{bmatrix}, \quad B_m = \begin{bmatrix} 0 \\ 16 \end{bmatrix} \text{ and } C_m = [1 \quad 0].$$

Here, we consider two design cases

- State feedback MRAC

Suppose that all the states are measurable. First we consider the MRAC design with the nonlinear adaptation gain, the controller is constructed using control law (6.5) and adaptive law (6.11) with the time varying adaptation gain (6.24). Figure 6.4 shows the states responses for both the nonlinear and constant adaptation gain. It is clear that using the nonlinear adaptation gain (6.24) the convergence speed increases considerably.

A further improvement is obtained using the proposed adaptive law (6.36). The nonlinear system (6.38) is approximated with a T-S model with $L = 9$ for the given example. Figure 7.1 shows an example of the weighting functions $h_i(z(t))$ for the triggering variable $z(t) = w(t)$. The optimal adaptation gains α_i and β_i are obtained by solving the optimization problem (6.49). Figure 6.5 shows the system state trajectory and the reference model states using the proposed and the standard MRAC. As shown, a faster convergence is achieved by using the proposed update law (6.36).

- Output feedback MRAC

In this case, only the system output, $y = x_1$, is measurable, applying the augmented error method with the primary control structure shown in Figure 6.2 and the adaptive laws with constant and nonlinear adaptation gain. Figure 6.6 shows the system response in case of output feedback MRAC for both nonlinear and constant adaptation gain. The adaptation (implicit identification) phase is much shorter. On the other hand, we construct the controller based on the control law (6.50) with the multiple adaptation law (6.52). We found by Theorem 6.4.4 that the optimal $\rho^2 = 0.7$ after several optimization iterations. Figure 6.7 compares

the system response of both the proposed and standard MRAC. The multiple adaptation gain demonstrates fast adaptation, which is needed to deal with large uncertainties. The adaptation phase is much shorter (about ten times) compared with the standard MRAC.

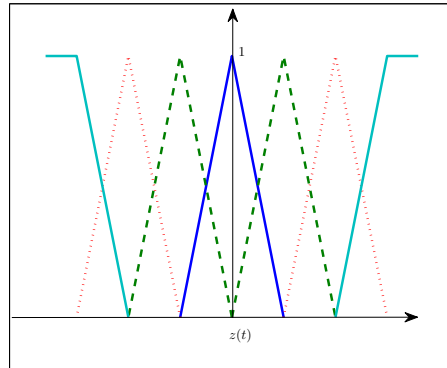


Figure 6.3: The weighting functions $h_i(w(t))$

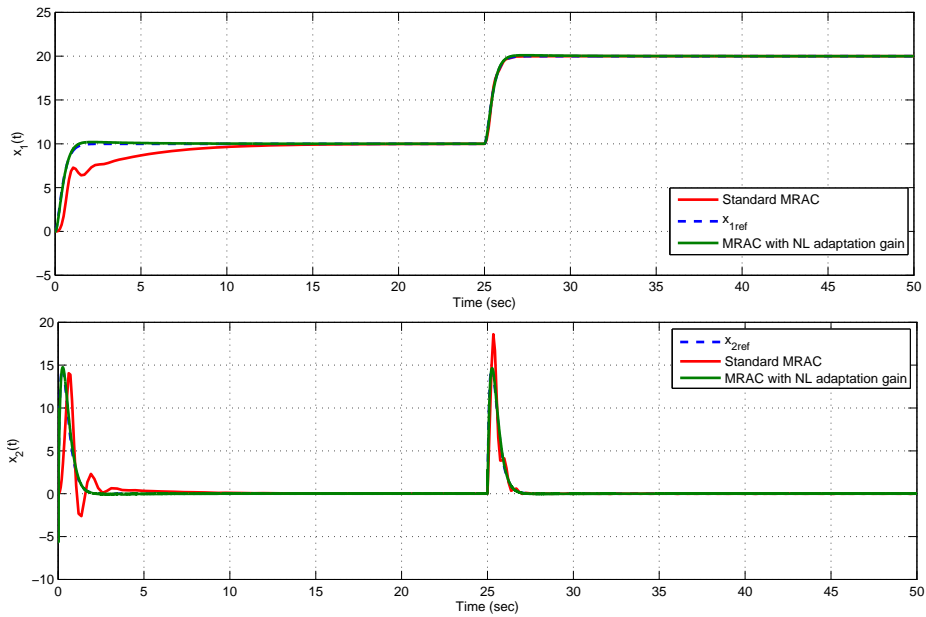


Figure 6.4: State feedback for fixed and nonlinear adaptation gain (6.24)

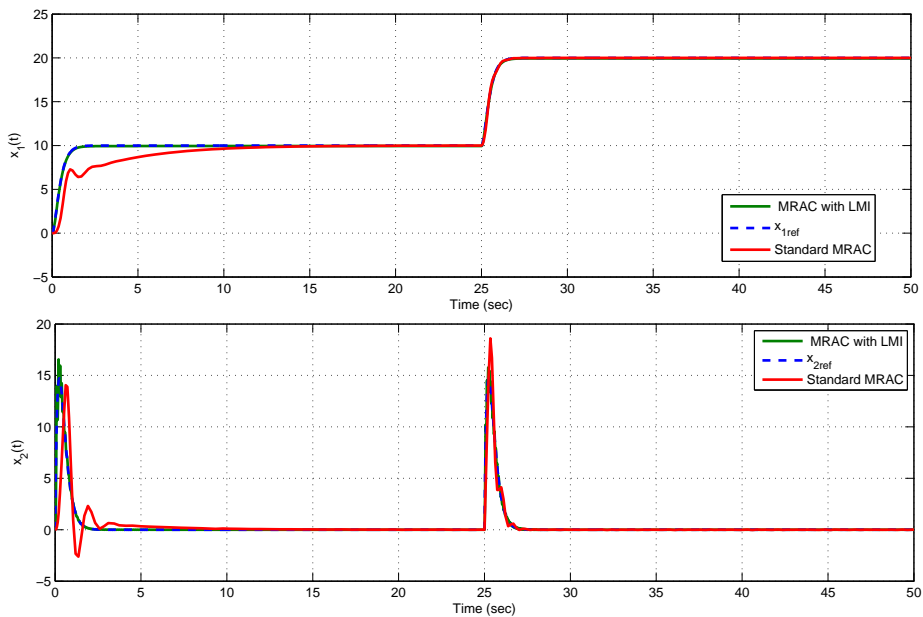


Figure 6.5: State feedback for standard MRAC and the proposed adaptive control (6.46)

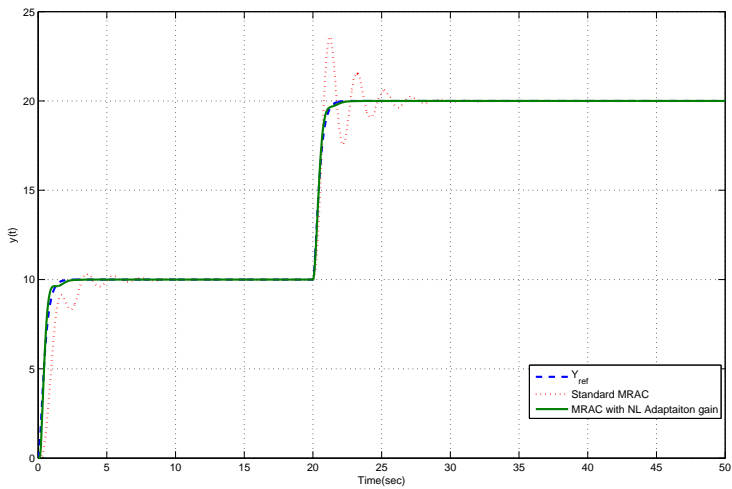


Figure 6.6: The trajectories of the output variable y : the adaptive control with nonlinear adaptation gain (solid-line), the standard MRAC (dashed-line), and reference state y_r (dotted-line)

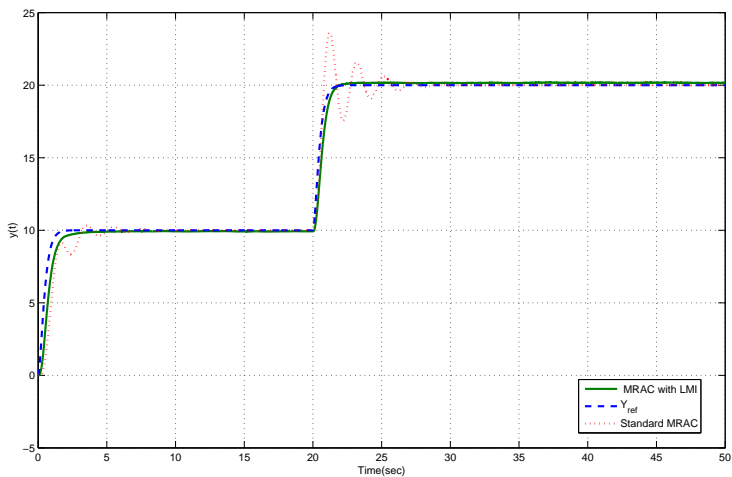


Figure 6.7: The trajectories of the output variable y : the proposed adaptive control in Theorem 6.4.4 (solid-line), the standard MRAC (dashed-line), and reference state y_r (dotted-line)

6.6 Application of MRAC for laser printing system

As mentioned in chapter 5, the major issues that are encountered in the printing system are related to large and fast parameter variations (paper size, weight, and humidity) and nonlinearities. These problems influence the performance of the printing system. Good quality means that the fusing temperature should be at a certain desired print job dependent temperature level for all different print jobs. Currently, an industrial PI controller is implemented in the printing system to control the preheating and TTF temperatures. The advantages of the PI controller include simple structure, easy to design and implement, and no need for an accurate model of the process. However, a PI controller has some difficulties in the presence of nonlinearities, it does not react to changing process behavior, and is slow in responding to large disturbances.

Based on the printer characteristics, MRAC is suggested to control the fuse temperature. The objective is to design a controller to keep both the printing quality and the productivity as good as possible. In this section, we present a comparison of the tracking control results of the existing industrial PI controller and the proposed MRAC approaches.

The printing system (5.1) is defined as model (6.1) with state vector defined as

$$x = \begin{bmatrix} T_{pre} \\ T_{TTF} \\ T_{roller} \\ T_{slow} \end{bmatrix},$$

which represents the temperature at different locations. The control input is

$$u(t) = \begin{bmatrix} P_{pre}(t) \\ P_{TTF}(t) \end{bmatrix},$$

and the measured output is

$$y(t) = \text{col}(T_{pre}(t), T_{fuse}(t)).$$

Several parameters of the printing system are time varying since these parameters depend on the different printing jobs, while other parameters are unknown. As shown in Figure 6.8 the paper mass and the drive speed are varied to simulate the parameter variations.

The reference models (6.16) for the preheater and the TTF are chosen as

$$A_{r_{pre}} = -0.5, \quad B_{r_{pre}} = 0.5, \quad C_{r_{pre}} = 1.$$

$$A_{r_{TTF}} = \begin{bmatrix} 0 & 1 & 0 \\ 0 & 0 & 1 \\ -0.125 & -0.75 & -1.5 \end{bmatrix}, \quad B_{r_{pre}} = \begin{bmatrix} 0 \\ 0 \\ 0.125 \end{bmatrix}, \quad C_{r_{pre}} = [1 \ 0 \ 0].$$

Since the fusing temperature depends on the preheating and the TTF temperature, we apply Theorem 6.3.2 with the nonlinear adaptation gain to control both the preheating and TTF temperature. We also implement the adaptive control law (6.50) with the multiple adaptation law (6.52). To construct the T-S model (6.53), we assume that the $w_{pre} \in [\mathcal{N}_{min}, \mathcal{N}_{max}]$ and $w_{TTF} \in [\mathcal{M}_{min}, \mathcal{M}_{max}]$. We choose

$$\mathcal{N}_{min} = col(50, 50), \mathcal{N}_{max} = col(100, 100), \mathcal{M}_{min} = col(0, 0, 0, 0),$$

$$\text{and } \mathcal{M}_{max} = col(100, 100, 1000, 1000).$$

The LMI problem (6.58) is feasible with an optimal $\rho_{pre}^2 = 0.5$ and $\rho_{TTF}^2 = 0.4$ for the preheating and the TTF systems, respectively. The triangle weighting functions, see Figure 6.3, are adopted for this approach.

Figure 6.9 compares the fusing temperature tracking error of the existing industrial PI controller, the MRAC with a nonlinear adaptation gain, and the MRAC with multiple adaptation gains. As depicted, the tracking performance of both MRAC schemes is better than that of the PI controller in the presence of the large parameter variations. Figure 6.10 presents the preheating temperature tracking of different temperature levels with paper mass variations. These simulation results elucidate that the proposed MRAC schemes can efficiently improve the performance of the printing system in the presence of large parameters variations.

Note that using MRAC with a nonlinear adaptation gain guarantees a faster convergence of the tracking error to zero but it does not guarantee the convergence of the controller parameters to the optimal value. On the other hand, employing the adaptive law (6.52) yields to the convergence of both the tracking and the controller parameters errors. Thanks to the representation of the augmented error as a T-S model, the adaptive problem is formulated as an LMI feasibility problem and, therefore, the adaptation gains are optimally obtained. That explain the better performance of the MRAC with multiple adaptation gain compared with the MRAC with the nonlinear adaptation gain.

6.7 Conclusions

This chapter has addressed two different approaches for an improved convergence of MRAC using a nonlinear varying adaptation gain and a multiple adaptation gain. The adaptation gain has been chosen to be a function of the error to speed up the adaptation process when the error is large. The proposed design yields a faster error convergence for both state and output feedback compared with a constant adaptation gain. A new Lyapunov function has been introduced to prove the stability of the system when applying the proposed MRAC. In addition, multiple adaptation gains are employed to improve the convergence of the adaptation law. The nonlinear error dynamics composed

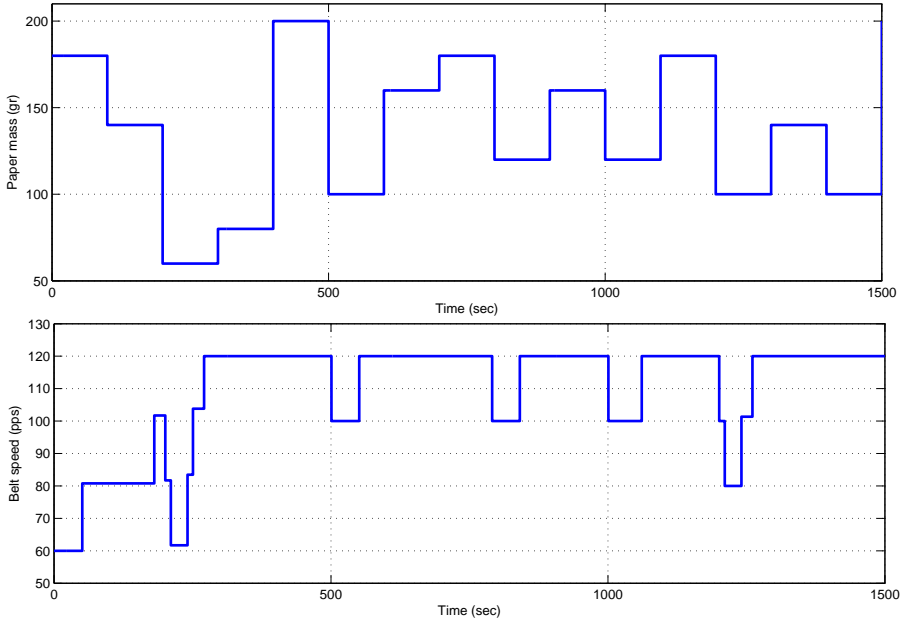


Figure 6.8: The variation of the paper mass and the transfer belt speed.

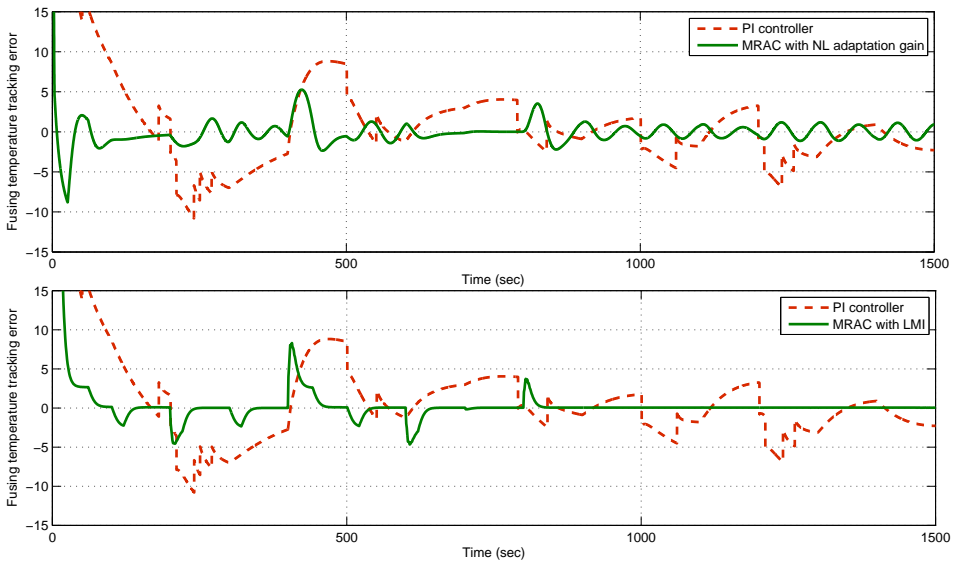


Figure 6.9: Fusing temperature tracking error.

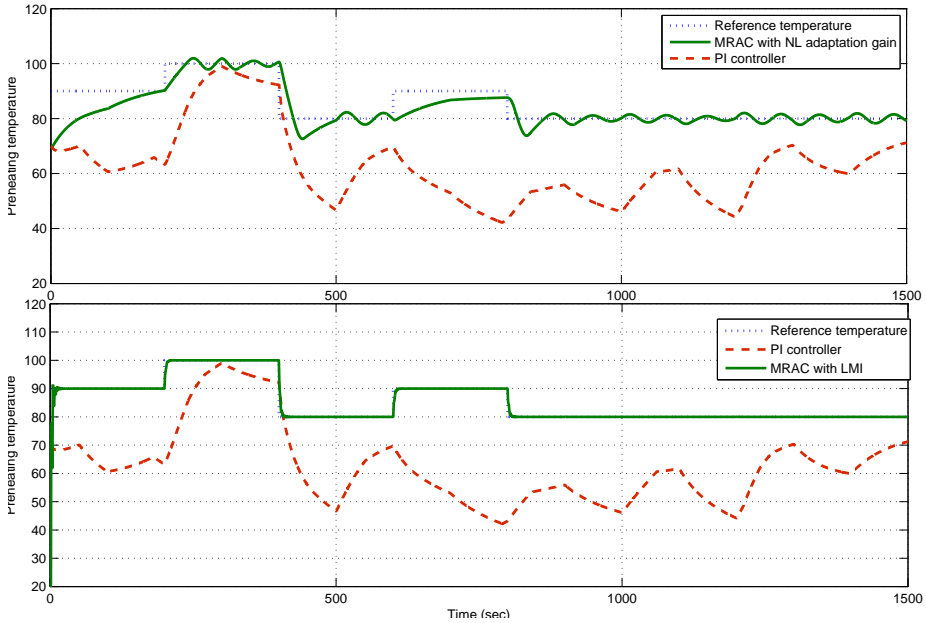


Figure 6.10: Preheating temperature tracking control comparison.

of the tracking error and the controller parameters error has been approximated by a T-S model. Based on the proposed formulation, the adaptive control synthesis problem is formulated as an LMI feasibility problem, which can efficiently be solved using dedicated numerical solvers. The proposed design yields a faster error convergence for both state and output feedback controller when compared with a constant adaptation gain. The proposed approaches are used to control a printing system. Simulations with the printing system illustrated the effectiveness of the proposed techniques. A good tracking and robust stability has been obtained for large parameter variations. Moreover, the proposed MRAC show that the printing quality can be considerably improved in the presence of large and fast parameter variations compared with the present industrial controller.

Chapter 7

Robust \mathcal{L}_2 Control for a Professional Printing System

In this chapter, the robust control problem of a laser printing system, using an \mathcal{L}_2 state and output feedback controller, is addressed. The nonlinear printing system is approximated by a Takagi-Sugeno (T-S) model. A robust control technique is proposed to cope with the effect of the approximation error between the nonlinear model of the printing system and the approximating T-S model. A sufficient condition is derived to ensure robust stability of an \mathcal{L}_2 state and output feedback controller with a guaranteed disturbance attenuation level. A technique based on a parameterized Lyapunov function is employed in our approach. After a transformation the problem is formulated in terms of a linear matrix inequality for which efficient optimization solvers are used to test feasibility. Simulation results illustrate the performance and the validity of the proposed approach.

7.1 Introduction

The Takagi-Sugeno (T-S) model-based approach has nowadays become popular since it showed its efficiency to control complex nonlinear systems and has been used for many applications. Commonly a T-S model is used to approximate a nonlinear system and in that case the weights in the T-S model depend on the operating point of the nonlinear system. Furthermore, T-S models are closely related to piece-wise linear (PWL) and piece-wise affine (PWA) models. Specifically, a T-S model can be seen as a convex combination of a number of linear systems. It has been proven that T-S models can efficiently approximate any smooth nonlinear dynamic system [67]. T-S models have led to various designs of feedback controllers in which local controllers are combined to get an overall control law [75]-[76]. Recently, T-S type of controllers have been successfully applied to the stabilizing control design of nonlinear systems [77]-[83].

The T-S model structure has been used as a feasible approach to capture the plant dynamic characteristics under different operating conditions. The approximation error (or misfit) between the original nonlinear plant and the T-S model is known as the *consequence uncertainty*. Designing a controller based on the T-S model might not guarantee the stability of the original nonlinear system under such a controller. Robust control design alleviates this problem. Robust stabilization is well developed and investigated for linear systems and its many variations and generalizations to time-varying and nonlinear systems [85]-[89]. In [86], a sufficient condition for the stability of the output feedback control for a nonlinear system under a mixed H_2/H_∞ constraints is derived. Recently, in the same context, the problem of robust H_∞ dynamic output feedback control for uncertain fuzzy systems with multiple time scales has been considered [88]. The standard approach to analyze the issues of robust stability and stabilization in a T-S framework is mainly based on the existence of a common quadratic Lyapunov function guaranteeing stability. Most of these conditions can be represented as an LMI feasibility test, which is verified using convex optimization techniques, but are generally conservative.

Generally, it is difficult to find a common quadratic Lyapunov function for a finite number of LTI systems, even for stable T-S models. Several approaches have been proposed to relax this conservatism. Some results have employed piecewise quadratic Lyapunov functions [81]. These functions are composed of several quadratic Lyapunov functions, each of them is active in a single region in a partitioning of the state space. Several boundary conditions should be satisfied due to the discontinuities of the function across the subset boundaries. However, using piecewise Lyapunov functions for controller design leads to a non convex optimization problem. In [78], an approach for the construction of parameterized Lyapunov function (PLF) has been developed. This function consists of a weighted sum of several quadratic Lyapunov functions. The weights are the same as the ones used in the T-S model. Unlike piecewise Lyapunov function ap-

proach, the PLF is smooth. Hence, it does not require any boundary condition to be satisfied. Using the PLF leads to a considerable relaxation of the conservatism and motivates more research in that direction.

In this chapter, we use the T-S model to approximate the dynamics of the printing system at different operating conditions. By taking the approximation error between the printing system and the T-S model into account, an \mathcal{L}_2 gain state and output feedback controller is proposed to achieve robust stability with the desired \mathcal{L}_2 gain performance. Towards this objective, the parameterized Lyapunov function technique is employed in our approach instead of the conventional quadratic Lyapunov function. This Lyapunov function presents a significantly wider class of functions than the conventional quadratic one and is, therefore, applicable to more general nonlinear systems. We believe that this flexibility leads to less conservative and higher performance design. The initial formulation of the considered \mathcal{L}_2 gain problem is necessarily given in terms of a nonlinear matrix inequality. A transformation is proposed to formulate the problem as an LMI feasibility problem, which is efficiently solved using dedicated solvers.

The remainder of the chapter is organized as follows. The basic definitions of the T-S model and a formulation of the robust control problem are presented in section 7.2. Section 7.3 introduces \mathcal{L}_2 gain based state feedback control. In section 7.4, an \mathcal{L}_2 gain observer-based output feedback control is illustrated. Section 7.5 presents the LMI formulation for control synthesis. A simulation example is given in section 7.6 to elucidate the design effectiveness. The application of the robust control design to a professional printing system is given in section 7.7. Concluding remarks are collected in section 7.8.

7.2 Problem formulation

Consider the nonlinear system

$$\begin{aligned} \dot{x}(t) &= F(x(t)) + G(x(t))u(t) + w(t), \\ y(t) &= H(x(t)), \end{aligned} \tag{7.1}$$

where $x(t) \in \mathbb{R}^n$ is the state vector, $y(t) \in \mathbb{R}^p$ is the process output, $u(t) \in \mathbb{R}^m$ denotes the control input, $w(t) \in \mathbb{R}^n$ denotes an unknown but bounded disturbance and $F(x(t))$, $G(x(t))$ are smooth (continuously differentiable) functions with $F(0) = 0$.

The nonlinear system (7.1) is represented using a T-S model as follows:

$$\begin{aligned} \dot{x}(t) &= \sum_{i=1}^r h_i(z(t)) (A_i x(t) + B_i u(t) + w(t)), \\ y(t) &= \sum_{i=1}^r h_i(z(t)) C_i x(t), \end{aligned} \tag{7.2}$$

with for all i $h_i : \mathbb{R}^z \rightarrow \mathbb{R}_+$ and $\sum_{i=1}^r h_i(z) = 1$ for all $z \in \mathbb{R}^z$ is the scheduling or triggering variable, which is used to determine what operating region the system is currently in and to enable the appropriate linear model, $A_i \in \mathbb{R}^{n \times n}$, $B_i \in \mathbb{R}^{n \times m}$, $C_i \in \mathbb{R}^{p \times n}$ and r is the number of subsystems.

The nonlinear system (7.1) is rearranged as

$$\begin{aligned} \dot{x}(t) &= \sum_{i=1}^r h_i(z(t))(A_i x(t) + B_i u(t)) + w(t) \\ &+ \underbrace{(F(x(t)) - \sum_{i=1}^r h_i(z(t))A_i x(t))}_{\Delta F(t)} + \underbrace{(G(x(t)) - \sum_{i=1}^r h_i(z(t))B_i u(t))}_{\Delta G(t)}, \\ y(t) &= \sum_{i=1}^r h_i(z(t))C_i x(t) + \underbrace{H(x(t)) - \sum_{i=1}^r h_i(z(t))C_i x(t)}_{\Delta H(t)}. \end{aligned}$$

Hence, the nonlinear system (7.1) is given as

$$\begin{aligned} \dot{x}(t) &= \sum_{i=1}^r h_i(z(t))(A_i x(t) + B_i u(t)) + \Delta F(t) + \Delta G(t) + w(t), \\ y(t) &= \sum_{i=1}^r h_i(z(t))C_i x(t) + \Delta H(t), \end{aligned} \tag{7.3}$$

where $\Delta F(t)$, $\Delta G(t)$, and $\Delta H(t)$ denote the approximation errors between the nonlinear system (7.1) and the T-S system (7.2). Assume that $\mathcal{U} \subset \mathbb{R}^{n \times n} \times \mathbb{R}^{n \times m} \times \mathbb{R}^{p \times n}$ is an uncertainty set in which $(\Delta F(t), \Delta G(t), \Delta H(t))$ resides for all $t \geq 0$. We recall the definition of dissipativity and the dissipativity characterization of the upper bounds for the \mathcal{L}_2 gain.

Let $\bar{w} := \text{col}(u, w)$ denote the inputs of the nonlinear system (7.1), (7.3).

Definition 7.2.1. *The system (7.3) with state $x \in \mathbb{R}^n$, input $\bar{w} \in \mathbb{R}^{m_w}$ and output $y \in \mathbb{R}^p$, is robustly dissipative with respect to the supply function $s : \mathbb{R}^{m_w} \times \mathbb{R}^p \rightarrow \mathbb{R}$ if there exists a positive definite continuous function $V : \mathbb{R}^n \rightarrow \mathbb{R}_+$, called a storage function, which satisfies $V(0) = 0$ and $V(x(t_1)) - V(x(t_0)) \leq \int_{t_0}^{t_1} s(\bar{w}(t), y(t)) dt$ for all $t_1 \geq t_0$, and for all corresponding solutions (\bar{w}, x, y) to the system (7.3) and all uncertainties $(\Delta F, \Delta G, \Delta H) \in \mathcal{U}$ on the interval $[t_0, t_1]$.*

Definition 7.2.2. *The system (7.3) has robust \mathcal{L}_2 -gain $\rho \geq 0$ if ρ is the smallest number*

such that

$$\sup_{T>0} \sup_{0 \neq \bar{w} \in \mathcal{L}_2} \frac{\int_0^T \|y(t)\|_2^2 dt}{\int_0^T \|\bar{w}(t)\|_2^2 dt} \leq \rho^2$$

for all solutions $y(t)$ of (7.3) corresponding to input \bar{w} , $x(0) = 0$ and all uncertainties $(\Delta F, \Delta G, \Delta H) \in \mathcal{U}$.

Proposition 7.2.1. *The system (7.3) has a robust \mathcal{L}_2 -gain ρ if and only if it is robustly dissipative with respect to the supply function $s(\bar{w}, y) = \rho^2 \bar{w}^\top \bar{w} - y^\top y$.*

Proof. If the system is robustly dissipative, then there exists

$$V : \mathbb{R}^n \rightarrow \mathbb{R}_+ \quad \text{s.t.}$$

$$V(x(T)) - V(x(0)) \leq \int_0^T \rho^2 \|\bar{w}(t)\|_2^2 - \|y(t)\|_2^2 dt.$$

Let $x(0) = 0$ and since $V(x(T)) \geq 0$ we infer

$$\int_0^T \|y(t)\|_2^2 dt \leq \int_0^T \rho^2 \|\bar{w}(t)\|_2^2 dt.$$

In particular,

$$\frac{\int_0^T \|y(t)\|_2^2 dt}{\int_0^T \|\bar{w}(t)\|_2^2 dt} \leq \rho^2.$$

So also,

$$\sup_{T>0} \sup_{0 \neq \bar{w} \in \mathcal{L}_2} \frac{\int_0^T \|y(t)\|_2^2 dt}{\int_0^T \|\bar{w}(t)\|_2^2 dt} \leq \rho^2$$

□

7.3 Robust state feedback control

In this section, we consider the robust state feedback controller synthesis problem with a guaranteed \mathcal{L}_2 control performance [84]. Suppose that the system states are measurable. Define the state feedback control law as follows

$$u(t) = \sum_{j=1}^L h_j(z(t)) K_j [P_n(z(t))]^{-1} x(t) \quad (7.4)$$

where K_j are the controller gains for $j = 1, \dots, L$ and $P_n(z) = \sum_{k=1}^L h_k(z)P_k$ with $P_k > 0$ is an arbitrary positive definite matrix for $z \in \mathbb{R}^n$ and $k = 1, \dots, L$. Note that $P_n(z)$ is invertible as any convex combination of positive definite matrices is positive definite.

Hence, the closed-loop system is given as

$$\begin{aligned} \dot{x} &= \sum_{i=1}^L \sum_{j=1}^L h_i(z(t))h_j(z(t)) (A_i + B_i K_j P_n^{-1}) x(t) + \Delta F(t) \\ &\quad + \Delta G(t) + w(t) \end{aligned} \quad (7.5)$$

$$\dot{x} = \sum_{i=1}^L \sum_{j=1}^L h_i(z(t))h_j(z(t))A_{ij}(z)x(t) + \Delta F(t) + \Delta G(t) + w(t)$$

with $A_{ij} = A_i + B_i K_j P_n^{-1}$. Suppose that for the trajectory $x(t)$, there exist bounding matrices $\Delta A_i \in \mathbb{R}^{n \times n}$ and $\Delta B_i \in \mathbb{R}^{n \times m}$ such that for all $t \in \mathbb{R}$ and $z \in \mathbb{R}^n$

$$\|\Delta F(t)\| \leq \left\| \sum_{i=1}^L h_i(z(t))\Delta A_i x(t) \right\| \quad (7.6)$$

$$\|\Delta G(t)\| \leq \left\| \sum_{j=1}^L \sum_{i=1}^L h_i(z(t))h_j(z(t))\Delta B_i K_j P_n^{-1}(z)x(t) \right\| \quad (7.7)$$

where, for $i = 1, \dots, L$

$$\begin{aligned} \Delta A_i &\in \{ \delta_i \Delta A \mid |\delta_i| \leq 1 \} \\ \Delta B_i &\in \{ \eta_i \Delta B \mid |\eta_i| \leq 1 \} \end{aligned} \quad (7.8)$$

Obviously, according to the assumptions (7.6) and (7.7), the uncertainties reflect the worst case if $\Delta A_i = \delta_i \Delta A$, $\Delta B_i = \delta_i \Delta B$ such that (7.6) and (7.7) hold for some $|\delta_i| \leq 1$ and $|\eta_i| \leq 1$ for $i = 1, \dots, L$. For convenience we denote $h_i(z(t))$, $h_j(z(t))$, and $h_k(z(t))$ h_i , h_j , and h_k , respectively.

According to the above assumption, we obtain for all $t \geq 0$ and all $z \in \mathbb{R}^n$

$$(\Delta F(t))^\top (\Delta F(t)) \leq (\Delta A x(t))^\top (\Delta A x(t)). \quad (7.9)$$

Moreover,

$$(\Delta G(t))^\top (\Delta G(t)) \leq \left(\sum_{j=1}^L h_j \Delta B K_j P_n^{-1} x(t) \right)^\top \left(\sum_{j=1}^L h_j \Delta B K_j P_n^{-1} x(t) \right). \quad (7.10)$$

Based on these assumptions, the approximation error in the closed loop system is bounded by the specified structure of the bounding matrices $\Delta A \in \mathbb{R}^{n \times n}$ and $\Delta B \in \mathbb{R}^{n \times m}$. For more details about how to determine these bounding matrices see [86].

For a given value of $\rho > 0$, the objective is to design a state feedback controller (7.4) such that (7.5) has \mathcal{L}_2 gain from w to $y = x$ is less than or equal to ρ . The typical method of proving that a system has a finite \mathcal{L}_2 gain is to prove existence of a storage function [89]. Specifically, a storage function $V(x)$ associated with a quadratic supply rate $s(w(t), x(t))$ is a positive definite function which satisfies the relationship

$$\int_0^t s(w(\tau), x(\tau)) d\tau \geq V(x(t)) - V(x(0)) \quad (7.11)$$

for all trajectories (w, x) generated by the uncertain system (7.5) and for all $t \geq 0$.

By Definition 7.2.1, if V is a storage function of the controlled system (7.5) which is robustly dissipative with respect to $s(w(t), x(t)) := \rho^2 w^\top w - x^\top Q x$, $Q \succ 0$, then in particular $\forall T \geq 0$

$$\int_0^T \left\| Q^{\frac{1}{2}} x(t) \right\|_2^2 dt - \rho^2 \|w(t)\|_2^2 dt \leq 0 \quad \forall w \in \mathcal{L}_2(0, T) \quad (7.12)$$

which shows that

$$\sup_{T > 0} \sup \frac{\int_0^T \left\| Q^{\frac{1}{2}} x(t) \right\|_2^2 dt}{\int_0^T \|w(t)\|_2^2 dt} \leq \rho^2. \quad (7.13)$$

Hence, the control law (7.4) achieves that the \mathcal{L}_2 gain in (7.5) is less than ρ if (7.13) holds for $Q = I$.

Theorem 7.3.1. *Suppose that for $k = 1, \dots, L$, $\left\| \dot{h}_k \right\| = \left\| \frac{dh_k}{dz} \frac{dz}{dt} \right\| \leq \mu_k$ for all $t \geq 0$, $\mu_k > 0$ and $\rho > 0$. If there exist symmetric positive definite matrices P_k that satisfy the following matrix inequalities:*

$$\begin{aligned} A_{ij}^\top P_n^{-1} + P_n^{-1} A_{ij} - P_n^{-1} \hat{P} P_n^{-1} + \left(\frac{1}{\rho^2} + 2 \right) P_n^{-1} P_n^{-1} + \Delta A^\top \Delta A \\ + P_n^{-1} (K_j \Delta B)^\top (K_j \Delta B) P_n^{-1} + Q \prec 0, \end{aligned} \quad (7.14)$$

for all i, j such that $h_i h_j \neq 0$, with $\hat{P} = \sum_{k=1}^L \mu_k P_k$, then the control law (7.4) is well defined and the corresponding closed loop system (7.5) has guaranteed \mathcal{L}_2 gain performance as specified in (7.12).

Proof. Consider the candidate storage function:

$$\begin{aligned} V(x) &:= x^\top \left(\sum_{k=1}^L h_k(z) P_k \right)^{-1} x \\ &= x^\top P_n^{-1}(z) x. \end{aligned}$$

The time derivative $\frac{d}{dt}V(x(t))$ along the systems trajectories is given by:

$$\frac{d}{dt}V(x(t)) = \dot{x}^\top P_n^{-1} x + x^\top P_n^{-1} \dot{x} - x^\top P_n^{-1} \dot{P}_n P_n^{-1} x.$$

Then using (7.5), we can write the following sequence of equalities and inequalities:

$$\begin{aligned} \dot{V}(x(t)) &= \sum_{i=1}^L \sum_{j=1}^L h_i h_j x^\top (A_{ij}^\top P_n^{-1} + P_n^{-1} A_{ij}) x + \Delta F^\top P_n^{-1} x \\ &\quad + x^\top P_n^{-1} \Delta F + \Delta G^\top P_n^{-1} x + x^\top P_n^{-1} \Delta G + w^\top P_n^{-1} x + x^\top P_n^{-1} w \\ &\quad - x^\top P_n^{-1} \dot{P}_n P_n^{-1} x, \\ &= \sum_{i=1}^L \sum_{j=1}^L h_i h_j x^\top (A_{ij}^\top P_n^{-1} + P_n^{-1} A_{ij} - P_n^{-1} \dot{P}_n P_n^{-1}) x \\ &\quad - (x P_n^{-1} - \Delta F)^\top (x P_n^{-1} - \Delta F) - (x P_n^{-1} - \Delta G)^\top (x P_n^{-1} - \Delta G) \\ &\quad - \left(\frac{1}{\rho} x P_n^{-1} - \rho w \right)^\top \left(\frac{1}{\rho} x P_n^{-1} - \rho w \right) + \rho^2 w^\top w + \Delta F^\top \Delta F \\ &\quad + \Delta G^\top \Delta G + \left(2 + \frac{1}{\rho^2} \right) x^\top P_n^{-1} P_n^{-1} x, \end{aligned}$$

using the assumptions (7.9) and (7.10) implies

$$\begin{aligned} &\leq \sum_{i=1}^L \sum_{j=1}^L h_i h_j x^\top (A_{ij}^\top P_n^{-1} + P_n^{-1} A_{ij} - P_n^{-1} \hat{P} P_n^{-1} + \Delta A^\top \Delta A \\ &\quad + \left(\frac{1}{\rho^2} + 2 \right) P_n^{-1} P_n^{-1} + P_n^{-1} (K_j \Delta B)^\top (K_j \Delta B) P_n^{-1}) x + \rho^2 w^\top w \end{aligned} \quad (7.15)$$

From the properties of h_i , and using (7.14) the inequality (7.15) implies the following inequality

$$\dot{V}(x(t)) \leq x^\top(t) (-Q) x(t) + \rho^2 w^\top(t) w(t).$$

Integrating both sides from 0 to t_f we obtain,

$$\int_0^{t_f} x^\top(t) Q x(t) dt \leq x^\top(0) P_n^{-1} x(0) + \rho^2 \int_0^{t_f} w^\top(t) w(t) dt$$

Since the previous inequality holds for any $t_f > 0$, the \mathcal{L}_2 gain performance is achieved with a prescribed ρ . \square

Theorem 7.3.2. *Suppose that for $k = 1, \dots, L$, and for all $t \geq 0$ $\|\dot{h}_k\| \leq \mu_k$, $\mu_k > 0$. Given the closed loop system (7.5), if there exist symmetric positive definite matrices P_k such that the matrix inequalities (7.14) are satisfied, then the closed loop system is quadratically stable.*

Proof. if we set $w(t) = 0$, from (7.15) and (7.14) we obtain

$$\dot{V}(x(t)) < -x^\top(t)Qx(t) < 0.$$

Therefore, the closed loop system (7.5) is quadratically stable. \square

7.4 Robust output feedback control

In this section, we consider the robust observer-based output feedback controller synthesis with a guaranteed \mathcal{L}_2 control performance [87]. In practical applications, the states may be unmeasurable. A state observer is introduced as follows

$$\begin{aligned} \dot{\hat{x}} &= \sum_{i=1}^r h_i(z(t)) (A_i \hat{x}(t) + B_i u(t) + L_i (y(t) - \hat{y}(t))) \\ \hat{y}(t) &= \sum_{i=1}^r h_i(z(t)) C_i \hat{x}(t) \end{aligned} \quad (7.16)$$

where L_i is the observer gain for $i = 1, \dots, r$. Define the control law as follows

$$u(t) = \sum_{j=1}^r h_j(z(t)) K_j \hat{x}(t) \quad (7.17)$$

where K_j is the controller gain for $j = 1, \dots, r$.

Let the state estimation error be

$$e(t) = x(t) - \hat{x}(t). \quad (7.18)$$

Using the control law (7.17) and state estimation error (7.18), the closed-loop system is represented as the augmented system:

$$\dot{\tilde{x}} = \sum_{i=1}^r \sum_{j=1}^r h_i(z(t)) h_j(z(t)) \left(A_{ij} \tilde{x} + E w(t) + \Delta \tilde{F} + \Delta \tilde{G} + \Delta \tilde{H}_i \right) \quad (7.19)$$

In the sequel, the following abbreviations are adopted:

$$\tilde{x} := [\hat{x}(t) \quad e(t)]^\top, \quad A_{ij} := \begin{bmatrix} A_i + B_i K_j & L_i C_j \\ 0 & A_i - L_i C_j \end{bmatrix}, \quad E := [0 \quad I]^\top,$$

$$\begin{aligned}\Delta\tilde{F} &:= [0 \quad \Delta F]^\top, \quad \Delta\tilde{G} := [0 \quad \Delta G]^\top, \\ \Delta\tilde{H}_i &:= \left[\sum_{i=1}^r h_i(z(t))L_i\Delta H \quad - \sum_{i=1}^r h_i(z(t))L_i\Delta H \right]^\top.\end{aligned}$$

The following assumptions are adopted for the approximation errors, for all trajectories $x(t)$ and $\hat{x}(t)$ in (7.19), (7.16), and (7.17), there exist bounding matrices ΔA , ΔB and ΔC such that for all $t \geq 0$

$$\|\Delta F(t)\| \leq \left\| \sum_{i=1}^r h_i \Delta A_i x(t) \right\| \quad (7.20)$$

$$\|\Delta G(t)\| \leq \left\| \sum_{j=1}^r \sum_{i=1}^r h_i h_j \Delta B_i K_j \hat{x}(t) \right\| \quad (7.21)$$

$$\|\Delta H(t)\| \leq \left\| \sum_{i=1}^r h_i \Delta C_i x(t) \right\| \quad (7.22)$$

where, for $i = 1, \dots, r$,

$$\begin{aligned}\{\Delta A_i = \delta_i \Delta A \mid |\delta_i| \leq 1\} \\ \{\Delta B_i = \eta_i \Delta B \mid |\eta_i| \leq 1\} \\ \{\Delta C_i = \gamma_i \Delta C \mid |\gamma_i| \leq 1\}\end{aligned} \quad (7.23)$$

According to these assumptions, we obtain for all $t \geq 0$

$$\begin{aligned}(\Delta\tilde{F}(t))^\top (\Delta\tilde{F}(t)) &= (\Delta F(t))^\top (\Delta F(t)) \\ &= \left(F(x(t)) - \sum_{i=1}^r h_i(z(t))A_i x(t) \right)^\top \left(F(x(t)) - \sum_{i=1}^r h_i(z(t))A_i x(t) \right) \\ &\leq \left(\sum_{i=1}^r h_i(z(t))\Delta A_i x(t) \right)^\top \left(\sum_{i=1}^r h_i(z(t))\Delta A_i x(t) \right) \\ &= \left(\sum_{i=1}^r h_i(z(t))\delta_i \Delta A x(t) \right)^\top \left(\sum_{i=1}^r h_i(z(t))\delta_i \Delta A x(t) \right) \\ &\leq (\Delta A x(t))^\top (\Delta A x(t)). \\ &\leq (\Delta\tilde{A}\tilde{x}(t))^\top (\Delta\tilde{A}\tilde{x}(t))\end{aligned} \quad (7.24)$$

with $\Delta\tilde{A} := [\Delta A \quad \Delta A]$.

Furthermore,

$$\begin{aligned}
(\Delta\tilde{G}(t))^\top(\Delta\tilde{G}(t)) &= (\Delta G(t))^\top(\Delta G(t)) \\
&= \left((G(x(t)) - \sum_{i=1}^r h_i(z(t))B_i)u(t) \right)^\top \left((G(x(t)) - \sum_{i=1}^r h_i(z(t))B_i)u(t) \right) \\
&\leq \left(\sum_{j=1}^r \sum_{i=1}^r h_i h_j \Delta B_i K_j \hat{x}(t) \right)^\top \left(\sum_{j=1}^r \sum_{i=1}^r h_i h_j \Delta B_i K_j \hat{x}(t) \right) \\
&= \left(\sum_{j=1}^r \sum_{i=1}^r h_i h_j \eta_i \Delta B K_j \hat{x}(t) \right)^\top \left(\sum_{j=1}^r \sum_{i=1}^r h_i h_j \eta_i \Delta B K_j \hat{x}(t) \right) \\
&\leq \left(\sum_{j=1}^r h_j \Delta B K_j \hat{x}(t) \right)^\top \left(\sum_{j=1}^r h_j \Delta B K_j \hat{x}(t) \right) \\
&\leq \left(\sum_{j=1}^r h_j \Delta \tilde{B}_j \tilde{x}(t) \right)^\top \left(\sum_{j=1}^r h_j \Delta \tilde{B}_j \tilde{x}(t) \right) \tag{7.25}
\end{aligned}$$

with $\Delta \tilde{B}_j := [\Delta B K_j \quad 0]$.

Similarly,

$$\begin{aligned}
(\Delta\tilde{H}(t))^\top(\Delta\tilde{H}(t)) &= 2 \left(\sum_{i=1}^r h_i L_i \Delta H \right)^\top \left(\sum_{i=1}^r h_i L_i \Delta H \right) \\
&\leq 2 \left(\sum_{i=1}^r h_i L_i \Delta C x(t) \right)^\top \left(\sum_{i=1}^r h_i L_i \Delta C x(t) \right) \\
&\leq 2 \left(\sum_{i=1}^r h_i \Delta \tilde{C}_i \tilde{x}(t) \right)^\top \left(\sum_{i=1}^r h_i \Delta \tilde{C}_i \tilde{x}(t) \right) \tag{7.26}
\end{aligned}$$

with $\Delta \tilde{C}_i := [L_i \Delta C \quad L_i \Delta C]$.

Given $\rho > 0$, the objective is to design an observer-based output feedback control (7.17), which ensures that the \mathcal{L}_2 gain from w to \tilde{x} is upper bounded with small value ρ . According to Proposition 7.2.1, the system has a finite \mathcal{L}_2 gain from w to \tilde{x} if there exists a storage function $V(\tilde{x})$ associated with a quadratic supply rate $s(w(t), \tilde{x}(t))$ is a

positive definite function, such that

$$\int_0^t s(w(t), \tilde{x}(t)) dt \geq V(\tilde{x}(t)) - V(\tilde{x}(0)) \quad (7.27)$$

holds for all trajectories (w, \tilde{x}) generated by the uncertain system (7.19) and for all $t \geq 0$.

Let V be a storage function of the closed-loop system (7.19) that is robustly dissipative with respect to the supply function $s(w, \tilde{x}) := \rho^2 w^\top w - \tilde{x}^\top Q \tilde{x}$, $Q \succ 0$, then based on Definition 7.2.1 we obtain

$$\int_0^T \|\tilde{x}(t)\|_2^2 dt - \rho^2 \|w(t)\|_2^2 dt \leq 0 \quad \forall w \in \mathcal{L}_2(0, T) \quad \forall T \geq 0, \quad (7.28)$$

therefore, it follows that the following inequality holds for all uncertainties ΔF , ΔG , and ΔH .

$$\sup_{T>0} \sup_{0 \neq w \in \mathcal{L}_2} \frac{\int_0^T \|\tilde{x}(t)\|_2^2 dt}{\int_0^T \|w(t)\|_2^2 dt} \leq \rho^2.$$

Theorem 7.4.1. *Suppose that for $k = 1, \dots, r$, $\|\dot{h}_k\| = \left\| \frac{dh_k}{dz} \frac{dz}{dt} \right\| \leq \mu_k$, $\mu_k > 0$ and $\rho > 0$. If there exist symmetric positive definite matrices P_k , which satisfy the matrix inequalities:*

$$\begin{aligned} A_{ij}^\top P_k + P_k A_{ij} + \hat{P} + P_k \left(\frac{EE^\top}{\rho^2} + 3I \right) P_k + \Delta \tilde{A}^\top \Delta \tilde{A} \\ + \Delta \tilde{B}_j^\top \Delta \tilde{B}_j + 2\Delta \tilde{C}_i^\top \Delta \tilde{C}_i + Q \prec 0, \end{aligned} \quad (7.29)$$

for all i, j such that $h_i h_j h_k \neq 0$, with $\hat{P} = \sum_{k=1}^r \mu_k (P_k + Y)$, and where μ_k are scalars, Y is a symmetric arbitrary matrix, then the state observer (7.16) and the control law (7.17) are well defined and the corresponding closed loop system (7.19) has guaranteed robust \mathcal{L}_2 gain performance as specified in (7.28).

Proof. Consider the candidate storage function:

$$V(\tilde{x}(t)) = \sum_{k=1}^r h_k(z(t)) \tilde{x}^\top(t) P_k \tilde{x}(t), \quad (7.30)$$

The time derivative $\frac{d}{dt} V(\tilde{x}(t))$ along the system trajectories is given by:

$$\begin{aligned} \dot{V}(\tilde{x}(t)) &= \sum_{k=1}^r h_k \dot{\tilde{x}}^\top(t) P_k \tilde{x}(t) + \sum_{k=1}^r h_k \tilde{x}^\top(t) P_k \dot{\tilde{x}}(t) \\ &+ \sum_{k=1}^r \dot{h}_k \tilde{x}^\top(t) P_k \tilde{x}(t). \end{aligned}$$

Furthermore, using (7.19) we have

$$\begin{aligned}
\dot{V}(\tilde{x}(t)) &= \sum_{k=1}^r \sum_{i=1}^r \sum_{j=1}^r h_i h_j h_k (\tilde{x}^\top(t) A_{ij}^\top P_k \tilde{x}(t) + \tilde{x}^\top(t) P_k A_{ij} \tilde{x}(t) \\
&\quad + w^\top(t) E^\top P_k \tilde{x}(t) + \tilde{x}^\top(t) P_k E w(t)) + \sum_{k=1}^r \dot{h}_k \tilde{x}^\top(t) P_k \tilde{x}(t) \\
&\quad + \Delta \tilde{F}^\top P_k \tilde{x}(t) + \tilde{x}^\top(t) P_k \Delta \tilde{F} + \Delta \tilde{G}^\top P_k \tilde{x}(t) + \tilde{x}^\top(t) P_k \Delta \tilde{G} \\
&\quad + \Delta \tilde{H}^\top P_k \tilde{x}(t) + \tilde{x}^\top(t) P_k \Delta \tilde{H}. \\
\dot{V}(\tilde{x}(t)) &= \sum_{k=1}^r \sum_{i=1}^r \sum_{j=1}^r h_k h_i h_j \tilde{x}^\top (A_{ij}^\top P_k + P_k A_{ij}) \tilde{x} \\
&\quad - (\tilde{x} P_k - \Delta \tilde{F})^\top (\tilde{x} P_k - \Delta \tilde{F}) - (\tilde{x} P_k - \Delta \tilde{G})^\top (\tilde{x} P_k - \Delta \tilde{G}) \\
&\quad - (\tilde{x} P_k - \Delta \tilde{H})^\top (\tilde{x} P_k - \Delta \tilde{H}) + \Delta \tilde{F}^\top \Delta \tilde{F} + \Delta \tilde{G}^\top \Delta \tilde{G} \\
&\quad - \left(\frac{1}{\rho} \tilde{x} E^\top P_k - \rho w\right)^\top \left(\frac{1}{\rho} \tilde{x} E^\top P_k - \rho w\right) + \rho^2 w^\top w \\
&\quad + \tilde{x}^\top P_k \left(3 + \frac{E E^\top}{\rho^2}\right) P_k \tilde{x} + \sum_{k=1}^r \dot{h}_k \tilde{x}^\top(t) P_k \tilde{x}(t), \tag{7.31}
\end{aligned}$$

Since $\sum_{k=1}^r h_k = 1$, hence, $\sum_{k=1}^r \dot{h}_k = 0$, it follows that $\sum_{k=1}^r \dot{h}_k Y = 0$ for arbitrary matrix Y . Adding $\sum_{k=1}^r \dot{h}_k Y$ to (7.31) with $Y \in \mathbb{R}^{2n \times 2n}$, and using the inequality $|\dot{h}_k| \leq \mu_k$ and the assumptions (7.24), (7.25) and (7.26) implies

$$\begin{aligned}
\dot{V}(\tilde{x}(t)) &\leq \sum_{k=1}^r \sum_{i=1}^r \sum_{j=1}^r h_k h_i h_j \tilde{x}^\top (A_{ij}^\top P_k + P_k A_{ij} + \Delta \tilde{A}^\top \Delta \tilde{A} \\
&\quad + \Delta \tilde{B}_j^\top \Delta \tilde{B}_j + \hat{P} + P_k \left(\frac{E E^\top}{\rho^2} + 3I\right) P_k + 2\Delta \tilde{C}_i^\top \Delta \tilde{C}_i) \tilde{x} \\
&\quad + \rho^2 w^\top w \tag{7.32}
\end{aligned}$$

with the abbreviation $\hat{P} := \sum_{k=1}^r \mu_k (P_k + Y)$. Applying the properties of $h_i(z(t))$ and (7.29), we can write (7.32) as

$$\dot{V}(\tilde{x}(t)) \leq \tilde{x}^\top(t) (-Q) \tilde{x}(t) + \rho^2 w^\top(t) w(t).$$

Integrating both sides from 0 to T we obtain,

$$\int_0^T \tilde{x}^\top(t) Q \tilde{x}(t) dt \leq \tilde{x}^\top(0) \sum_{k=1}^r h_k(z) P_k \tilde{x}(0) + \rho^2 \int_0^T w^\top(t) w(t) dt$$

Therefore, the robust \mathcal{L}_2 gain performance is achieved with a prescribed ρ . \square

Theorem 7.4.2. *Suppose that for $k = 1, \dots, r$, and for all $t \geq 0$ $\|\dot{h}_k\| \leq \mu_k$, $\mu_k > 0$. The closed loop system (7.19) is quadratically stable, if there exist symmetric positive definite matrices P_k that satisfy the matrix inequalities (7.29).*

Proof. if we set $w(t) = 0$, from (7.32) and (7.29) we obtain

$$\dot{V}(\tilde{x}(t)) < -\tilde{x}^\top(t)Q\tilde{x}(t) < 0.$$

Therefore, the augmented system (7.19) is quadratically stable. \square

7.5 LMI formulation for control synthesis

Over the last decades, linear matrix inequality (LMI) problems have received significant attention [73, 74]. LMI techniques are now considered as a powerful framework for formulating and solving control problems. The main advantage of these LMI techniques is that many complicated control problems can be efficiently solved. The interior-point method, which is developed in [74], is an extremely efficient tool to solve LMI problems in practice. For systems and control, the importance of LMI optimization stems from the fact that a wide variety of control problems can be recast as LMI problems [73], which are, in fact, convex optimization problem. In this section, the robust \mathcal{L}_2 conditions, derived in Theorem 7.3.2 and Theorem 7.4.1, are formulated as a set of LMIs.

7.5.1 State feedback controller synthesis

The inequalities (7.14) are not a linear in P_k and K_j as variables. Therefore, a transformation method is proposed to reformulate (7.14) as a feasibility problem of a set of LMIs. The following Theorem shows that the controller synthesis can be formulated as a feasibility problem with P_k and K_j as variables.

Theorem 7.5.1. *Given $\mu_k > 0$ and $\rho > 0$, consider the following linear matrix inequalities in the variables P_k, K_j :*

$$\begin{bmatrix} G_{ijk} & (*) & (*) & (*) \\ \Delta AP_k & -I & 0 & 0 \\ P_k & 0 & -Q^{-1} & 0 \\ \Delta BK_j & 0 & 0 & -I \end{bmatrix} \prec 0 \quad (7.33)$$

with $G_{ijk} := (A_i P_k + B_i K_j)^\top + (A_i P_k + B_i K_j) - \hat{P} + (\frac{1}{\rho^2} + 2)I$ for $i, j, k = 1, \dots, L$,

and $\hat{P} = \sum_{k=1}^L \mu_k P_k$.

Then for any feasible solution (P_k, K_j) , $P_k \succ 0$ and (7.33), the control law (7.17) is well defined and the corresponding closed-loop system (7.5) has guaranteed \mathcal{L}_2 gain performance as specified in (7.12).

Proof. First pre- and post-multiplying (7.14) by P_n we get

$$\begin{aligned} P_n A_{ij}^\top + A_{ij} P_n - \hat{P} + \left(\frac{1}{\rho^2} + 2\right)I + P_n \Delta A^\top \Delta A P_n + (K_j \Delta B)^\top (K_j \Delta B) \\ + P_n Q P_n \prec 0 \end{aligned} \quad (7.34)$$

then substituting $A_{ij} = A_i + B_i K_j P_n^{-1}$ and $P_n = \sum_{k=1}^L h_k P_k$ in (7.34) and using the Schur complement, we obtain the LMI (7.33). \square

The inequalities (7.33) allows control synthesis since (7.33) is an LMI, which can be solved using the LMI optimization toolbox in Matlab software package to determine P_k and the controller.

Therefore, the \mathcal{L}_2 gain control problem is formulated as the following minimization problem:

$$\begin{aligned} \min_{P_k, K_j, \rho} \rho^2 \\ \text{subject to } P_k > 0, k = 1, \dots, L, \text{ and (7.33)} \end{aligned} \quad (7.35)$$

This problem is solved by decreasing the value of ρ until the LMIs (7.33) are infeasible. Note that (7.29) is not an LMI in the variables P_k , L_i and K_j . Therefore, a transformation method is proposed to reformulate (7.29) as a feasibility problem of a set of LMIs.

7.5.2 Output feedback controller synthesis

For output feedback case, it is not straightforward to formulate the nonlinear matrix inequalities (7.29) as an LMIs. Here, we present a method to formulate (7.29) as an LMI conditions. The following Theorem summarizes the controller and observer synthesis.

Theorem 7.5.2. *Given $\mu_k > 0$, $\rho > 0$ and a positive scalar $\chi > 0$, consider the following linear matrix inequalities in the variables P_k, L_i, K_j :*

$$\begin{bmatrix} G_k & (*) & (*) & (*) & (*) \\ A_{ij} + \chi I & -\chi I & 0 & 0 & 0 \\ P_k & 0 & -\left(\frac{EE^\top}{\rho^2} + 3I + \chi I\right)^{-1} & 0 & 0 \\ \Delta \tilde{B}_j & 0 & 0 & -I & 0 \\ \Delta \tilde{B}_i & 0 & 0 & 0 & -0.5I \end{bmatrix} \prec 0 \quad (7.36)$$

with $G_k := -2\chi P_k + \hat{P} + \Delta \tilde{A}^\top \Delta \tilde{A} + Q$ for $i, j, k = 1, \dots, r$, and $\hat{P} = \sum_{k=1}^r \mu_k (P_k + Y)$.

Then for any feasible solution (P_k, L_i, K_j) , $P_k \succ 0$ and (7.36), the control law (7.17) and the state observer (7.16) are well defined and the corresponding closed loop system (7.19) has guaranteed robust \mathcal{L}_2 gain ρ .

Proof. Suppose there exists a scalar positive value $\chi > 0$, the matrix inequality (7.29) can be written as

$$\begin{aligned} & \chi P_k P_k + \frac{1}{\chi} (A_{ij} + \chi I)^\top (A_{ij} + \chi I) - 2\chi P_k \\ & - (A_{ij} - \chi P_k + \chi I)^\top \chi^{-1} (A_{ij} - \chi P_k + \chi I) \\ & + \hat{P} + P_k \left(\frac{EE^\top}{\rho^2} + 3I \right) P_k + \Delta \tilde{A}^\top \Delta \tilde{A} + \Delta \tilde{B}_j^\top \Delta \tilde{B}_j \\ & + 2\Delta \tilde{C}_i^\top \Delta \tilde{C}_i + Q \prec 0, \end{aligned} \quad (7.37)$$

The following matrix inequality implies (7.37)

$$\begin{aligned} & \frac{1}{\chi} (A_{ij} + \chi I)^\top (A_{ij} + \chi I) - 2\chi P_k + \hat{P} + P_k \left(\frac{EE^\top}{\rho^2} + 3I + \chi I \right) P_k \\ & + \Delta \tilde{A}^\top \Delta \tilde{A} + \Delta \tilde{B}_j^\top \Delta \tilde{B}_j + 2\Delta \tilde{C}_i^\top \Delta \tilde{C}_i + Q \prec 0, \end{aligned} \quad (7.38)$$

Using the Schur complement, we obtain the following LMI

$$\begin{bmatrix} G_k & (*) & (*) & (*) & (*) \\ A_{ij} + \chi I & -\chi I & 0 & 0 & 0 \\ P_k & 0 & -\left(\frac{EE^\top}{\rho^2} + 3I + \chi I\right)^{-1} & 0 & 0 \\ \Delta \tilde{B}_j & 0 & 0 & -I & 0 \\ \Delta \tilde{B}_i & 0 & 0 & 0 & -0.5I \end{bmatrix} \prec 0 \quad (7.39)$$

using the abbreviation $G_k := -2\chi P_k + \hat{P} + \Delta \tilde{A}^\top \Delta \tilde{A} + Q$, for $i, j, k = 1, \dots, r$ we obtain (7.36). \square

Unlike (7.29), (7.36) can be used for control synthesis. The inequalities (7.36) are now an LMI with P_k , L_i and K_j as variables, which can be efficiently solved using an LMI optimization solver to determine the observer and controller gains. Similar to the state feedback design, the \mathcal{L}_2 gain control problem is formulated as the minimization problem:

$$\min_{P_k, K_j, L_i, \rho} \rho^2 \quad (7.40)$$

subject to $P_k > 0$, $k = 1, \dots, r$, and (7.36)

This problem is solved by decreasing the value of ρ until the LMIs (7.36) are infeasible.

7.6 Simulation example

In this section, we use a benchmark example to illustrate the proposed control approach and compare our \mathcal{L}_∞ controller design with the conventional \mathcal{L}_∞ design [86]. The con-

trol problem of balancing an inverted pendulum on a cart is considered. For this example, the state equations of the inverted pendulum are given by

$$\begin{aligned} \dot{x}_1 &= x_2, \\ \dot{x}_2 &= \frac{F_1(x, u)}{(M + m)(J + ml^2) - (ml \cos x_1)^2} + d_1, \\ \dot{x}_3 &= x_4, \\ \dot{x}_4 &= \frac{F_2(x, u)}{(M + m)(J + ml^2) - (ml \cos x_1)^2} + d_2 \end{aligned} \quad (7.41)$$

where

$$\begin{aligned} F_1(x, u) &= -f_1(M + m)x_2 - (mlx_2)^2 \sin x_1 \cos x_1 + f_o mlx_4 \cos x_1 \\ &\quad + (m + M)mgl \sin x_1 - ml \cos x_1 u, \\ F_2(x, u) &= -f_1 mlx_2 \cos x_1 - (J + ml^2)mlx_2^2 \sin x_1 - f_o(J + ml^2)x_4 \\ &\quad + m^2 gl^2 \sin x_1 \cos x_1 + (J + ml^2)u, \end{aligned}$$

x_1 is the angle of the pendulum from the vertical [rad], x_2 represents the angular velocity [rad/s], x_3 [m], x_4 [m/s] denote the position and the velocity of the cart respectively, m [kg.], M [kg.] are the mass of the pendulum and the cart respectively, f_o [Ns/m] the friction factor, J [kg m²] denotes the moment of inertia of the pendulum around its center of mass, l [m] is the length of the pendulum from the center of mass of the pendulum to the shaft axis, u [N] is the force applied to the cart and d_1 and d_2 are external disturbances. The system parameters are summarized in table 7.1. To implement

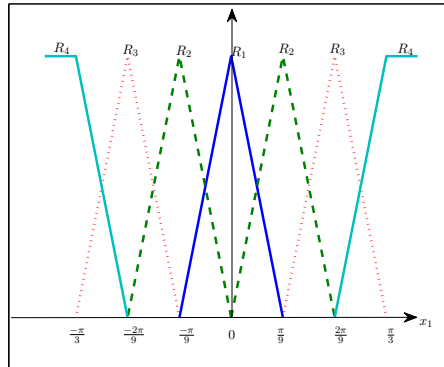


Figure 7.1: The weighting functions $h_i(x_1(t))$

the proposed approach, the nonlinear system (7.41) is approximated with a T-S model. The Takagi-Sugeno model which approximates the nonlinear system (7.41) can be represented using the following set of linearized models [86]:

R1 If $-\frac{\pi}{9} \leq x_1 \leq \frac{\pi}{9}$
then $\dot{x} = A_1x + B_1u + w, y = C_1x$

R2 If $0 \leq |x_1| \leq \frac{2\pi}{9}$
then $\dot{x} = A_2x + B_2u + w, y = C_2x$

R3 If $\frac{\pi}{9} \leq |x_1| \leq \frac{\pi}{3}$
then $\dot{x} = A_3x + B_3u + w, y = C_3x$

R4 If $|x_1| \geq \frac{\pi}{3}$
then $\dot{x} = A_4x + B_4u + w, y = C_4x$

where

$$A_1 = \begin{bmatrix} 0 & 1 & 0 & 0 \\ 28.0262 & -0.2224 & 0 & 1.8692 \\ 0 & 0 & 0 & 1 \\ -0.1649 & 0.0013 & 0 & -0.6646 \end{bmatrix},$$

$$A_2 = \begin{bmatrix} 0 & 1 & 0 & 0 \\ 27.4065 & -0.222 & 0 & 1.7530 \\ 0 & 0 & 0 & 1 \\ -0.1515 & 0.0012 & 0 & -0.6633 \end{bmatrix},$$

$$A_3 = \begin{bmatrix} 0 & 1 & 0 & 0 \\ 25.6263 & -0.2209 & 0 & 1.422 \\ 0 & 0 & 0 & 1 \\ -0.1155 & 0.001 & 0 & -0.66 \end{bmatrix},$$

$$A_4 = \begin{bmatrix} 0 & 1 & 0 & 0 \\ 22.8887 & -0.2197 & 0 & 0.9229 \\ 0 & 0 & 0 & 1 \\ -0.066 & 0.0006 & 0 & -0.6563 \end{bmatrix},$$

$$B_1 = \begin{bmatrix} 0 \\ -0.1869 \\ 0 \\ 0.0668 \end{bmatrix}, B_2 = \begin{bmatrix} 0 \\ -0.1753 \\ 0 \\ 0.0663 \end{bmatrix}, B_3 = \begin{bmatrix} 0 \\ -0.1422 \\ 0 \\ 0.066 \end{bmatrix}, B_4 = \begin{bmatrix} 0 \\ -0.0923 \\ 0 \\ 0.0656 \end{bmatrix},$$

$$C_i = \begin{bmatrix} 1 & 0 & 0 & 0 \\ 0 & 0 & 1 & 0 \end{bmatrix} \text{ for } i = 1, \dots, 4$$

$$w = [0 \quad d_1 \quad 0 \quad d_2]^\top.$$

and the bounding matrices are chosen as

$$\Delta A = \begin{bmatrix} 0 & 0.14 & 0 & 0.2 \\ 0.3204 & 0.31 & 0.2 & 0.129 \\ 0 & 0 & 0 & 0.14 \\ 0.09 & 0.1 & 0 & 0.092 \end{bmatrix}$$

$$\Delta B = \begin{bmatrix} 0 \\ 0.0025 \\ 0 \\ 0.0026 \end{bmatrix}$$

$$\delta_i = I, \eta_i = I \text{ for } i = 1, \dots, 4.$$

Figure 7.1 shows the normalized weighting functions $h_i(z(t))$ for the triggering vari-

m	0.3 [kg]	M	15 [kg]
l	0.3 [m]	J	0.005 [kg m ²]
f_o	10 [Ns/m]	f_1	0.007 [Ns/rad]

Table 7.1: The inverted pendulum parameters.

able $z(t) = x_1(t)$. Select $Q = 0.05 I$ and $\mu_k = 0.5$ for $k = 1, \dots, L$.

7.6.1 State feedback control

Using Theorem 7.3.2, we obtain the optimal $\rho = 0.68$ after several iterations using the LMI optimization toolbox in Matlab. In this case, the solution of the optimization problem is given as

$$P_1 = \begin{bmatrix} 1.2339 & -2.9085 & -0.1802 & -1.3187 \\ -2.9085 & 31.6187 & 1.2549 & -19.1815 \\ 0 - 0.1802 & 1.2549 & 16.3268 & -5.9421 \\ -1.3187 & -19.1815 & -5.9421 & 28.3182 \end{bmatrix},$$

$$P_2 = \begin{bmatrix} 1.1495 & -3.0411 & -0.1807 & -1.1872 \\ -3.0411 & 26.4152 & 0.7727 & -16.3091 \\ -0.1807 & 0.7727 & 16.0449 & -5.5627 \\ -1.1872 & -16.3091 & -5.5627 & 26.9390 \end{bmatrix},$$

$$\begin{aligned}
P_3 &= \begin{bmatrix} 1.0739 & -3.6134 & -0.3919 & -1.4684 \\ -3.6134 & 34.5500 & 2.6357 & -18.9975 \\ -0.3919 & 2.6357 & 5.4647 & -6.6969 \\ -1.4684 & -18.9975 & -6.6969 & 30.0676 \end{bmatrix}, \\
P_4 &= \begin{bmatrix} 1.4046 & -7.9869 & 0.1702 & 0.1131 \\ -7.9869 & 75.6924 & 0.1587 & -38.8957 \\ 0.1702 & 0.1587 & 17.2051 & -7.6467 \\ 0.1131 & -38.8957 & -7.6467 & 50.6451 \end{bmatrix}, \\
K_1 &= [309.4672 \quad -376.9036 \quad -51.9365 \quad -315.7050], \\
K_2 &= [284.3237 \quad -470.1439 \quad -78.8475 \quad -229.3938], \\
K_3 &= [352.8398 \quad -392.6765 \quad -57.3666 \quad -717.5650], \\
K_4 &= 10^3 \times [0.4246 \quad 1.5181 \quad -0.0283 \quad -2.2810].
\end{aligned}$$

Figures 7.2-7.3 present the state trajectories $x(t)$ including the external disturbance $w(t)$ with initial condition $x(0) = [\frac{\pi}{4} \quad 0 \quad 0.1 \quad 0]^\top$. A periodic square wave with amplitude ± 1 and period 0.25 sec. is used as external disturbance $w(t)$ in the simulation. The simulation results indicate that the proposed approach can efficiently balance the inverted-pendulum in the presence of external disturbances and the desired performance is achieved.

7.6.2 Output feedback control

After several iterations using the LMI optimization toolbox in Matlab, we found by Theorem 7.5.2 that the optimal $\rho = 0.6$. The solution of the optimization problem in terms of the controller (7.17) and observer (7.16) gains are given as

$$\begin{aligned}
K_1 &= 10^3 \times [1.2158 \quad 0.0727 \quad -0.0255 \quad 0.0635] \\
K_2 &= 10^3 \times [1.2573 \quad 0.0849 \quad 0.0538 \quad 0.0677] \\
K_3 &= 10^3 \times [1.3507 \quad 0.0879 \quad -0.0578 \quad 0.0419] \\
K_4 &= 10^3 \times [1.4044 \quad 0.1097 \quad 0.0495 \quad 0.0173] \\
L_1 &= \begin{bmatrix} 10.1944 & 0.0405 \\ 141.4460 & -0.1010 \\ 0.2858 & 10.1847 \\ 0.2480 & 0.2957 \end{bmatrix}, \quad L_2 = \begin{bmatrix} 10.4638 & -0.0820 \\ 139.1894 & 0.2185 \\ 0.0994 & 9.7396 \\ 0.6817 & -0.4997 \end{bmatrix} \\
L_3 &= \begin{bmatrix} 10.1546 & 0.1100 \\ 128.4257 & -0.0273 \\ -0.7806 & 10.3984 \\ 0.7399 & 0.7642 \end{bmatrix}, \quad L_4 = \begin{bmatrix} 6.2299 & -0.0786 \\ 95.1523 & -0.0575 \\ -1.0065 & 9.6462 \\ -18.7628 & -0.6792 \end{bmatrix}
\end{aligned}$$

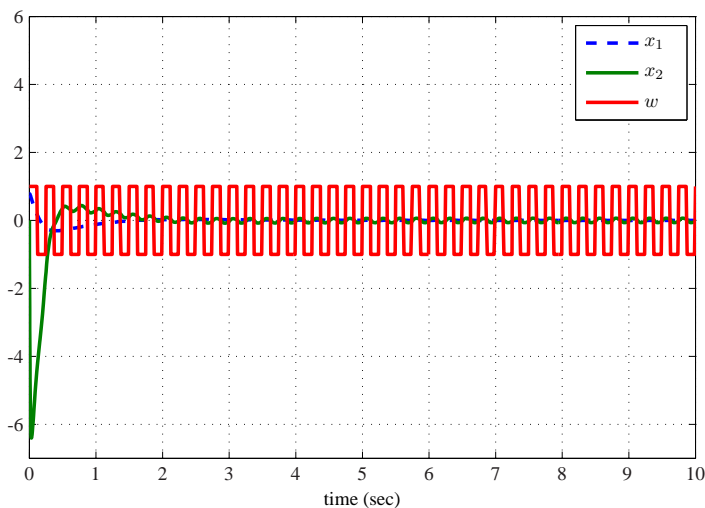


Figure 7.2: The trajectories of the states x_1 (dashed line), x_2 (solid line) and external disturbance w (solid line)

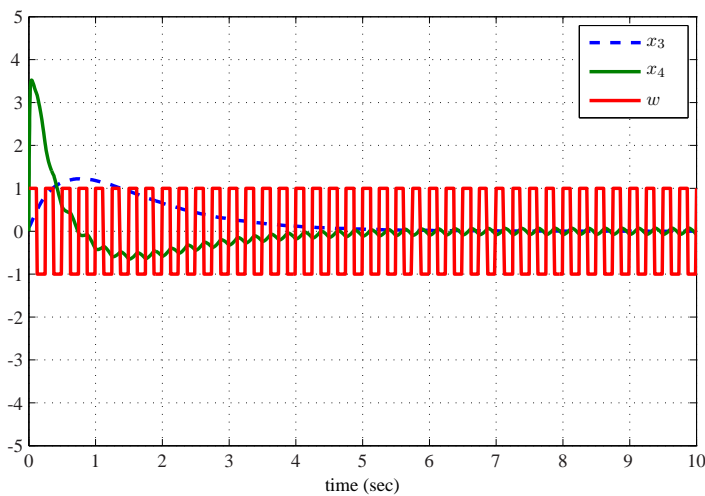


Figure 7.3: The trajectories of the states x_3 (dashed line), x_4 (solid line) and external disturbance w (solid line)

Figure 7.4 presents the output trajectories $y(t)$ including the external disturbance $d(t)$ with initial condition $[x(0) \ \hat{x}(0)]^\top = [\frac{\pi}{4} \ 0 \ 0.5 \ 0 \ 0 \ 0 \ 0]^\top$. A periodic square wave with amplitude ± 0.5 and period 0.25 sec is used as external disturbance $d(t)$ in the simulation. Figures 7.5-7.6 compare the trajectories of the system states and the estimated states (including the external disturbance $w(t)$). All of these state variables converge to zero. This reveals that the closed-loop system is a stable system. The observer estimation errors are depicted in Fig. 7.7. The simulation results show that the observer-based \mathcal{L}_2 controller can balance the inverted pendulum with relatively large external disturbances and that the desired performance can be achieved. Moreover, the controller is capable of damping the initial observation error for the given initial conditions.

Using the \mathcal{L}_2 conditions based on the conventional single quadratic Lyapunov function $V(x) = x^\top Px$ [86], we could not find any feasible solution for the given example. We found that it is only possible to find a feasible solution for the stability conditions given in [86], if the uncertain matrices, ΔA , ΔB , ΔC , are more than 10 times smaller than the one used in our example.

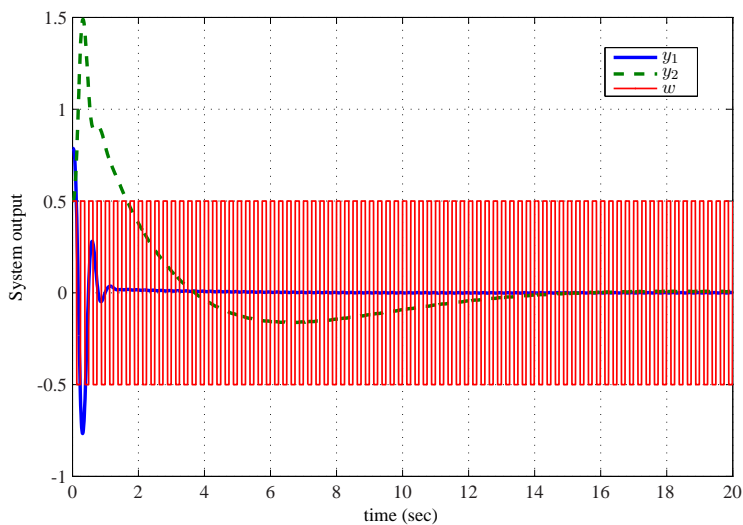


Figure 7.4: The trajectories of the outputs y_1 and y_2 with the presence of the external disturbance w .

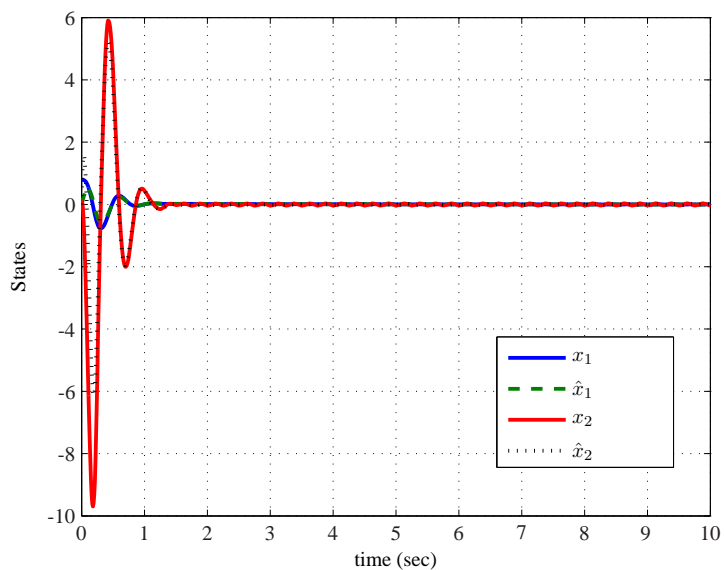


Figure 7.5: The trajectories of the states x_1 and x_2 and the estimated states \hat{x}_1 and \hat{x}_2 .

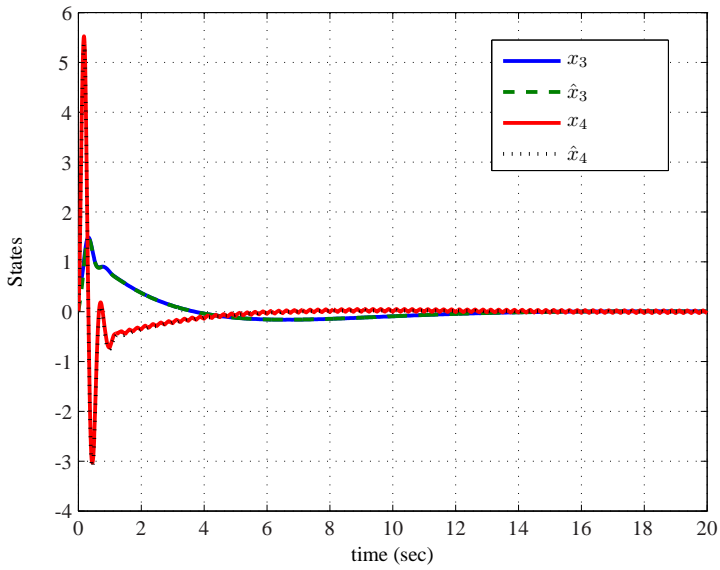


Figure 7.6: The trajectories of the states x_3 and x_4 and the estimated states \hat{x}_3 and \hat{x}_4 .

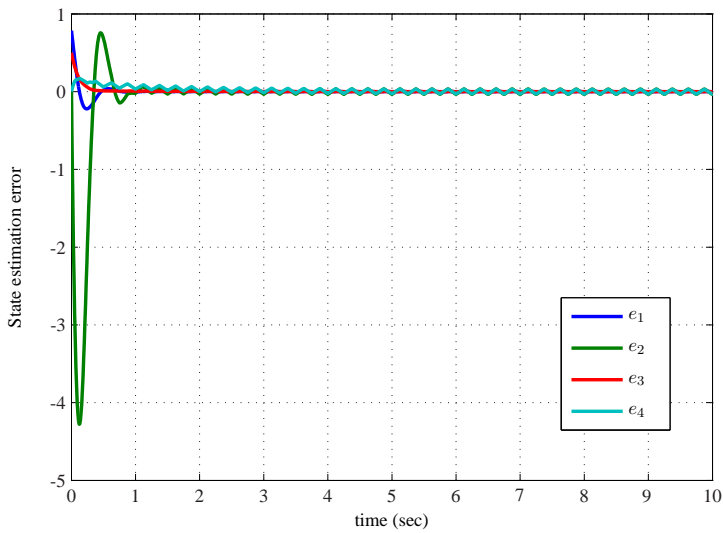


Figure 7.7: The observer estimation errors

7.7 Robust control of professional laser printing system

In this section, we present the implementation of the robust control scheme to the printing system and the comparison between the performance of both the proposed robust control scheme and the PI controller. To have a fair comparison, the PI controller is a well tuned industrial controller.

Given the knowledge of the paper mass m and the belt speed v , the printing system dynamics are approximated with a T-S model. The T-S model which approximates the printing system (5.1) is represented using the following set of 9 linearized models,

$$\begin{aligned} \dot{x}(t) &= \sum_{i=1}^9 h_i(z(t)) (A_i x(t) + B_i u(t) + E d(t)), \\ y(t) &= \sum_{i=1}^9 h_i(z(t)) C_i x(t), \end{aligned} \tag{7.42}$$

in the following 9 regions R_i ,

$$R1 \quad m \leq 80 \text{ and } v \leq 60,$$

$$R2 \quad m \leq 80 \text{ and } 60 \leq v \leq 90,$$

$$R3 \quad m \leq 80 \text{ and } 90 \leq v \leq 120,$$

$$R4 \quad 80 \leq m \leq 140 \text{ and } v \leq 60,$$

$$R5 \quad 80 \leq m \leq 140 \text{ and } 60 \leq v \leq 90,$$

$$R6 \quad 80 \leq m \leq 140 \text{ and } 90 \leq v \leq 120,$$

$$R7 \quad 140 \leq m \leq 200 \text{ and } v \leq 60,$$

$$R8 \quad 140 \leq m \leq 200 \text{ and } 60 \leq v \leq 90,$$

$$R9 \quad 140 \leq m \leq 200 \text{ and } 90 \leq v \leq 120,$$

where $x(t) = [T_1 \ T_2 \ T_3 \ T_4]^\top$, $u(t) = \begin{bmatrix} P_{TTF}(t) \\ P_{pre}(t) \end{bmatrix}$, $d(t) = T_{env}(t)$ is the environment temperature, $y(t) = \begin{bmatrix} T_{TTF}(t) \\ T_{pre}(t) \end{bmatrix}$,

$$A_1 = \begin{bmatrix} -0.1302 & 0.0104 & 0.0450 & 0.0103 \\ 0 & -0.0054 & 0 & 0 \\ 0.0412 & 0 & -0.0450 & 0 \\ 0.0407 & 0 & 0 & -0.0103 \end{bmatrix},$$

$$A_2 = \begin{bmatrix} -0.1302 & 0.0093 & 0.0450 & 0.0103 \\ 0 & -0.0073 & 0 & 0 \\ 0.0412 & 0 & -0.0450 & 0 \\ 0.0407 & 0 & 0 & -0.0103 \end{bmatrix},$$

$$A_3 = \begin{bmatrix} -0.1302 & 0.0082 & 0.0450 & 0.0103 \\ 0 & -0.0086 & 0 & 0 \\ 0.0412 & 0 & -0.0450 & 0 \\ 0.0407 & 0 & 0 & -0.0103 \end{bmatrix},$$

$$A_4 = \begin{bmatrix} -0.1302 & 0.0087 & 0.0450 & 0.0103 \\ 0 & -0.0080 & 0 & 0 \\ 0.0412 & 0 & -0.0450 & 0 \\ 0.0407 & 0 & 0 & -0.0103 \end{bmatrix},$$

$$A_5 = \begin{bmatrix} -0.1302 & 0.0071 & 0.0450 & 0.0103 \\ 0 & -0.0098 & 0 & 0 \\ 0.0412 & 0 & -0.0450 & 0 \\ 0.0407 & 0 & 0 & -0.0103 \end{bmatrix},$$

$$A_6 = \begin{bmatrix} -0.1302 & 0.0060 & 0.0450 & 0.0103 \\ 0 & -0.0109 & 0 & 0 \\ 0.0412 & 0 & -0.0450 & 0 \\ 0.0407 & 0 & 0 & -0.0103 \end{bmatrix},$$

$$A_7 = \begin{bmatrix} -0.1302 & 0.0073 & 0.0450 & 0.0103 \\ 0 & -0.0096 & 0 & 0 \\ 0.0412 & 0 & -0.0450 & 0 \\ 0.0407 & 0 & 0 & -0.0103 \end{bmatrix},$$

$$A_8 = \begin{bmatrix} -0.1302 & 0.0057 & 0.0450 & 0.0103 \\ 0 & -0.0111 & 0 & 0 \\ 0.0412 & 0 & -0.0450 & 0 \\ 0.0407 & 0 & 0 & -0.0103 \end{bmatrix},$$

$$A_9 = \begin{bmatrix} -0.1302 & 0.0046 & 0.0450 & 0.0103 \\ 0 & -0.0121 & 0 & 0 \\ 0.0412 & 0 & -0.0450 & 0 \\ 0.0407 & 0 & 0 & -0.0103 \end{bmatrix},$$

$$B_i = \begin{bmatrix} 0.7 & 0 \\ 0 & 1 \\ 0 & 0 \\ 0 & 0 \end{bmatrix}, \text{ for } i = 1, \dots, 9$$

$$C_i = \begin{bmatrix} 0.0031 & 0 & 0 & 0 \\ 0 & 0.0008 & 0 & 0 \end{bmatrix} \text{ for } i = 1, \dots, 9$$

$$E = [0.0119 \quad 0.0435 \quad 0 \quad 0]^\top.$$

The bounding matrices are chosen as

$$\Delta A = \begin{bmatrix} 0.02 & 0.027 & 0 & 0.005 \\ 0 & 0.31 & 0 & 0 \\ 0.007 & 0 & 0.001 & 0 \\ 0.02 & 0 & 0 & 0.003 \end{bmatrix}$$

$$\Delta B = \begin{bmatrix} 0.015 & 0 \\ 0 & 0.015 \\ 0 & 0 \\ 0 & 0 \end{bmatrix}, \Delta C = 0$$

$$\delta_i = I, \eta_i = I \text{ for } i = 1, \dots, 9.$$

Figure 7.1 shows the normalized weighting functions $h_i(z(t))$ for the triggering variables $z(t) = \text{col}(m, v)$. We select $Q = 100 I$.

After several iterations using the LMI optimization toolbox in Matlab, we found from Theorem 7.5.2 that the optimal $\rho = 0.5$. As shown in Figure 7.8, the external disturbance $d(t)$ (environment temperature) is assumed to vary from 15 to 30 °C. The variation of the paper mass and the belt speed is depicted in Figure 7.9. To achieve a good printing quality, the T_{TTF} and T_{pre} should be kept at a certain desired set point. The T_{TTF} and T_{pre} are used to estimate the fusing temperature. Figure 7.10 shows the fusing temperature tracking error comparison. As shown, the tracking performance of the robust controller is better compared to the PI controller in the presence of the parameter variations and the external disturbance. Figure 7.11 shows the preheating temperature tracking of different temperature levels with paper mass variations. The simulation results show that the observer-based \mathcal{L}_2 controller has considerably improved the printing quality with relatively large external disturbances while the desired performance is still being achieved.

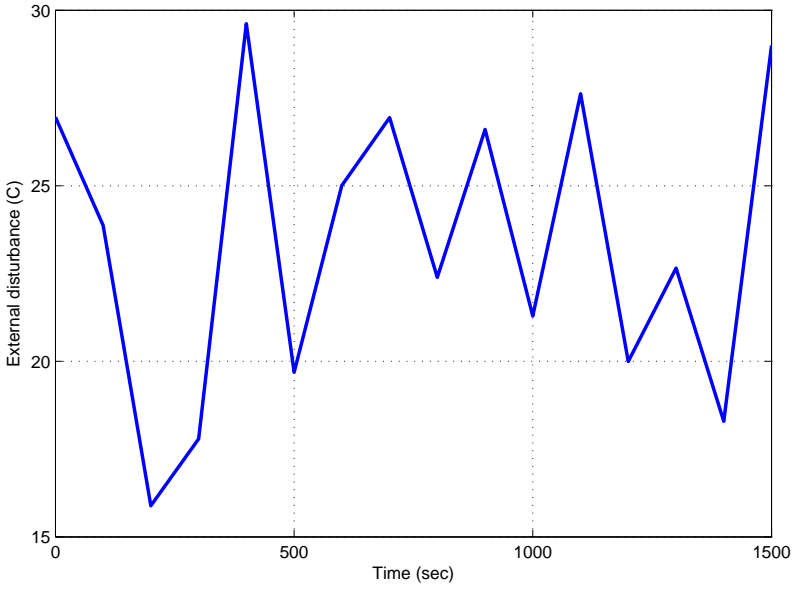


Figure 7.8: The external disturbance $d(t)$.

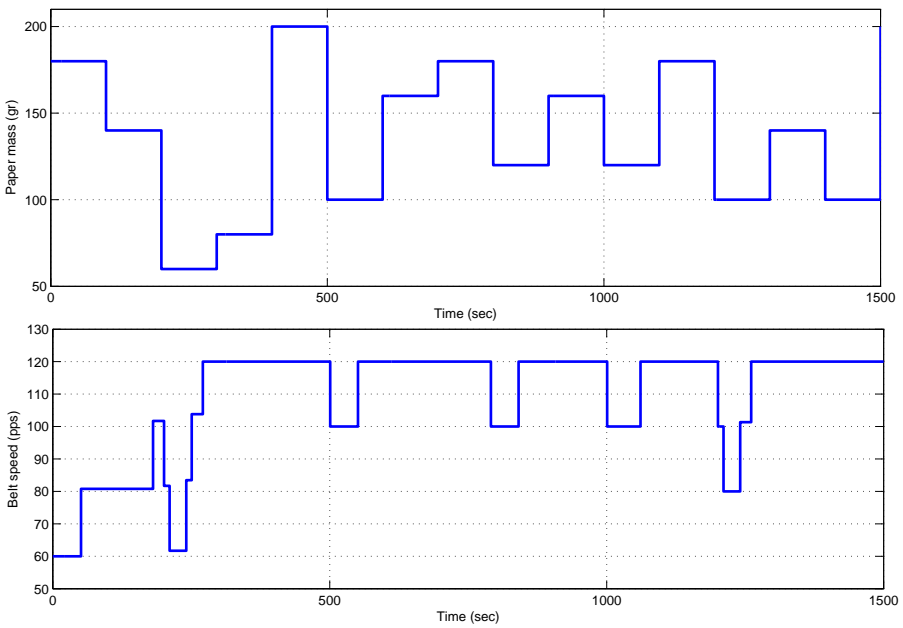


Figure 7.9: The variation of the paper mass and the belt speed.

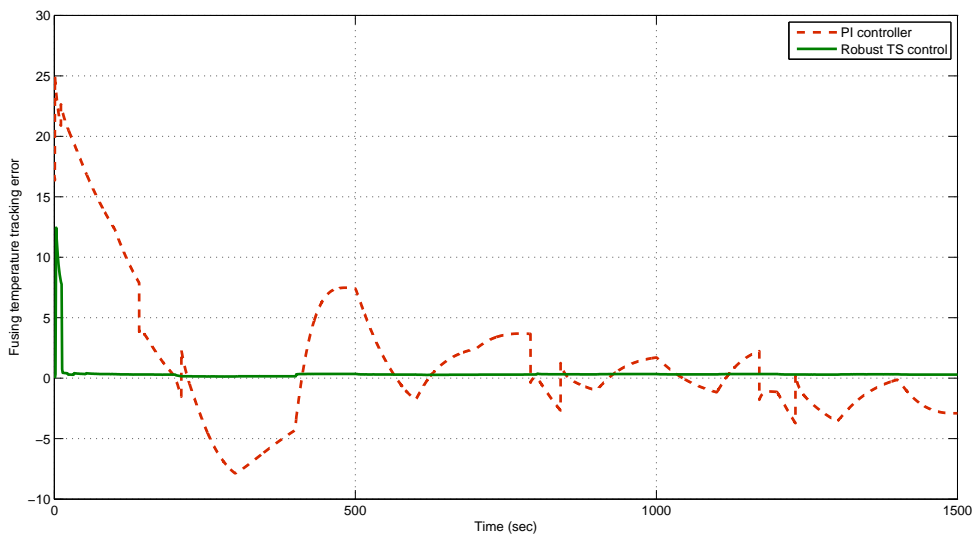


Figure 7.10: Fusing temperature tracking error.

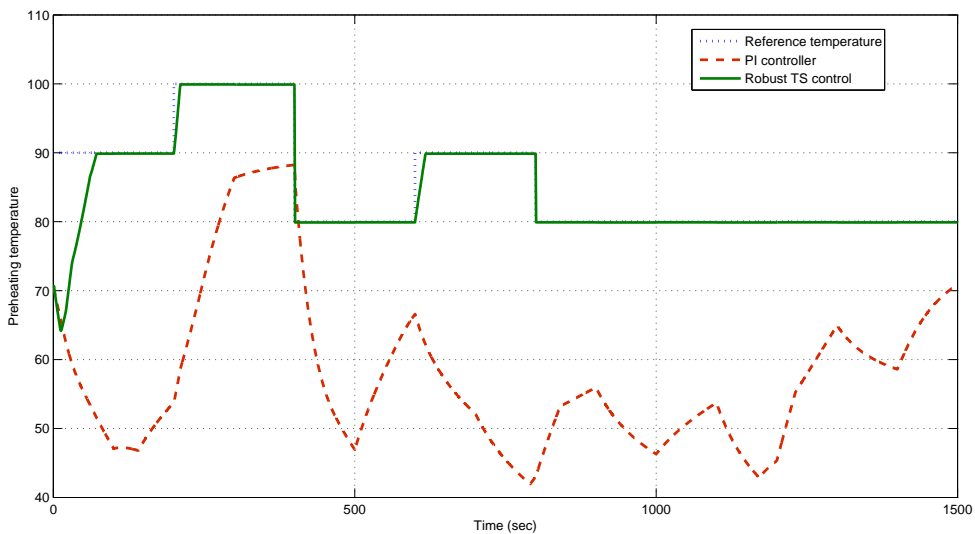


Figure 7.11: Preheating temperature tracking control comparison.

7.8 Conclusions

In this chapter, the robust stabilization problem of printing systems has been examined. The control design stabilizes the system for all bounded disturbances by optimizing the corresponding \mathcal{L}_2 gain performance criterion. T-S model is proposed as a feasible representation for the printing system. The approximation error between the original model of the printing system and the approximated T-S model is taken into account to guarantee both the stability of the T-S model as well as the stability of the printing system. A nonlinear scheduled observer-based output feedback control scheme is designed to tackle this problem. Unlike the approaches using a single quadratic Lyapunov function, a parameter varying quadratic Lyapunov function is employed in our approach. A solution for such a problem is presented and a relaxed LMI stability condition is derived for which dedicated numerical solvers are available. The proposed controller yields considerable improvements compared to the present industrial PI controller.

Chapter 8

Conclusions and Recommendations

8.1 Conclusions

In this chapter, the main conclusions are presented and some recommendation are given. The goal of this thesis was to improve the performance of professional printing systems. Two test cases are considered, namely, a professional inkjet printer and a professional laser printer. In both cases, there are many operational issues where control can have a major impact in solving them.

8.1.1 Professional inkjet printer

The main challenge in the inkjet printer is to design actuation pulses such that for any random bitmap and for any jetting frequency a good printing quality is achieved. To achieve this objective, several control strategies have been addressed in this thesis.

- We have demonstrated that feedforward control is a suitable control strategy to overcome the residual vibrations and the crosstalk. Consequently, the printing quality of inkjet printhead is considerably improved, beyond current limits. The experimental results have shown the effectiveness of the inverse-based feedforward approach. The major drawback of the feedforward control is that an accurate model is needed, and there must not be any unmeasured disturbances. That makes feedforward control very sensitive to any model uncertainty and unmodeled dynamics. Therefore, a further improvement can be achieved by improving the predictability of the narrow-gap model. Particularly, the model should be improved to predict the meniscus position, which plays an important role in determining the drop velocity. Moreover, this model should be modified to include the refill dynamics of ink inside the channel after jetting a drop. The jetting process and drop formation dynamics have to be included in the design of the input

pulse.

- We have illustrated that the available physical models are not suited for pulse design since these models do not include dynamics of the meniscus position. Therefore, an experimental-based optimization scheme has been proposed to minimize the drop velocity variations. Hence, there is no need for an accurate model. Furthermore, the pulse design is based on controlling the drop velocity and not on an intermediate state, meniscus speed, as in the model-based feedforward control.
- By understanding the physics of the print channel, we have proposed a new actuation pulse parameterization, which reflects the relation between the input pulse parameters and the print channel dynamics. The proposed input pulse has less unknown parameters, which improves convergence considerably. This parameterization has sparked a flurry of a possibility of real-time adaptation of the pulse to cope with the change of the printhead characteristics due to aging and wear. If the PAINT signal (or meniscus speed) is measured online, the damping factor μ and the two frequency modes F_1, F_2 can be estimated from the frequency content of the measured variable.
- We have shown that a flat DoD speed curve is neither a sufficient, nor a necessary condition for high print quality. DoD speed curve is a performance measure for continuous jetting, which is a contradiction of the drop on demand principle. However, having a flat DoD speed curve is a good starting point for real performance improvement. We have shown that introducing 0-pixels in the bitmap considerably influences the print quality, since the state of the meniscus (velocity, position) at the start of the succeeding pulse influences the drop velocity and, consequently, the print quality. Any pulse design has to guarantee almost the same initial meniscus state at the firing instant of a drop. Toward this end, for jetting patterns containing “0”, a non-jetting pulse is optimized to ensure that the same initial meniscus state of the subsequent drop.
- The effectiveness of both approaches has been elucidated by several experimental tests. The performance is evaluated based on the drop velocity variations for one channel. Table 8.1 summarizes the performance of the model-based feedforward control, experimental-based control, and standard pulse, where Δv_{max} represents the maximum drop velocity variations over the frequency range 20-70 kHz and it is defined as

$$\Delta v_{max} = \max_f (v_{max}(f) - v_{min}(f))$$

Δv_{max}	Standard pulse	Experimental-based control	Model-based control
DoD speed curve	12 m/s	0.8 m/s	3 m/s
Jetting pattern 1111111111	3 m/s	0.65 m/s	1.5 m/s
Jetting pattern 1111101010101	6 m/s	1 m/s	2 m/s
Jetting pattern 10101010111111	6 m/s	1 m/s	2 m/s

Table 8.1: Performance comparison for single channel

with $f \in [20, 70]$ is the jetting frequency. For a given pattern, v_{max} and v_{min} are the maximum and minimum velocity of the jetted drops, respectively. Using two optimized pulses, over frequency range 20-70 kHz, result in an improvement of a factor 15 compared to the standard pulse.

- We have demonstrated that by dividing the ink channels into a number of groups and introducing a proper time delay between the actuation of those groups the effect of the crosstalk between the channels is sufficiently reduced. By optimizing the time delay between 16 channels, the crosstalk effect is reduced by a factor 5.
- A set of input actuation pulses is optimized based on the jetting bitmap (multiple channels). For any random bitmap, choosing the proper actuation pulses leads to less drop velocity variations, and consequently improves printing quality by a factor 3 compared to the standard pulse.

8.1.2 Professional laser printer

As explained in chapter 5, there are several challenging problems that negatively affect the performance of a laser printing system. In this thesis, we focus on two main directions to tackle this problem.

- The first direction is finding the best control technique to achieve adaptability in the physical layer with fast and large parameter variations. This issue is alleviated by adaptive control. Standard adaptive control has a limited performance in the presence of large and fast parameter variations. Therefore, we have developed two different approaches to improve the convergence of MRAC.
 1. A nonlinear time varying adaptation gain has been chosen to be a function of the error to accelerate the adaptation process when the error is large. To proof the stability of the closed loop system, a new Lyapunov function is

employed. We have shown that the standard MRAC with a constant adaptation gain is a special case of the proposed MRAC.

2. A multiple adaptation gain has been designed based on the operating point to improve the convergence of the adaptation law. The T-S model has been used to approximate the nonlinear error dynamics composed of the tracking error and the controller parameters error. Owing to this formulation, a systematic procedure is derived for the adaptive control synthesis, where an LMI feasibility problem has been solved. We have shown that using multiple adaptation gains results in a considerable improvement in the convergence rate for both state and output feedback compared to a constant adaptation gain. We have demonstrated that MRAC with multiple adaptation gains has a better tracking performance compared to the MRAC with the nonlinear adaptation gain, because the T-S model allows the design of adaptation gains based on the operating point. Moreover, it allows the formulation of the adaptive problem as an LMI feasibility problem, which guarantees the convergence of both the tracking and the controller parameter errors. Furthermore, the LMI problem results in optimal adaptation gains, which minimizes an \mathcal{L}_2 gain performance criterion.
- The application of the proposed approaches in controlling a printing system has shown good tracking and robust stability in the presence of large parameters variations. We have demonstrated that MRAC with multiple adaptation gains has a better tracking performance compared to the MRAC with the nonlinear adaptation gain. We have demonstrated that using the proposed MRAC schemes the printing quality with higher throughput can be considerably improved in the presence of large and fast parameter variations compared to the present industrial controller.
 - The second approach uses the available knowledge about the printing jobs to further improve the performance of the printing system. A nonlinear scheduled observer-based output feedback control scheme has been designed. The T-S model has been proposed as a feasible representation for the printing system at different print jobs. The approximation error between the original model of the printing system and the approximated T-S model has been taken into account to guarantee both the stability of the controlled T-S model as well as the stability of the printing system. Less conservative stability conditions have been derived by using a parameter varying quadratic Lyapunov function. Furthermore, a solution for such a problem has been presented as a relaxed LMI stability condition. Including the knowledge about the printing jobs in the controller design yields considerable improvements compared to both adaptive control and the present industrial PI controller.

8.2 Recommendations

For inkjet printing systems, all the approaches addressed in this thesis are feedforward solutions due to the measurement limitations. However, uncertainties and external disturbances might be encountered during the operation of the printers, which might degrade the performance of the printing system. These uncertainties occur due to the changing environment in which they operate. An online adaptation technique should be further studied to adapt the pulse parameters to cope with these operational uncertainties. Currently, the PAINT signal is the only available online measurement. However, the PAINT signal can be used for adaptation only at low jetting frequencies. Other possible measuring methods should be considered, such as adding a small camera to measure the drop velocity directly or scanning the printed image and compare it with the real image. A good operational print quality measure should be properly defined. It has to be sensitive for the effects we want to observe (e.g. pulse shape, paper velocity variation, viscosity ink, etc) and selective (measure only the effects we want to observe). Moreover, the scanner resolution should be higher than the print resolution.

A second option to deal with online disturbances is the implementation of feedback control. Since the meniscus velocity cannot be measured online, an estimator can be designed to estimate the meniscus velocity based on the measurements of the PAINT signal. Thus, a feedback controller can be designed to control the meniscus velocity. A fast feedback controller is required due to the short sampling time. A block diagram of the printhead with all possible variables, which can be used for online adaptation or feedback control is shown in Figure 8.1. A comparison of these different control techniques is summarized in Figure 8.2.

For laser printing, throughout this thesis we did not put any constraint on input power and temperatures. However the power supply is a limiting factor in achieving high throughput. Moreover, we also assumed that the print jobs are directly implemented with the order defined by the user without any further processing. In addition, the amount of energy needed to establish the temperatures required by the printing process determines the amount of time needed for the printer to warm up in preparing for the first print. This time must be as short as possible, and is directly determined by the speed with which the temperature levels can rise to acceptable levels in a printer. Therefore, rescheduling of the print jobs could yield a better performance of the printing system with minimum warm up time. The belt speed is assumed to be controlled using a separate controller. To achieve a fully controlled system with high throughput, a unified control and scheduling approach should be studied to include the power supply constraint and consider pre-heater power, TTF power, belt speed, heat exchanger, simplex, duplex, the spacing between two sheets and the print jobs as controllable input, see Figure 8.3.

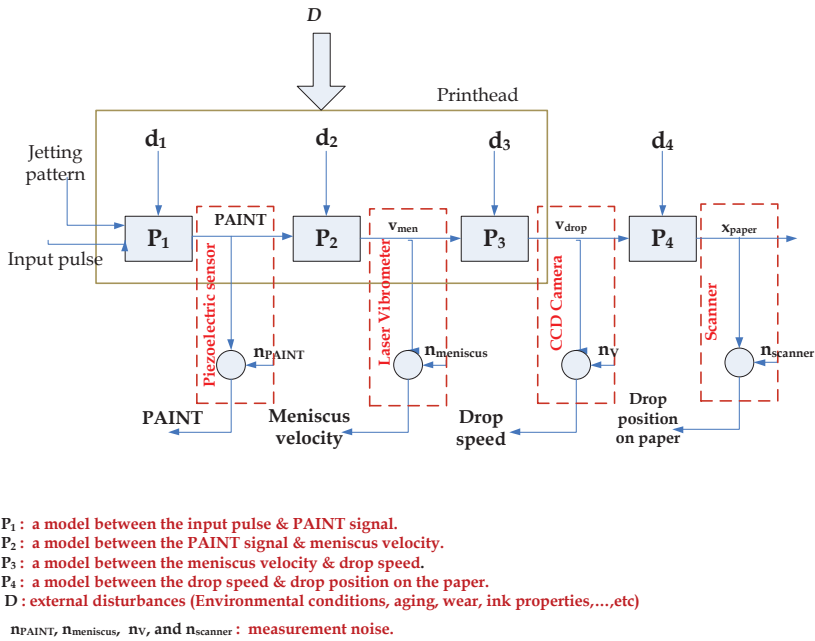


Figure 8.1: Schematic diagram of all possible signals that could be used for online adaptation or feedback control

Control Technique	Model dependency	Sensor required	Estimated variable	Jetting channels		Performance		Sensitivity	
				One	Multiple	Without pulse scheduling	With pulse scheduling	Model uncertainty	External disturbances
Feedforward inverse control	High	No	Meniscus velocity	✓	✓	Good (+)	Better (++)	High (-)	High (-)
Model-free optimization	No	CMOS camera	Drop velocity	✓	✓	Better (++)	Much better (+++)	none	High (-)
Online adaptation	Small	Small camera	Drop velocity	✓	✓	Much better (+++)	Much better (+++)	Low (-)	Less (+)
Feedback control	Small	PAINT (Print)	Meniscus velocity	✓	✓	Much better (+++)	Much better (+++)	Low (-)	Low (++)

Figure 8.2: Comparison of all possible control techniques for inkjet printer

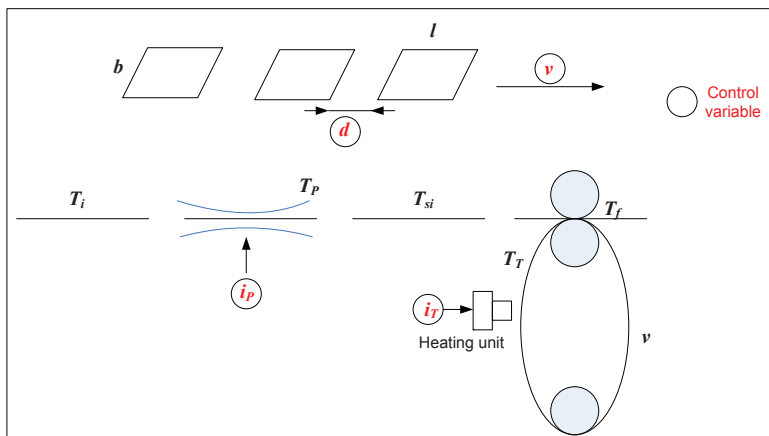


Figure 8.3: Schematic diagram of control variables and temperatures for laser printer

Bibliography

- [1] K. Kwon, S. Shin, and S. Kim, "The opportunity of printing technology for display manufacturing process," *Proc. of the Colloquium on Micro/Nano Thermal Engineering*, pp. 17-19, 2005.
- [2] T. Gohda, Y. Kobayashi, K. Okanao, S. Inoue, K. Okamoto, S. Hashimoto, E. Yamamoto, H. Morita, S. Mitsui, and M. Koden, "A 3.6-in 202-ppi full-color amplified display fabricated by ink-jet method," *Proc. of the SID 06 Digest*, pp. 1767-1770, 2006.
- [3] M. Bale, J. C. Carter, C. J. Creighton, H. J. Gregory, P. H. Lyon, P. Ng, L. Webb, and A. Wehrum, "Ink-jet printing: The route to production of full-color P-OLED displays," *Journal of the Society for Information Display*, vol. 14, pp. 453-459, 2006.
- [4] D. Albertalli, "Gen 7 FPD inkjet equipment - Development status," *Proc. of the SID 05 Digest*, pp. 1200-1203, 2005.
- [5] H.S. Kooa, M. Chenb, P.C. Pana, L.T. Chouc, F.M. Wuc, S.J. Changc, and T. Kawaia, "Fabrication and chromatic characteristics of the greenish LCD color-filter layer with nano-particle ink using inkjet printing technique," *Displays*, vol. 27, pp. 124-129, 2006.
- [6] F.R.S. Rayleigh, "On the instability of jets," *Proc. London Math. Soc.*, vol. 10, pp. 4-13, 1878.
- [7] R. Elmqvist, "Measuring instrument of the recording type," US Patent no. 2566443, 1948.
- [8] R.G. Sweet, "Signal apparatus with fluid drop recorder," US Patent no. 3596275, 1971.
- [9] W.L. Buehner, J.D. Hill, T.H. Williams, and J.W. Woods, "Application of ink-jet technology to a word processing output printer," *IBM Journal of Research and Development*, vol. 21, pp. 2-9, 1977.

- [10] S.L. Zoltan, "Pulse drop ejection system," US Patent no. 3857049, 1974.
- [11] I. Endo, Y. Sato, S. Saito, T. Nakagiri, and S. Ohno, "Liquid jet recording process and apparatus thereof," UK Patent no. 2007162, 1979.
- [12] J.L. Vaught, F.L. Cloutier, D.K. Donald, J.D. Meyer, C.A. Tacklind, and H.H. Taub, "Thermal inkjet printer," US Patent no. 4490728, 1984.
- [13] L. Kuhn and A. Myers, "Inkjet printing," *Sci. Am.*, vol. 240, pp. 162-178, 1979.
- [14] W. Wehl, "Nur nicht kleckern," *CHIP*, vol. 8, pp. 104-112, 1994.
- [15] D. B. Bogy and F.E. Talke, "Experimental and theoretical study of wave propagation phenomena in drop-on-demand inkjet devices," *IBM Journal of Research and Development*, vol. 28, pp. 314-321, 1984.
- [16] B. V. Antohe and D. B. Wallace, "Acoustic phenomena in a demand mode piezoelectric inkjet printer," *Image Science and Technology*, vol. 46, pp. 409-414, 2002.
- [17] H.M.A. Wijshoff, *Structure- and fluid-dynamics in piezo inkjet printheads*. PhD Thesis, 2008.
- [18] M. B. Groot Wassink, *Inkjet printhead performance enhancement by feedforward input design based on two-port modeling*. PhD Thesis, 2007.
- [19] W. de Zeeuw. *Akoestisch inkjet model met refill*. Internal report at Océ, 2005.
- [20] S. S. Berger and G. Recktenwald, "Development of an Improved Model for Piezo-Electric Driven Ink Jets," *International Conference on Digital Printing Technologies*, New Orleans, 2003.
- [21] S. Sakai, "Dynamics of Piezoelectric inkjet printing system," *IS & T NIP 16*, pp. 15-20, Vancouver, Canada, 2000.
- [22] D. Y. Shin, P. Grassia, and B. Derby, "Oscillatory incompressible fluid flow in a tapered tube with a free surface in an inkjet printhead," *Journal of Fluids Engineering*, vol. 127, pp. 98-109, 2005.
- [23] T. W. Schield, D.B. Bogy, and F. E. Talke, "A numerical comparison of one-dimensional fluid jet models applied to drop-on-demand printing," *Journal of Computational Physics*, vol. 67, pp. 327-347, 1986.
- [24] R.M. Redheer, "On a certain linear fractional transformation," *Journal of Math. and Physics*, vol. 39, pp. 269-286, 1960.

- [25] J. S. Dewey, K. Leang, and S. Devasia, "Experimental and theoretical results in output-trajectory redesign for flexible structures," *ASME J. Dynamics Syst. Measurement Control*, vol. 120, pp. 456-461, Dec. 1998.
- [26] S. Devasia, "Should model-based inverse input be used as feedforward under plant uncertainty?," *IEEE Trans. Automat. Contr.*, vol. 47, pp. 1865-1871, Nov. 2002.
- [27] S. Devasia, D. Chen, and B. Paden, "Nonlinear inversion-based output tracking," *IEEE Trans. Automat. Contr.*, vol. 41, pp. 930-942, July 1996.
- [28] M. Ezzeldin, P.P.J. van den Bosch, and S. Weiland, "Inverse-based feedforward control for an inkjet printhead," *Proc. of the American Control Conf.*, San Francisco, California, USA, June 2011, pp. 4087-4092.
- [29] P.M.J. Van den Hof, X.J.A. Bombois. *System identification for control*. Lecture notes of DISC course.
- [30] D. Bertsimas, D.B. Brown, and C. Caramanis, "Theory and applications of robust optimization," *Society for Industrial and Applied Mathematic*, vol. 53, pp. 464-501, 2011.
- [31] C. Scherer, S. Weiland. *Linear Matrix Inequalities in Control*. Lecture notes of DISC course.
- [32] M. Ezzeldin, P.P.J. van den Bosch, A. Jokic, and R. Waarsing, "Model-free optimization based feedforward control for an inkjet printhead," *Proc. of the 2010 IEEE Multi-Conference on Systems and Control*, Yokohama, Japan, September 2010, pp. 967-972.
- [33] M. Ezzeldin, P.P.J. van den Bosch, and S. Weiland, "Towards a Better Printing Quality for an Inkjet Printhead," submission to *IEEE Control Systems Magazine*.
- [34] R. C. Gonzalez and R. E. Woods. *Digital Image Processing*. Addison-Wesley, 1993.
- [35] F.van der Heijden. *Image Based Measurement Systems: Object Recognition and Parameter Estimation*. Wiley & Sons, 1995.
- [36] S. Hutchinson, G. Hager, and P. Corke, "A Tutorial on Visual Servo Control," *IEEE Transactions on Robotics and Automation*, vol. 12, pp. 651-670, Oct.1996.
- [37] A. P. Ruszczynski. *Nonlinear optimization*. Princeton University Press, 2006.
- [38] T. V. Mikosch, S. I. Resnick, and S. M. Robinson. *Numerical Optimization*. Springer: New York, 2006.

- [39] M. Bartholomew-Biggs. *Nonlinear Optimization with Engineering Applications*. Springer Optimization and Its Applications, vol. 19, 2008.
- [40] J.A. Nelder and R. Mead, "A simplex method for function minimization," *Computer Journal*, vol. 7, pp. 308–313, 1965.
- [41] K.I.M. McKinnon, "Convergence of the NelderMead simplex method to a non-stationary point," *SIAM Journal on Optimization*, vol. 9, pp. 148–158, 1999.
- [42] Matlab Optimization Toolbox, The Mathworks Inc., 2010.
- [43] Laser printer. Internet site, www.wikipedia.org.
- [44] Facts about laser printing. Internet site, www.Papergear.com.
- [45] E. D. Reilly, *Milestones in Computer Science and Information Technology*, Greenwood Press. 2003.
- [46] The history of Xerography. Internet site, www.fujixerox.com.au
- [47] The Story of Xerography, Xerox Corporation, 1989.
- [48] J . H. Dessauer and H. E. Clark, *Xerography and Related Processes*, The Focal Press, New York, 1965.
- [49] V. M. Fridkin, *The Physics of The Electrophotographic Process*. The Focal Press, New York, 1972.
- [50] M. E. Williams, *The Physics and Technology of Xerographic Processes*. John Wiley and Sons, New York, 1984.
- [51] M.P.M.H. Heemels and G.J. Muller, *Boderc: Model-based design of high-tech systems*. Embedded Systems Institute, Eindhoven, The Netherlands, 2007.
- [52] B. Krijnen, *Heat flow modeling in copiers*, master report, University of Twente, The Netherlands, 2007.
- [53] John H. L. VI and John H. L. V, *a Heat Transfer Textbook*. The Phlogiston Press, Cambridge, Massachusetts, USA, 2004.
- [54] K. J. Astrom and B. wittenmark, *Adaptive Control*. Addison- Wesley, 1995.
- [55] H. Butler, *Model Reference Adaptive Control From Theory to Practice*. Prentice Hall International, 1992.
- [56] M. A. L. Thathachar and F. Gajendran, "Convergence problems in a class of model reference adaptive control systems," *Proc. of the Conference on Decision and Control*, New Orleans, LA, USA. 1036-1041. 1977.

- [57] H. N. Nounou and K. M. Passino, "Stable auto-tuning of the adaptation gain for continuous-time nonlinear systems," *Proc. of the Conference on Decision and Control*, Orlando, FL, USA. 2037-2042. 2001.
- [58] H. N. Nounou and K. M. Passino, "Stable auto-tuning of the adaptation gain for direct adaptive control," *Proc. of American Control Conf.*, Chicago, IL, USA. 2154-2158. 2000.
- [59] R. V. Monopoli, "Model reference adaptive control with an augmented error signal," *IEEE Transactions on Automatic Control*, vol. AC-19, no. 5, pp. 474-484, 1974.
- [60] C. Cao and N. Hovakimyan, "Design and analysis of a novel L_1 adaptive control architecture with guaranteed transient performance", *IEEE Transactions on Automatic Control*, vol. 53, No. 2, pp. 586-591, 2008.
- [61] N. Nguyen, K. Krishnakumar, J. Kaneshige, and P. Nespeca, "Flight dynamics and hybrid adaptive control of damaged aircraft", *AIAA Journal of Guidance, Control, and Dynamics*, vol. 31, No. 3, pp. 751-764, 2008.
- [62] M. Ezzeldin, and R. Waarsing, "Improved convergence of MRAC design for printing system", *Proc. of the 28th American Control Conference*, St. Louis, MO, USA. pp. 3232-3237, June 2009.
- [63] M. Ezzeldin, S. Weiland, and P.P.J. van den Bosch, "Improving the performance of a printing system using model reference adaptive control: an LMI Approach," *Proc. of the American Control Conference*, Montréal, Canada, June 2012.
- [64] T. Kailath, *Linear Systems*. Prentice Hall International, 1980.
- [65] P. Ioannou, and P. Kokotovi, *Adaptive Systems with Reduced Models*. Springer-Verlag, 1983.
- [66] T. Takagi and M. Sugeno, "Fuzzy identification of systems and its applications to modeling and control," *IEEE trans. on Systems, Man, and Cybernetics*, vol. 15, no. 1, pp. 116-132, 1985
- [67] L. Wang, *a Course in Fuzzy Systems and Control*. Prentice Hall, London, UK, 1997.
- [68] K. Tanaka, and M. Sugeno, "Stability analysis and design of fuzzy control systems," *Fuzzy Sets Syst.*, vol. 45, no. 2, pp. 135-136, Jan. 1992.
- [69] S. Cao, N. Rees, and G. Feng, "Analysis and design of fuzzy control systems using dynamic fuzzy global models," *Fuzzy Sets and Syst.*, vol. 75, no. 1, pp. 47-62, Oct. 1995.

- [70] M. Takahashi, I. Mizumoto, and Z. Iwai, "Adaptive output feedback control system design for MIMO plants with unknown plant orders," *Transactions of the Society of Instrument and Control Engineers*, vol. 33, no. 5, pp. 359-367, 1997.
- [71] I. D. Landau and H. M. Silveira, "A stability theorem with applications to adaptive control," *IEEE Transactions on Automatic Control*, vol. 24, no. 2, pp. 305-312, 1979.
- [72] K. S. Narendra and L. S. Valavani, "Stable adaptive controller design-direct control," *IEEE Transactions on Automatic Control*, vol. 23, no. 4, pp. 570-583, 1978.
- [73] S. Boyd, L. El Ghaoui, E. Feron, and V. Balakrishnan, *Linear Matrix Inequalities in System and Control Theory*. Philadelphia, (PA:SIAM), 1994.
- [74] Stephen Boyd and Lieven Vandenberghe, *Convex Optimization*. 2004, (Cambridge University Press), Internet site, <http://www.cambridge.org>.
- [75] H. Wang, K. Tanaka and M. Griffin, "Parallel distributed compensation of nonlinear systems by Takagi-Sugeno fuzzy model," *Proc. FUZZ/IFES*, vol. 2, pp. 531-538, 1995.
- [76] L. Tanaka, and H. Wang, "Fuzzy control systems design and analysis: A linear matrix inequality approach," John Wiley & Sons, Inc., 2001.
- [77] L.A. Mozelli, R.M. Palhares, F.O. Souza and E.M.A.M Mendes, "Reducing conservativeness in recent stability conditions of TS fuzzy systems," *Automatica*, 2009.
- [78] K. Tanaka, T. Hori and H. Wang, "A fuzzy Lyapunov approach to fuzzy control system design," *Proc. ACC*, vol. 6, pp. 4790-4795, 2001.
- [79] B. Ding, H. Sun and P. Yang, "Further studies on LMI-based relaxed stabilization conditions for nonlinear systems in Takagi-Sugeno's form," *Automatica*, vol. 42, pp. 503-508, 2006.
- [80] H. Fang, Y. Liu, W. Kau, L. Hong and H. Lee, "A new LMI- based approach to relaxed quadratic stabilization of T-S fuzzy control systems," *IEEE Trans. Fuzzy Syst.*, vol. 14, pp. 386-397, 2006.
- [81] G. Feng, "Controller synthesis of fuzzy dynamic systems based on piecewise Lyapunov functions," *IEEE transaction on Fuzzy Systems*, vol. 11, pp. 605-612, 2003.
- [82] M. Ezzeldin, A. Jokic, and P.P.J. van den Bosch, "A Parameter Varying Lyapunov Function Approach for Tracking Control for Takagi-Sugeno Class of Nonlinear

- Systems” *Proc. 8th IEEE Int. conference on Control and Automation*, Xiamen, China, pp. 428-433, June 2010.
- [83] M. Ezzeldin, H.M.Emara, A.Elshafei, and A. Bahgat, Observer based fuzzy-control design using relaxed LMI conditions, *IEEE Conference on Decision and Control*, pp. 5312–5317, Dec. 2007.
- [84] M. Ezzeldin, S. Weiland, and P.P.J. van den Bosch, “Robust \mathcal{L}_2 Control for a Class of Nonlinear Systems: A Parameter Varying Lyapunov Function Approach,” *Proc. 19th Mediterranean Conference on Control and Automation*, Corfu, Greece, pp. 213–218, June 2011
- [85] P. P. Khargonekar, I. R. Petersen, and K. Zhou, “Robust stabilization of uncertainty linear systems: Quadratic stabilizability and H_∞ control theory,” *IEEE Trans. Automat. Contr.*, vol. 35, no. 3, pp. 356–361, 1990.
- [86] B. S. Chen, C. S. Tseng, and H. J. Uang, “Mixed H_2/H_∞ fuzzy output feedback control design for nonlinear dynamic systems: An LMI approach,” *IEEE Trans. Fuzzy Syst.*, vol. 8, pp. 249–265, 2000.
- [87] M. Ezzeldin, S. Weiland, and P.P.J. van den Bosch, “Observer-Based Robust \mathcal{L}_2 Control for a Professional Printing System,” *Proc. of the American Control Conference*, Montréal, Canada, June 2012.
- [88] S. K. Nguang and P. Shi, “ H_∞ output feedback control design for uncertain fuzzy systems with multiple time scales: an LMI approach,” *European Journal of Control*, vol.11, no. 2, pp. 157-166, 2005
- [89] A. Rantzer and A. Megretski, “A tutorial on integral quadratic constraints: Part I: IQC models and their feasibility,” *Personal Correspondence*, 2002.

Acknowledgments

This work has been carried out as part of the OCTOPUS project with Océ Technologies B.V. under the responsibility of the Embedded Systems Institute. This project is partially supported by the Netherlands Ministry of Economic Affairs under the Bsik program.

This thesis has been part out of years of research that has been done since I joined the control systems group at Electrical Engineering. By that time, I have worked with several people who have major contributions in assorted ways to this research. It is my pleasure to convey my gratitude to all of them in my humble acknowledgment.

First of all, I would like to express my sincere gratitude to Prof. Paul van den Bosch for his supervision and guidance. His encouragement, discussions, and advices from the preliminary to the concluding level have a great influence on my way of thinking. Also I would like to thank him for giving me the opportunity to work on this project as well as giving me extraordinary experiences through out the work. Thanks for your trust.

If you have any mathematical issues that you could not solve or something you could not prove, you should go to Prof. Siep Weiland. He always has the key for the closed doors. I am gratefully acknowledge to Siep for his intensive technical support and cooperation. His mathematical knowledge and creative insights added a great value to this work.

I would like to express my sincere appreciation to the project members at Océ, Wim de Zeeuw, Pierre Klerken, Hans Reinten, Herman Wijshof, Sjirk Koekebakker and René Waarsing, for their valuable information, discussions, and support for the completion of this work. Their fruitful discussions have played an important role to understand the printing process and to improve my practical knowledge. Also I would like to thank Jan Simons for his technical support.

To Amol Khalate, it has been a pleasure to collaborate with you. We have such a pleasant time when working together.

I convey special acknowledgment to Frans Reckers, Twan Basten, and Jacques Ver-

riety from the Embedded Systems Institute for their indispensable help dealing with any problem within the project. I have to admit that writing a work plan and a work summary every few months have been useful for me and have helped me to finish the thesis on time. In addition, all the content and partner meetings had a great influence on my presentation skills.

I gratefully thank the committee members for their constructive comments on this thesis. I am thankful that in the midst of all their busy activity, they accepted to be members of the committee.

Also I would like to thank my colleagues at the control systems group for helping me to broaden my view and knowledge. I have enjoyed the nice working atmosphere within the group. I am gratefully acknowledge to Dr. Hakan Koroglu for his generous support with references, discussions, and valuable comments. Special thanks to my officemates, Mark and Jaron, for their help, support, interest, and valuable hints. I will never forget the special Dutch words that you taught me.

My deepest gratitude to my parents for their inseparable support and prayers. I would like to give my special thanks to my wife, Donia, whose support enabled me to complete this work. I cannot forget to thank my son, Kareem, for waiting inside his mother's belly until I finished the thesis :-).

Finally, I offer my regards to all of those who supported me in any respect during the completion of this work.

Mohamed

Curriculum Vitae

Mohamed Ezzeldin Mahdy was born on July 20, 1983 in Menia, Egypt. He received his Bachelors degree (May 2005) and Masters degree (December 2007) in Electrical Engineering from Cairo University, Egypt. His master thesis is titled *Relaxed Stability Conditions of Fuzzy Systems: an LMI Approach*. At the same time, he was working as teaching assistant at Control System group, Electrical Engineering department, Cairo University, Egypt. In May 2008, he was appointed as a PhD student in Control Systems group, Electrical Engineering department, Eindhoven University of Technology, The Netherlands. His PhD project focuses on adaptive control of professional printers. The results of this research are presented in this thesis titled *Performance Improvement of Professional Printing Systems: from theory to practice*.